Structure and Dynamics of End-capped Star Polymers in Aqueous Solution and in Microemulsion

vorgelegt von

Paula Malo de Molina

Madrid, Spanien

Von der Fakultät II - Mathematik und Naturwissenschaften
der Technischen Universität Berlin
zur Erlangung des akademischen Grades
Doktor der Naturwissenschaften
Dr.rer.nat.

genehmigte Dissertation

Promotionsausschuss:
Vorsitzender: Prof. Dr. rer. nat. Reinhard Schomäcker
Gutachter: Prof. Dr. rer. nat. Michael Gradzielski
Gutachter: Prof. Dr. rer. nat. André Laschewsky
Gutachter: Prof. Dr. rer. nat. Arturo López Quintela

Tag der wissenschaftlichen Aussprache: 12.07.2012

Berlin 2012

D83

Zusamenfassung

Mischungen telecheler Polymere und Mikroemulsionen sind von großer Bedeutung aufgrund ihrer vielfältigen möglichen Anwendungen und da sie als Modellsysteme für selbstaggregierte Netzwerke dienen können, bei denen die Konzentration und Konnektivität der Verknüpfungspunkte unabhängig voneinander variiert werden können. Außerdem sollte die Strukturrelaxationszeit getrennt über die hydrophoben Enden der telechelen Polymere gesteuert sein.

Diese Arbeit präsentiert eine umfangreiche Untersuchung des Assoziationsverhaltens telecheler Sternpolymere in wässriger Lösung, in Anwesenheit und Abwesenheit von Mikroemulsionströpfchen unterschiedlicher Größe und mittleren Abstandes. Dabei wurde der Effekt unterschiedlicher Typen solcher mehrfach verbrückender Polymere und ihr Effekt auf Struktur und Dynamik von Öl-in-Wasser Mikroemulsionströpfchen untersucht. Hierzu wurden maßgeschneiderte verbrückende amphiphile Polymere mit zwei bis vier hydrophoben Endgruppen verwendet, die durch RAFT (reversible addition fragmentation chain transfer) Polymerisation hergestellt worden war. Diese erlaubt die getrennte Variation der Anzahl der Arme (Funktionalität), der Länge des hydrophilen Blockes (maximale Verbindungslänge des Netzwerkes) und der hydrophoben Endkette (Verankerungsstärke).

Ein detailliertes Strukturbild wurde durch SANS Messungen, speziell bezüglich der Tröpfchengrößen und der durch das verbrückende Sternpolymer induzierten Wechselwirkungen in der Mikroemulsion, erhalten. Diese Messungen zeigten, dass die Größe durch das Polymer nur wenig beeinflusst werden, während die Wechselwirkung sehr wohl durch die Anwesenheit des Polymer modifiziert werden. Weiterführende Messungen der Dynamischen Lichtstreuung und der Rheologie (bis zu hohen Frequenzen von 2000 Hz) erlaubten eine Korrelation der mikroskopischen und makroskopischen Dynamik. Diese Experimente zeigten eine erheblichen Einfluss der Länge der hydrophoben Endgruppe auf die Rheologie und insbesondere die Strukturrelaxationszeit, die exponentiell mit der hydrophoben

Kettenlänge anwächst, was sich auf der Affinität der Endgruppe zu den Öltröpfchen begründet. Das dynamische Verhalten des Systems wird mit steigender Anzahl der Arme wesentlich komplexer und sehr langsame Relaxationsprozesse werden sehr bedeutend, was eine wesentlich effektivere Netzwerkausbildung anzeigt. Offensichtlich ist die Funktionalität dieser verbrückten Systeme ein maßgeblicher Faktor bei der Netzwerkausbildung und damit der Kontrolle der Mikroemulsionsrheologie, während gleichzeitig die Länge der Polymerketten die Längenskala bestimmt, über die Vernetzung möglich ist. Zusammenfassend lässt sich sagen, dass die Architektur der telechelen Polymere (Anzahl und Länge der Arme sowie die Länge der hydrophoben Verankerung) zentrale Parameter zur Kontrolle des rheologischen, dynamischen und strukturellen Verhaltens von Mikroemulsionen sind.

Abstract

Mixtures of telechelic polymers and microemulsions have a tremendous interest due their wide range of potential applications and also because they serve as model systems of self-assembled networks, where the concentration of nodes and the connectivity can be tuned separately. Therefore, the rheological properties of these materials can be controlled by different topological parameters over a wide range. In addition, as self-assembling systems their characteristic structural relaxation time may be controlled via the hydrophobic ends of the telechelic polymers.

This work presents a comprehensive study of the association behavior of telechelic star polymers in aqueous solution, in the absence or presence of microemulsion droplets of different size and spacing. We have investigated various types of multiply bridging polymers and their effect on the structure and dynamics of oil in water microemulsion droplets. For that purpose we employed tailor made bridging amphiphilic polymers with two to four linkers that were synthesized by the RAFT procedure, allowing to control the number of arms (functionality), the length of the hydrophilic block (maximum length for connection) and of the hydrophobic chain (stickiness) in a clearly separate fashion.

A detailed structural picture was obtained by SANS measurements, especially with respect to the effects on the droplet sizes and even more on the interactions in the microemulsion systems induced by the bridging star polymer. They showed that the size is little affected by the addition of the polymer while the interactions are modified by the presence of the polymer. In addition, dynamic light scattering and rheology measurements going to high frequencies (2000 Hz) were carried out, which allowed to correlate microscopic and macroscopic dynamics. These experiments show that increasing the sticker length has an enormous impact on the rheology and, in particular, on the structural relaxation time which rises exponentially with the length of the hydrophobic chain due to a stronger affinity of the end-cap chain to the oil droplets. The dynamic response of the systems becomes

much more complex with increasing number of arms and slow relaxation processes become very pronounced due to a much more efficient network formation. Accordingly the functionality of these bridging systems is an important factor in network formation and control of rheology in microemulsions, while the length of the polymer chains determines the length scale over which such networks are formed. In general, the architecture of the telechelic polymers (number and length of arms as well as length of the hydrophobic sticker) has been shown to be key points in controlling the rheological, dynamical and structural behavior of microemulsions.

Acknowledgements

This work has been possible only thanks to a large number of people. The ?rst, and more important, my supervisor Prof. Michael Gradzielski. His patience, support and intuition are inspiring. I am glad that Prof. Dr. Michael Gradzielski and Prof. Dr. Laschewsky gave me the opportunity of working in this interesting topic. I want to thank Prof. Dr. Laschewsky and Prof. Dr. López Quintela for being reviewers of the present thesis.

I am deeply grateful to Christoph Herfurth, who synthesized the end-capped star polymers. Without his work, mine would not be possible. He was always enthusiast and exited about the results, making the work in this project even more stimulating.

I am specially grateful to my colleagues at the group for their generosity and patience. They always found time to explain me how to model small angle scattering data, how an instrument works or how to declinate in German. It has been real fun to work with them. Specially thankful I am to Sylvain Prévost, who is responsible for almost all my knowledge in SANS, Raphael Michel, who spend many nights working in Beamtimes with me, and Franziska Ihlefeldt did the Phase Diagrams in Chapter 7. I thank Peggy Heunemann and Burcu Altin for their friendship.

Last but not least, I am grateful to my boyfriend Christian for his support and for making some of the sketches in this thesis.

Contents

Chapter 1

Introduction

1.1 Microemulsions

Microemulsions are isotropic, thermodynamically stable mixtures of two fluids forming nanoscale domains separated by an interfacial fluid film. In general, these fluids are water and oil and the film is made of surfactants. The surfactant at the oil-water interface lowers the surface tension. Their structure can be oil-in-water (O/W) or water-in-oil (W/O) droplets but also bicontinuous microemulsions are known [1–4].

The free energy of the surfactant layer at the liquid interface F is the result of the sum of the interfacial energy F_i, a bending energy term F_b, and an entropic term

$$F = F_i + F_b + F_{ent} = \gamma A + \int \left[\frac{K}{2} \left(C_1 + C_2 - C_0 \right)^2 + \bar{K} C_1 C_2 \right] dA + n k_B T f(\phi) \qquad (1.1)$$

where γ is the interfacial tension, A the total surface area of the film, K the mean elastic bending modulus, $\bar{K}$ is the Gaussian bending modulus, C_1 and C_2 are the two principal curvatures, C_0 the spontaneous curvature, n is the number of droplets, k_B is the Boltzmann constant, and $f(\phi)$ is a function of the droplet volume fraction ϕ that accounts for the entropy of mixing of the microemulsion droplets. For dilute systems where $\phi < 0.1$, it has been shown that that $f(\phi)$ can be approximated as $ln(\phi) - 1$. Microemulsion formation is associated with ultra-low interfacial tension, γ so the γA term can be neglected.

Consequently, the type of structure that is formed depends on the curvature of the interface that is controlled by the bending energy of the amphiphilic film [5,6]. In many cases

the film curvature can be estimated by simple geometrical requirements of the surfactant molecule. The geometry of the amphiphile may be described by the packing parameter, defined as the ratio of the hydrophobic chain molecular volume (v_s), which is the volume occupied by the surfactant in the assembly, to the product of the head group area (a_s) and the chain length (l_s) [7].

$$p = \frac{v_s}{a_s l_s} \tag{1.2}$$

In general terms, when $p < 1/3$ spherical aggregates are formed, cylindrical aggregates for $1/3 < p < 1/2$, bilayers for $p = 1$ and inverse structures when $p > 1$.

In the case of non-ionic surfactants, based on ethylene oxide (EO) head groups, the packing parameter changes with temperature [8]. The head group area of the EO chain decreases with increasing temperature because the hydration of the EO groups decreases. The temperature dependence decreases with increasing EO content for a given hydrophobic group, and at constant EO content it will be larger by decreasing the hydrophobe size, broadening the PEO chain-length distribution, and branching in the hydrophobic group. The ternary systems based on C_iE_j/Alkane Oil/Water exhibit a rich phase behavior by changing composition or temperature.

O/W microemulsions are generally low viscous liquids that find applications in many fields such as detergency, oil recovery and drug delivery [9, 10]. However, for a variety of situations their technical applicability is limited by their low viscosity. Therefore, the control of the viscosity of microemulsions is a highly interesting and important topic. There are various options for increasing the viscosity of microemulsions, which often are based on the addition of polymers. One logical option is to cross-link the oil droplets by bridging amphiphilic polymers, a concept which works well with end-capped PEO. The interconnection of droplets leads to a substantial increase in viscosity once passing an effective percolation concentration of droplets and polymer.

1.2 Associative Polymers in aqueous solution

Associative polymers (APs) are hydrophobically modified polymers that, due to their amphiphilic character, tend to aggregate in aqueous solutions. Their major interest is their applications as rheological modifiers. The properties of APs depend on the number of

associative groups. Polymers containing more than one associative group may associate in aqueous solution so that these groups assemble into the same aggregate or different aggregates.

In the following section the most relevant properties of associative polymers in aqueous solutions will be introduced. In the literature a large number works deal with different types of associative polymers, hydrophobically modified hydrophilic polymers or block copolymers with a great variety of chemical compositions and molecular architectures. All of them are based on the same mechanism and driving force. Some of this work is summarized in a recent review by Chassenieux et al. [11] and Tsitsilianis et al. [12].

1.2.1 Telechelic Polymers

Telechelic polymers aggregate at low concentrations into flower-like micelles [13]. The aggregation numbers are low (between 5 and 25) compared to those of surfactant micelles. For example, SDS has an aggregation number of 65 surfactant molecules per micelle [14]. The aggregation numbers determined by different techniques yield different numbers. The obtained aggregation numbers from fluorescence are lower than those obtained by static light (or neutron) scattering and these are slightly lower than from dynamic light scattering (DLS) and viscosimetry [15–17].

Moreover, the theory predicts that the aggregation number results from balancing the interfacial energy, configurational entropy, and excluded volume interactions in the corona against the deformation energy of the hydrophobic chains in the core. The polydispersity arises from thermal fluctuations [18]. In the case of long hydrophilic chains, the back-folding does not affect the free energy and, therefore, a solution of telechelic chains should have the same aggregation number in terms of the number of hydrophobes per micelle as a solution of double number of chains with one end-cap group [19]. In fact, this result has been also found experimentally by Sérero et al. [13].

By increasing the concentration, the micelles come closer together and polymer chains are able to reversibly form bridges between micelles [20]. This reversible intermicellar aggregation leads to the formation of clusters (See Fig 1.1). The size of the clusters grow with increasing concentration until a certain critical concentration, where one cluster occupies the entire volume. At this concentration, the percolation concentration, a transient network is formed. The structure of the network is based on flower-like micelles bridged

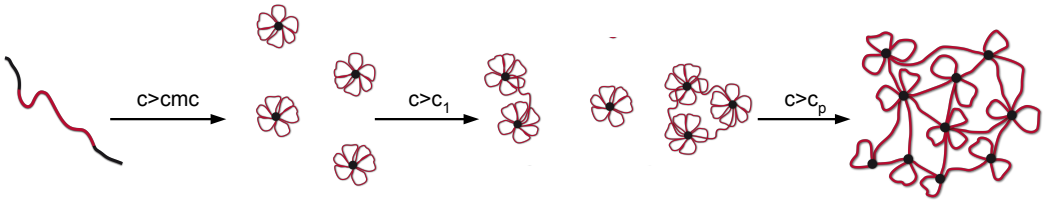

Figure 1.1: Sketch representing the aqueous behavior of telechelic polymers. At concentrations higher that the critical micellar concentration the polymers aggregate into flower-like micelles, at concentrations higher than an overlap concentration of the micelles (c_1), clusters of a few micelles form, and at concentrations higher than the percolation concentration (c_p) one cluster occupies the whole volume and a network is formed.

by telechelic polymers that have their two end-caps in two different micelles.

The structure has been successfully described with the model of a star proposed by Fetters et al. [21]. This model describes the flower-like micelles as chains emerging from the core, like a star polymer [22]. The model describes the small angle scattering data at the low concentration regime, where the micelles are isolated, and the concentrated where they are found to interact repulsively [13, 23].

Regardless of the lifetime of the bridges, the strength of the interaction is of about $1k_BT$ per chain. At constant concentration, an increase in the strength of the attraction leads to phase separation [24].

The rheological properties of networks formed by telechelic polymers in aqueous solutions have been studied in detail [25–28]. They exhibit shear thickening behavior prior to a sharp decrease in viscosity of several orders of magnitude [29]. Oscillatory shear measurements exhibit a rheological response that can be characterized by one single relaxation time τ_R and a plateau modulus G_0 that may be described by the Maxwell model. The relaxation time is related to the exit rate of the hydrophobic sticker from the micelle since it has been found to be the same as the relaxation times determined for micellar kinetics for surfactants with the same chain length. [27]

1.2.2 Associative polymers with multiple linkers

Polymers with many hydrophobic groups attached to a hydrophilic backbone associate in more complicated structures since the hydrophobes may associate with other hydrophobes

of the same polymer molecule or of different molecules. Depending on the polymer architecture and concentration, these polymers also form transient networks. They show a strong viscosity increase in the semi-dilute regime that is more pronounced if the grafting density is higher or the length of the stickers is increased. These solutions show a viscoelastic behavior. The rheological response presents a broader distribution of relaxation times compared to the HM-polymers [30, 31].

A theoretical work proposed by Rubinstein and Semenov [32] predicted that the dynamics in such systems is mainly controlled by intramolecular association. With increasing concentration, the polymer chain dynamics can be described by a sticky Rose model. The increase in viscosity with the concentration is due to the intermolecular association.

In the case of just a low number of hydrophobes per polymer, i.e. more that 2 but less than 10, considerably less work can been found in the literature. Recent investigations on 3-arm end-capped polymers showed a preference for intra-association instead of inter-association in agreement with the theory [33]

1.2.3 Addition of surfactants to telechelic polymers

The phase behavior of telechelic polymers may be modified by the addition of surfactants preventing the system from phase separation. The addition of small amounts of surfactants to associative polymer solutions induces a viscosity increase until the critical micellar concentration (cmc) of the surfactant is approached. However, an excess of surfactant induces a drastic decrease in viscosity [34–37].

Depending on both the concentrations of telechelic polymer and surfactant, the binding can be uncooperative or cooperative [38]. In terms of the structure, they form mixed aggregates with a relatively constant size when the number of hydrophobes is kept constant [39] and the surfactant aggregation number determined by SANS is lower than that observed in pure water [23].

1.3 Microemulsion-ABA polymer networks

The admixing of doubly hydrophobically end-capped polyethylene oxide (PEO) to microemulsions has been studied intensely with respect to the formation of transient net-

works. In terms of the phase behavior, they exhibit an extended monophasic region with a fluid sol region at low droplet and polymer concentrations and a viscoelastic region at higher droplet and polymer concentrations separated by a percolation line and a two phase region [40]. A typical phase diagram is depicted in Figure 1.2. The phase separation has a purely entropic origin since the increase in polymer configurations overcomes the entropy loss due to the phase separation and the formation of a dense phase [41]. The parameters

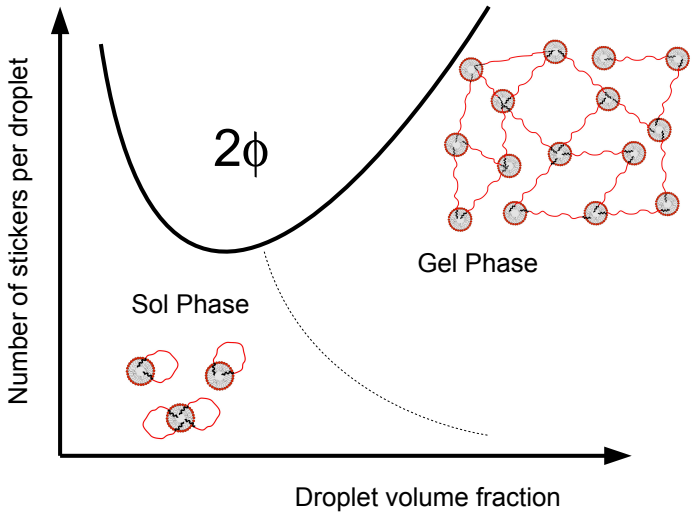

Figure 1.2: Phase behavior of micromulsions upon addition of telechelic polymers

that are controlling the system (see Figure 1.3) are the radius of the droplets R, distance between the microemulsion droplets d, the end-to-end distance of the polymer R_{ee}, the length of the sticker and the concentration of both, polymer, and droplets. The distance between the center of two neighboring droplets can be calculated assuming a primitive cubic arrangement of the droplets as

$$d = \sqrt[3]{\frac{1}{n}} = \sqrt[3]{\frac{4\pi R^3}{3\phi}} \tag{1.3}$$

where n is the number density and ϕ the droplet volume fraction. The surface-to-surface distance is $d^* = d - 2R$. The most important parameter is the ratio of the droplet distance and the polymer length, that for ideal chains is $R_{ee} = N^{1/2}l$ (N is the number

of monomers in the polymer chain and l the length of a monomer). If the inter droplet distance is larger than the end-to-end distance of the polymer, the polymers form loops decorating the droplets. If d is equal or shorter than R_{ee} bridges between droplets can be formed leading to the formation of clusters. By increasing the concentration of polymer, percolation can be achieved and a network is formed.

The length of the sticker determines the residence time of the hydrophobes in the oil droplets and, thus, the lifetime of the bridges [42].

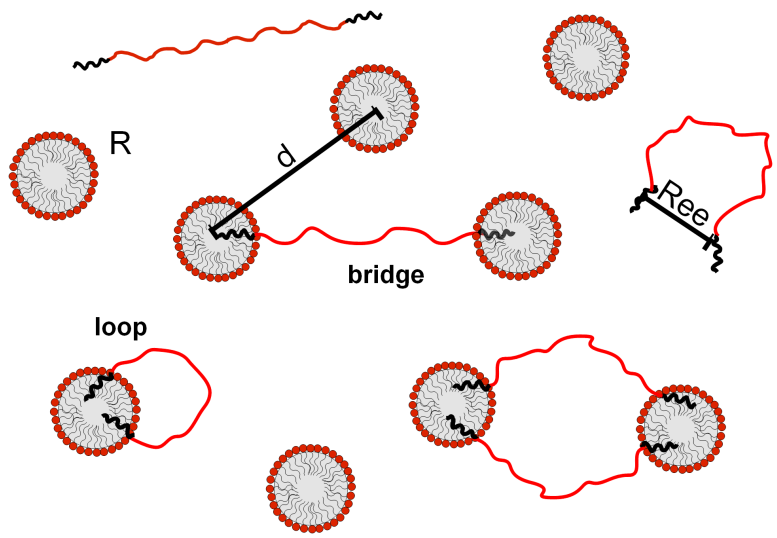

Figure 1.3: Sketch indicating the relevant parameters in the properties of telechelic polymers and microemulsion systems: the radius of the droplets R, the average distance between the droplets d given by the droplet size and volume fraction, the end-to-end distance of the hydrophilic polymer chain R_{ee}

The structural characterization of these systems by means of small-angle neutron scattering (SANS) [43–45] confirmed that the admixture of telechelic polymer does not lead to a change of the droplet size and they exhibit a net attractive interaction in the sol phase and a net repulsive interaction in the gel phase.

The gel phase exhibits a viscoelastic behavior with only one characteristic relaxation process. The relaxation time of the network depends on the length of the hydrophobic end-group. However, dynamic light scattering (DLS) experiments shows a rather complex behavior with various relaxation times [42, 46]. The inverse system consisting of a W/O microemusion with end-capped linear hydrophobic polymers has shown the same phase behavior, structure and dynamic properties as the classical system in water [47–49].

Computer simulations on such systems show that the minimum of the potential is

placed at a droplet separation similar to the end-to-end distance of the polymer [50]. Reference [51] showed that the fraction of polymers forming bridges was determined to have a strong dependence on the length ratio of the polymer end-to-end distance and the surface-to-surface distance between neighboring droplets for a lattice arrangement of the droplets. This fraction was independent of the number of polymers and independent of the polymer length and stiffness, except for very stiff or very long polymers. In fact, a universal behavior of the investigated properties was found, when examining the results versus the length ratio of the polymer end-to-end distance and the surface-to-surface distance between neighboring droplets for a hypothetical homogeneous droplet distribution [52]

A theoretical study by Bhatia and Russel [53] of two spheres with associative polymers predict that at a separation less than the end-to-end distance of the polymer ($d < N^{1/2}l$) the free energy exhibits an attractive minimum of $1k_BT$ per chain. They predict that for colloids in solution with associative polymers the interaction can be several k_BT, enough for phase separation. But for chains in good solvent, the attraction may be weaker, ans thus suppressing the tendency for phase separation. Helgeson and Wagner [54] go further for a very similar system and describe the potential by a Hard Sphere Double Yukawa (HSDY) potential. In this way they are able to predict the structure and phase behavior.

Further, the microemulsion networks are brittle according to the Griffith's theory of solid fracture [55]. The physical origin of this phenomenon is the reduction of the lifetime of links when they are under stress [56].

1.4 Motivation of this investigation

So far multi-armed (multi-functional) polymers have hardly been studied with respect to their ability of bridging microemulsions and their effects on the rheological properties. Furthermore, the aggregation behavior of telechelic star polymers in aqueous solutions should differ from that of their linear homolog.

Accordingly, such an extension of experimental studies on polymers with more complex architecture is undertaken here. In this study we were interested in the effect that end-capped star polymers of low functionality (f=2-4) have on the aggregation behavior in water and the formation of microemulsion networks , where the linear polymer ($f = 2$)

serves as a reference.

As model microemulsion, we chose the well known system of tetradecyldimethyl amine oxide (TDMAO) with decane as oil phase. This system is known to form low viscous microemulsions containing small spherical and rather monodisperse droplets [57]. This microemulsion has rather small droplets (R =2.4 nm) and have a interdroplet distance of d =13 nm for ϕ =0.033. The tailor made linear and star telechelic polymers have a larger length, i.e. $R_{ee} > d$. In this case, we expect the formation of a network. Our aim is to study the structure and dynamic properties of networks formed with polymers with varying architecture.

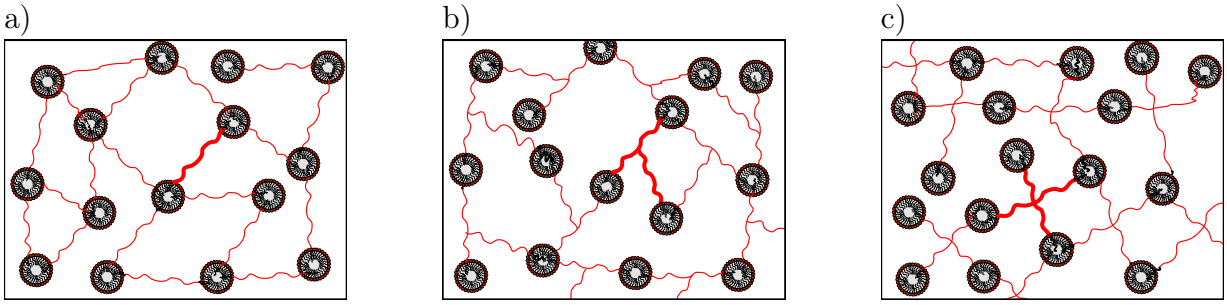

Figure 1.4: Schematic representation of microemulsion networks with end-capped star polymers with 2, 3 and 4 arms.

Moreover, we studied a microemulsion with composition Triton X100 / Brij 30 / Decane in water. Here, the droplets are larger (R = 6nm) and the interdroplet distance can be widely varied by changing the droplet concentration. For instance, for a droplet volume fraction of ϕ =0.033, d =34 nm and for ϕ =0.1, d =24nm. With this system we can study the case of $R_{ee} < d$. Our aim is to investigate the phase behavior, the structure and the dynamic properties of the microemulsion/polymer mixtures as a function of the polymer architecture.

In our experiments, we varied systematically the concentration of the added polymer, the length of the hydrophobic sticker, and, most importantly, the functionality, as given by the number of arms. By combining the results from SANS, rheology, and DLS, our aim was to derive systematic correlations between the architecture and amount of added polymer and the structural, dynamical, and rheological properties of the microemulsion/polymer mixtures.

The thesis is structured as follows. In Chapter 3 I present the characterization of the end-capped linear and star polymers and in Chapter 4 the behavior of the polymers in

aqueous solutions. Chapter 5 includes the investigation of a model microemulsion network based of TDMAO 100mM / Decane 35mM / water and a commercially available telechelic polymer $C_{18} - EO_{150} - C_{18}$ (Rewopal® 6000DS). In Chapter 6 the structure and dynamics of the microemulsion TDMAO 100mM / Decane 35mM / water with end-capped linear and star polymers is presented. Finally, Chapter 7 reports the phase behavior and structural investigation of the microemulsion Triton® X100/ Brij® 30/ Decane / water with end-capped linear and star polymers.

Chapter 2

Methods

2.1 Small-Angle Scattering

Scattering methods have become essential techniques for the characterization of microstructure and dynamics in the field of colloid and interface science [58].

In a small-angle experiment, a source produces a beam (neutron, X-rays, or light) scattered by the sample due to the inherent imhomogenities. The scattered intensity is measured by a detector at an angle θ, as depicted in Figure 2.1

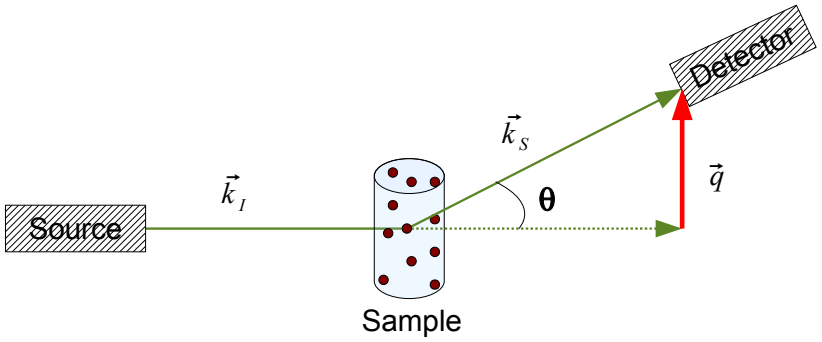

Figure 2.1: General set-up geometry of a scattering experiment with a light or neutron source, the sample with dispersed particles scatter light that may be collected at a certain angle θ by a detector.

The scattering wave vector **q** is defined as the difference between the incident wave

vector $\mathbf{k_I}$ and the scattered wave vector $\mathbf{k_S}$, and its magnitude is given by:

$$q = |\mathbf{q}| = \frac{4\pi n}{\lambda} sin\left(\frac{\theta}{2}\right) \tag{2.1}$$

The vector wave for the electric field of the incident beam of plane-wave, monochromatic electromagnetic radiation is defined for one particle by Equation 2.2 as function of the position $\mathbf{r}$ and the time t.

$$E(\mathbf{r}, t) = E_0 e^{i(\mathbf{k}\Delta\mathbf{r} - wt)} \tag{2.2}$$

E_0 is the maximal amplitude, $\mathbf{k}$ the wave vector whose magnitude is $|\mathbf{k}| = 2\Delta\pi/\lambda$, and the angular frequency is $w = 2\pi\nu/\lambda$, with λ being the wavelength of light in the medium. Assuming that there is a weak scattering so that most of the photons pass through the sample undeviated and the incident beam is not distorted significantly by the medium, the amplitude of the electric field of the scattered radiation $E_s(\mathbf{R}, t)$, in the position of detection $\mathbf{R}$ and at the time t is obtained by applying the Maxwell equations, and the total scattered electric field is the sum of the fields scattered by the individual particles:

$$E_s(\mathbf{R}, t) = -\frac{k^2 E_0}{4\pi} \frac{e^{i(kR - wt)}}{R} \sum_{j=1}^{N} b_j(\mathbf{q}, t) e^{-i\mathbf{q}\mathbf{R}_j(t)} \tag{2.3}$$

where $b_j(\mathbf{q}, t)$ is the scattering length of the particle j and it is defined by:

$$b_j(\mathbf{q}, t) = \int_{V_j} \Delta\eta(\mathbf{r}_j, t)\ e^{-i\mathbf{q}\mathbf{r}_j} d^3 r_j \tag{2.4}$$

Here, $\Delta\eta(\mathbf{r}_j, t)$ is the scattering length density at the position $\mathbf{r}_j$ of the particle j and at the time t. The dependence on the scattering material properties (dielectric constant, refractive index, density) depends on the type of radiation. The measured quantity is the scattered intensity and it is related to the electric field by $I(\mathbf{q}, t) = |E(\mathbf{q}, t)|^2$. Therefore, the scattered intensity can be expressed by the following equation:

$$I_s(\mathbf{q}, t) = E_s E_s^{:} = \frac{E_0^2}{R^2} \sum_{j=1}^{N} \sum_{i=1}^{N} b_j(\mathbf{q}, t) b_j^{:}(\mathbf{q}, t) e^{-i\mathbf{q}(\mathbf{R}_j - \mathbf{R}_j)} \tag{2.5}$$

The ensemble average on time $\langle I(q)_t \rangle$ is necessary in order to obtain structural information. It is assumed that the sample is spatially isotropic in order to set it as a function of the modulus of the scattering vector $\mathbf{q}$. In addition, if a dilute system is considered, the

particles are enough spread out so that their behavior can be considered as uncorrelated and the scattered intensity can be approximated by the equation:

$$I_s(q) = \frac{E_0}{R^2} \sum_{j=1}^{N} \left\langle |b_j(\mathbf{q})|^2 \right\rangle = \frac{NE_0}{R^2} \left\langle |b_j(0)|^2 \right\rangle P(q) \tag{2.6}$$

$P(q)$ is the normalized intensity form factor of the system and describes the structure of the individual particle in the system and it is given by:

$$P(q) = \frac{\langle |b_j(\mathbf{q})|^2 \rangle}{\langle |b_j(0)|^2 \rangle} \tag{2.7}$$

In a concentrated system the interaction of the particles between each other has to be taken in consideration. The structure factor takes into account the interparticle correlations and is defined as:

$$S(q) = \frac{1}{N} \sum_{j=1}^{N} \sum_{i=1}^{N} \left\langle e^{-i\mathbf{q}(\mathbf{R}_j - \mathbf{R}_k)} \right\rangle \tag{2.8}$$

Finally, we obtain that the scattering intensity (Eq. 2.9) is the product of the scattering by N uncorrelated particles ($Nb^2(0)P(q)$) and the structure factor, defined by equation 2.8, which represents the modification of the intensity due to the spacial correlation between the particles.

$$I_s(q) \;=\; \frac{NE_0}{R^2} \left\langle |b_j(0)|^2 \right\rangle P(q)\; S(q) \tag{2.9}$$

2.1.1 Small Angle Neutron Scattering (SANS)

The SANS experiment requires a source of neutrons. There are several types of neutron sources depending on the mechanism to produce the neutrons, on which will depend the energy and the rate of neutrons emitted by the source. The neutrons are particles that have an associated wavelength. The maximum from the Maxwell distribution of wavelengths of the neutron beam is the thermic De Broglie wavelength, $\lambda = h/\sqrt{2mk_BT}$, that is related to the mass of a neutron m and the temperature T. Here, h is the Plank constant and k_B is the Boltzmann constant.

Subsequently, a small interval of wavelengths is selected and the beam is focused on

the sample by a collimator. The scattered beam is measured by a bidimensional detector that is situated at a distance R and an angle θ.

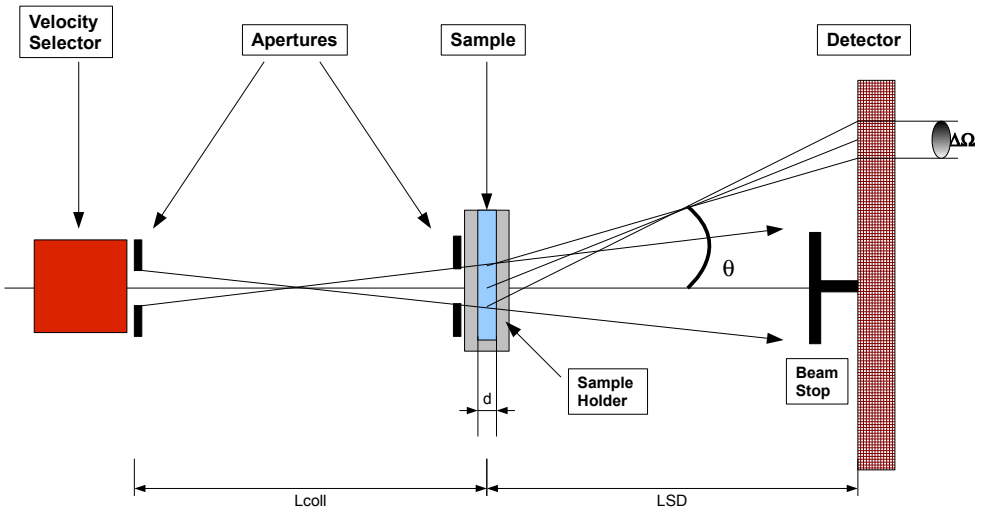

Figure 2.2: Scheme of a pin-hole SANS: The neutrons pass a velocity selector; the divergence by two apertures in the collimation of length L_{coll}; then the neutrons hit the sample. The non-scattered neutrons are absorbed by the beam-stop. The scattered neutrons are collected by the position sensitive area detector at a distance L_{SD}.

The general set-up of a pin-hole SANS experiment is schematized in Figure 2.2. The detected intensity at one pixel on the detector is:

$$I_i^0 = \Phi_0(\lambda)E(\lambda)Ad\Delta\Omega_i T\frac{d\Sigma}{d\Omega}(q) \tag{2.10}$$

where Φ_0 is the incident flux, $E(\lambda)$ the detector efficiency, A the illuminated sample area, $d\Sigma/d\Omega(q)$ the cross section, and $\Delta\Omega_i$ the solid angle of a detector element. $\Delta\Omega_i$ can be calculated from the area of a pixel a_{px}, and the sample-detector distance D:

$$\Delta\Omega_i = \frac{a_{px}}{D^2} \tag{2.11}$$

All the intensities have to be normalized on the number of incident neutrons. This can be done for example by dividing the measured intensity by a monitor count rate M. The intensity is given as the ratio between the number of neutrons detected at the detector and

those detected at a monitor situated before the instrument

$$I^0 = \frac{I}{M} \tag{2.12}$$

The incident intensity is:

$$I_0^o = \Phi_0(\lambda)E(\lambda)A = \frac{I_0 f_{att}}{M} \tag{2.13}$$

I_0 is the sum of neutrons detected at the detector, f_{att} the attenuation factor of the attenuator employed to measure the direct beam, and M is the neutrons detected at the monitor. If the incident beam were measured, this would saturate the detector. Therefore an attenuator (different thickness of Plexiglass) is placed before the collimation.

The measured intensity of the sample requires a correction by substraction of the contributions of the empty cell and background. The background noise corresponds to the electronic noise, the cosmic radiation, and the detection of neutrons which have not passed through the sample, e.g. scattered neutrons from neighboring experiments.

Therefore, the corrected and normalized intensity at a given pixel of the detector can be expressed as:

$$I^o_{sample,i} = \left(\frac{I_{S,i}}{M_S} - \frac{I_{B,i}}{M_B}\right) - \frac{T_S}{T_{EC}}\left(\frac{I_{EC,i}}{M_{EC}} - \frac{I_{B,i}}{M_B}\right) \tag{2.14}$$

The index B stands for the background, EC for the empty sample holder, and S for the sample in the sample holder. The factor $\frac{T_s}{T_{EC}}$ accounts for the attenuation of the beam by the sample.

The cross section can be calculated from the intensity from Equation 2.10.

$$\frac{d\Sigma}{d\Omega}(Q) = \frac{I^0_{S,i}/T_S}{dI^o_0 \Delta\Omega_i} \tag{2.15}$$

The SANS measurements were performed on several instruments, located at different neutron facilities in Europe. The specifications of each set of measurements are as follow:

SANS 2D, ISIS, England

The SANS measurements of Chapter 3 were performed at the pulsed source ISIS, England, on the SANS 2D time-of flight instrument. The sample-detector distance, as well as the

collimation were 4m. The wavelength was from 2 to 14 Å. The range of the scattering vectors was $0.05 < q < 8$ nm^{-1}. The SANS data were treated according to standard procedures for absolute scaling, radial averaging, and background subtraction. The absolute scaling was done with a monodisperse, partially deuterated polymer blend. The detection efficiency was not taken into account. Each sample was measured for a total of 15 minutes of acquisition time.

PAXY, LLB, France

The SANS measurements of Chapter 6 were performed at the spectrometer PAXY of the Laboratoire Léon Brillouin (LLB, CEA-CNRS, Saclay, France) with a neutron wavelength of 5 Å and sample-to-detector distances of 1.145 and 5.045 m. The covered range of the magnitude of scattering vectors was $0.08 < q < 3.3$ nm^{-1}. For some samples an additional configuration at 5.045 m and 15 Å was measured going down to 0.04 nm^{-1}. Sapphire cells with a 1 mm beam path were used for very viscous samples and Quartz Hellma cells (110-QS) of 1 or 2 mm of thickness for the low viscous samples.

KWS 2, FRMII, Germany

The SANS measurements of Chapter 5 were done on the instrument KWS2 of the Jülich Center for Neutron Sciences at the Forschungs-Neutronenquelle Heinz Meier-Leibnitz (JCNS at FRMII, Munich, Germany) [59], with scattered neutrons recorded on a 128x128 ^{3} 6Li scintillation detector with CCDs detector of 68x68 cm^2. Wavelengths of 5.0 and 1.2 Å (FWHM 20%) and sample-to-detector distances of 1.2, 8 and 20 m were employed with collimation at 4, 8 and 20 m respectively, thereby covering a q-range of $0.02< q <5.2$ nm^{-1}. The sensitivity of the detector was accounted for by comparing to the scattering of a 1 mm sample of water. Samples were contained in quartz cuvettes (QX, Hellma) of 0.5, 1 and 2 mm thickness and measured at $25°C$.

KWS 1, FRMII, Germany

The SANS measurements of Chapter 7 were done on the instrument KWS1 of the Jülich Center for Neutron Sciences at the Forschungs-Neutronenquelle Heinz Meier-Leibnitz (JCNS

at FRMII, Munich, Germany) [59], with scattered neutrons recorded on a 128x128 ^{3} 6Li scintillation detector with CCDs detector of 68x68 cm^2. A wavelength of 4.5 Å (FWHM 10%) and sample-to-detector distances of 1.2, 7.7 and 20 m were employed with collimation at 4, 8 and 20 m respectively, thereby covering a q-range of $0.03 < q < 5.2$ nm^{-1}. The sensitivity of the detector was accounted for by comparing to the scattering of a 1 mm sample of water. Samples were contained in quartz cuvettes (QX, Hellma) of 1 mm thickness and measured at $25°C$.

The sample thickness, the transmission, the dead time, and the electronic background were accounted for, and the background due to the scattering of the beam with an empty cell was subtracted. Hence, the scattering intensities given still contain the scattering contribution of the solvent and the incoherent scattering. The obtained data was finally radially averaged and merged using standard routines with the software BerSANS [60]. The obtained curves were fitted with SASfit [61], a program for fitting simple structural models to small angle scattering data. The mathematical equations of the form and structure factor, which were employed, are listed below.

2.1.2 Model-Free Analysis of the Small-Angle Scattering Data

Guinier approximation

Regardless of the structure of the particle, at very low angles, the scattering curve can be described by the forward scattering I_0 and the radius of gyration R_G around its center of mass by the Guinier approximation [62]:

$$\lim_{q \to 0} I(q) = I_0 \exp \frac{-q^2 R_G^2}{3} \tag{2.16}$$

The applicability of the Guinier approximation is restricted to low angles ($qR_G << 1$) and when the interparticle interactions are negligible [63].

Porod Law at the high q limit

At the high q limit, where very small distances are probed, there are no inter-particle effects and the intensity decays with fourth power of q . The strength depends on the

contrast $\delta\rho$ and the surface area S [64].

$$I(q) = 2\pi S \Delta\rho^2 q^{-4} \tag{2.17}$$

When the surface is not smooth, the Porod law can be extended by changing the power law from 4 to $n = 6 - d$, being d the fractal dimension that can be extracted from n.

2.1.3 Model Analysis of the Small-Angle Scattering Data

The scattering intensity of monodisperse, spherically symmetric aggregates can be described by the following expression:

$$I(q) = nV^2 \Delta\rho^2 P(q) S(q) \tag{2.18}$$

where n is the number density of scatterers, V their volume, $\Delta\rho$ the difference between the coherent scattering length density of the micellar unit and the one of the solvent, P(q) the form factor, and S(q) the structure factor that takes into account the interactions between the aggregates.

Form factor

Generalized Gauss Coil

The curves of polymer coils swollen in good solvents can be described with a generalized Gauss coil form factor.

$$^1 NV^2 \Delta\rho^2 P(Q)_{coil} = I(0) \frac{U^{\frac{1}{2\nu}} \Gamma(\frac{1}{2\nu}) - \Gamma(\frac{1}{\nu}) - U^{\frac{1}{2\nu}} \Gamma(\frac{1}{2\nu}, U) + \Gamma(\frac{1}{\nu}, U)}{\nu U^{\nu}} \tag{2.19}$$

with

$$\Gamma(a, x) = \int_x^{\infty} t^{a-t} \exp(t) dt \tag{2.20}$$

and

$$U = (2\nu + 1)(2\nu + 2) \frac{Q^2 R_G^2}{6} \tag{2.21}$$

ν is the excluded volume parameter from the Flory mean Field theory. Typical values are $\nu = 1/3$ (partially precipitated in poor solvents), $\nu = 1/2$ (thermally relaxed in "theta"-

solvents), and $\nu = 3/5$ (swollen in good solvents) [65].

Homogeneous sphere

Microemulsion droplets can be regarded as homogeneous spheres or core-shell particles depending on the scattering length density profiles.

$$P_s(q) = \left(3\frac{sinqR - qRcosqR}{(qR)^3}\right)^2 \tag{2.22}$$

Core-shell

The form factor of a core-shell particle with a core radius R_{core} and a shell thickness t_{shell} is defined as:

$$V\Delta\rho^2 P(q)_{shell} = [\Delta\rho_{shell}(V_{core} + V_{shell})f(qR_{shell}) - (\Delta\rho_{shell} - \Delta\rho_{core})V_{core}f(qR_{core}))]^2 \tag{2.23}$$

where $R_{shell} = R_{core} + t_{shell}$, $\Delta\rho_{core}$ and $\Delta\rho_{shell}$ are the scattering length density contrasts between the core and the solvent and between the shell and the matrix respectively. V_{core} and V_{shell} are the volumes of the core and the shell respectively, and f(qR) is defined as:

$$f(qR) = \left(3\frac{sinqR - qRcosqR}{(qR)^3}\right)^2 \tag{2.24}$$

Scattering length density contrast

The scattering length density contrast $\Delta\rho$ between the sample can be calculated as the difference of the scattering length density of the aggregates ρ_{agg} and the mean scattering length density of the sample $\bar{\rho}$:

$$\Delta\rho = \rho_{agg} - \bar{\rho} \tag{2.25}$$

ρ_{agg} and $\bar{\rho}$ are the volume fraction pondered sums of the scattering length densities of the individual components of the aggregates and the sample, respectively. The scattering length density of all the components used in this project are listed in Table 2.1.

Log-Normal Size Distribution

When considering polydisperse particles a size distribution has to be introduced. In this case, a log-normal distribution was chosen:

$$L_N = N/R\sigma(2\pi)^{1/2}exp(-[ln(R) - \sigma]^2/2\sigma^2) \tag{2.26}$$

where N is the number density of spheres. The polydispersity index PDI of this distribution is identical to the variance σ.

Structure Factor

The structure factor is related to the direct correlation function

$$S(q) = \frac{1}{1 - nC(q)} \tag{2.27}$$

The direct correlation function C(q) is the Fourier transform of c(r), that can be calculated by the Ornstein-Zernike integral equation [66]

$$h(r_{12}) = c(r_{12}) - n \int c(r_{13})h(r_{23})dr_3 \tag{2.28}$$

Here, there are two unknown functions and, therefore, mathematical approximations, called closures, are needed. These are typically the Percus Yevick (PY) for short range interactions and Hypernetted-chain (HNC) for long range, and Roger-Young (RY) closure for thermodynamically consistent S(q) where PY and HNC are used jointly [67].

We studied different systems with different type of interactions. Thus, several structure factors were employed. In the following, we present a compilation of all the used structure factors.

Hard Sphere Structure Factor

The potential in a hard sphere model is described by equation 2.29.

$$\frac{U(r)}{k_B T} = \begin{cases} \infty & \text{for } 0 < r < \sigma \\ 0 & \text{for } r > \sigma \end{cases} \tag{2.29}$$

where σ is the hard sphere diameter ($\sigma = 2R_{HS}$).

With this restrictions and using the Percus-Yevick closure relation [68], the structure

factor S_{HS} can be calculated as follows [69, 70]:

$$S_{HS}(q, R_{HS}, \phi_{HS}) = \frac{1}{1 + 24\phi_{HS}\frac{G(q,R_{HS},\phi_{HS})}{R_{HS}q}} \tag{2.30}$$

where ϕ_{HS} is the hard sphere volume fraction and the function $G(q, R_{HS}, \phi_{HS})$ is equal to:

$$G(q) = \alpha\frac{sinA - AcosA}{A^2} + \beta\frac{2AsinA + (2 - A^2cosA - 2)}{A^3} + \gamma\frac{-A4cosA + 4[(3A^2 - 6)cosA + (A^3 - 6A)sinA + 6]}{A^5} \tag{2.31}$$

and the parameters α, β, γ, and A are defined by the following equations:

$$\alpha = \frac{(1 + 2\phi_{HS})^2}{(1 - \phi_{HS})^4} \tag{2.32}$$

$$\beta = -6\phi_{HS}\frac{(1 + \phi_{HS}p/2)^2}{(1 - \phi_{HS})^4} \tag{2.33}$$

$$\gamma = \frac{\phi_{HS}\alpha}{2} \tag{2.34}$$

$$A = 2R_{HS}q \tag{2.35}$$

Sticky Hard Sphere

The interaction of systems with short range attraction and excluded volume repulsion may be described by the Sticky Hard Sphere model proposed by Baxter [71]. In this model, the interaction potential is defined by the following expression:

$$\frac{U(r)}{k_BT} = \begin{cases} \infty & \text{for} \quad 0 < r < \sigma \\ \ln\frac{12\tau\Delta}{\sigma+\Delta} & \text{for} \quad \sigma < r < \sigma + \Delta \\ 0 & \text{for} \quad r > \sigma + \Delta \end{cases} \tag{2.36}$$

where the hard sphere diameter is $\sigma = 2R_HS$, and Δ the width of the potential. When applied, the limit $\Delta \to 0$ is taken. Thus, only a single parameter, the so-called stickiness parameter τ, characterizes the adhesive strength. The Sticky Hard Sphere structure factor

is defined as:

$$S_{\mathrm{SHS}}(q, R_{\mathrm{HS}}, \phi_{HS}, \tau) = \frac{1}{1 - C(q)} \tag{2.37}$$

where ϕ_{HS} is the hard sphere volume fraction and the correlation function C(q) is equal to:

$$\begin{aligned} C(q) = \; & 2\tfrac{\eta\lambda}{\kappa}\sin\kappa - 2\tfrac{\eta^2\lambda^2}{\kappa^2}(1-\cos\kappa) - \\ \Big\{ \; & \alpha\kappa^3(\sin\kappa - \kappa\cos\kappa) + \beta\kappa^2(2\kappa\sin\kappa - (\kappa^2-2)\cos\kappa - 2) \\ & + \tfrac{\eta\alpha}{2}\left((4\kappa^3 - 24\kappa)\sin\kappa - (\kappa^4 - 12\kappa^2 + 24)\cos\kappa + 24\right)\Big\} \; \times \; 24\tfrac{\eta}{\kappa^6} \end{aligned}$$

The parameters κ, η, ϵ, γ, λ, μ, α and β are described by the following equations:

$$\kappa = 2qR_{\mathrm{HS}} \tag{2.38a}$$

$$\eta = \phi_{HS}\left(\frac{2R_{\mathrm{HS}} + \Delta}{2R_{\mathrm{HS}}}\right)^3 \tag{2.38b}$$

$$\epsilon = \tau + \frac{\eta}{1-\eta} \tag{2.38c}$$

$$\gamma = \phi_{HS}\frac{1 + \eta/2}{3\,(1-\eta)^2} \tag{2.38d}$$

$$\lambda = \frac{6}{\eta}\left(\epsilon - \sqrt{\epsilon^2 - \gamma}\right) \tag{2.38e}$$

$$\mu = \lambda\eta(1-\eta) \tag{2.38f}$$

$$\beta = -\frac{3\eta\,(2+\eta)^2 - 2\mu\,(1 + 7\eta + \eta^2) + \mu^2(2+\eta)}{2\,(1-\eta)^4} \tag{2.38g}$$

$$\alpha = \frac{(1 + 2\eta - \mu)^2}{(1-\eta)^4} \tag{2.38h}$$

Yukawa Hard Sphere

For systems with a long-range repulsion, a Hard-Sphere-Yukawa potential (Eq. 2.39) was chosen, as it has been proven to successfully describe the long range repulsion in non-ionic interacting systems [72, 73].

$$U(r) = \begin{cases} \infty & \text{for } 0 < r < R_{HS} \\ Aexp(-b(r - R_{HS}))/r & \text{for } r > R_{HS} \end{cases} \tag{2.39}$$

where R_{HS} is the hard sphere radius. For $r > R_{HS}$, the radius and the volume fraction of the hard sphere in this model are constrained to be defined by those of the sphere form factor. A describes the maximum strength of the interaction and b its range. The structure factor S(q) is obtained by solving the Ornstein-Zernike equation for the direct correlation function C(r), which may be obtained under the rescaled mean spherical approximation (RMSA) [74].

2.2 Dynamic Light Scattering (DLS)

Dynamic light scattering (DLS) experiments are based on the analysis of the temporal fluctuations of the scattered intensity due to density or concentration fluctuations of the sample. The experimental set-up is just as in other scattering experiments (see Figure 2.2) where the detector is connected to a correlator that computes the correlation function from the intensity fluctuations as a function of time (see Figure 2.3). These intensity fluctuations can be calculated from the temporal correlation function of the photoncount rate of the detector.

$$C(\tau) = \langle n(0)n(t)\rangle \tag{2.40}$$

where n(0) is the count-rate in a time interval ∂t and t the delay time. The intensity correlation function is defined as

$$g^2(t) = \frac{\langle I_s(0)I_s(t)\rangle}{\langle I_s(0)\rangle^2} \tag{2.41}$$

The electric field autocorrelation function $g_1(t)$ is defined as the ensemble of the product of the scattered field at time $t = 0$ and the one after a time, t.

$$g^1(t) = \frac{\langle E_s(0)E_s(t)\rangle}{\langle E_s(0)\rangle^2} \tag{2.42}$$

In the case of Gaussian scatterers and ergodic systems the intensity autocorrelation function $g^{(2)}(t)$ measured in a homodyne experiment is related to the field autocorrelation function $|g^{(1)}(t)|$ by the Siegert relation [75]:

$$g^{(2)}(t) = 1 + B|g^{(1)}(t)|^2 \tag{2.43}$$

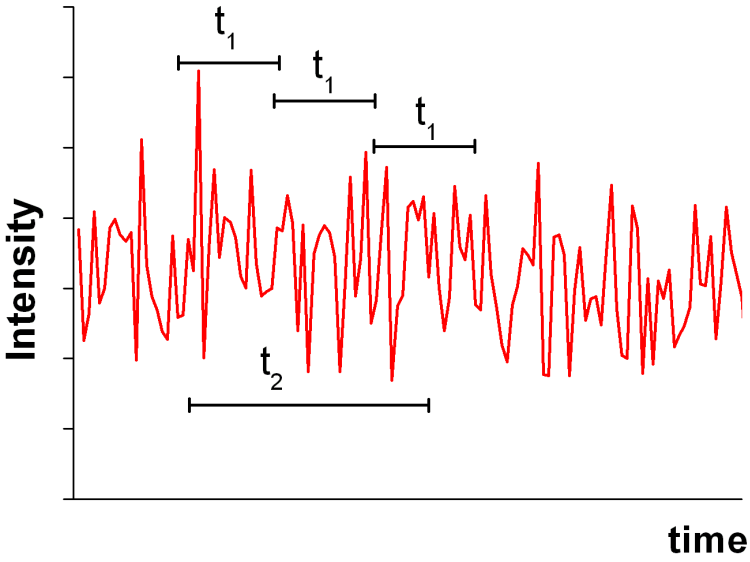

Figure 2.3: Representation of the intensity fluctuations as a function of time of a dynamic light scattering experiment indicating a delay time t_1 and a longer delay time t_2.

where B is an instrumental constant that reflects the deviations from the ideal correlation. It should have an ideal value of 0.33 on this set-up.

2.2.1 Dilute regime

For monodisperse particles in solution the field correlation function decays exponentially, $|g_1| = 1 + e^{-\Gamma_i t}$ with the decay rate $\Gamma = D \cdot q^2$, where D is the diffusion coefficient of the particle and q is the magnitude of the scattering wave vector. In polydisperse systems the correlation function g_1 is expressed in terms of a normalized distribution of decay rates $G(\Gamma)_i$:

$$|g_1| = \int_0^\infty G(\Gamma)_i e^{-\Gamma_i t} d\Gamma \tag{2.44}$$

Experimentally, $|g^{(1)}(t)|$ is obtained through the measured photocount correlation function.

The quantity measurable is the diffusion coefficient D. The particle shape is related to the diffusion coefficient. In the simple case of a spherical object, the Stokes-Einstein relation can be used to relate the diffusion coefficient with the hydrodynamic radius of the particle:

$$R_H = \frac{k_B T}{6\pi\eta D_T} \tag{2.45}$$

where k_B is the Boltzmann constant, T the absolute temperature and, η the dynamic viscosity of the medium.

2.2.2 Semidilute and concentrated regimes

The decay of the electric field autocorrelation function $g^{(1)}(t)$ of a colloidal system can be described by a single exponential function followed, in the case of complex systems, by one or two stretched exponential functions

$$|g^{(1)}(t)| = a_1 \cdot e^{-t/\tau_1} + \sum a_i \cdot e^{(-t/\tau_i)^{\beta_i}} \tag{2.46}$$

The parameters a_i are the amplitudes for the respective relaxation modes with decay times τ_i and $\beta_i (0 < \beta < 1)$ is a measure of the width of the distribution of relaxation times [76]. The further β differs from 1, the broader the distribution of relaxation rates is. The first relaxation mode is typically the simple diffusive mode that is related to the size of the diffusing particles or elementary structural units. The other modes describe more complex relaxation processes as they may arise from dense packing or other interactions between the colloidal particles.

In some cases, when it was not clear how many modes the relaxation function had, a CONTIN analysis [77] was performed to obtain further qualitative information.

Equation 6.17 for the relaxation is of a generalized Kohlrausch-Williams-Watt (KWW) type [78–80] and allows, in addition to the conventional diffusive relaxation, for two additional relaxation modes. The slower relaxation processes, as described by the stretched exponentials, can arise from different mechanisms that can be distinguished by the q-dependence of the relaxation time τ, that typically follows a power law ($1/\tau \sim q^{\alpha}$). For the case of viscoelastic polymer networks a q-independent ($\alpha = 0$) relaxation has been reported [81, 82]. The exponent β itself is typically smaller than 1 for such slower relaxation modes.

The effective diffusion coefficient is related to the fast relaxation time as $D_{eff} = 1/(\tau_f q^2)$ and thus related to the hydrodynamic radius R_H through the Stokes-Einstein equation (Eq. 2.45)

Dynamic Light Scattering (DLS) measurements were performed at 25°C using a setup

consisting of an ALV/LSE-5004 correlator, an ALV CGS-3 goniometer, and a He-Ne Laser with a wavelength of 632.8 nm. Cylindrical sample cells were placed in an index matching toluene vat. Intensity autocorrelation functions were recorded under different angles between 50° and 130°.

2.3 Fluorescence Correlation Sepctroscopy (FCS)

In an FCS experimente, the fluctuations of fluorescence intensity over time inside a confocal volume are measured. This technique allows the determination of translational the diffusion coefficients of fluorescent probes. The autocorrelation function $G(t)$, for a one component system in the absence of phosphorescence, is given by [83]:

$$G(t) = G(0)\left(1+\left(\frac{t}{\tau}\right)^{\alpha}\right)^{-1}\left(1+\frac{1}{S^2}\left(\frac{t}{\tau}\right)^{\alpha}\right)^{-0.5}(1-T+T\exp(t/\tau_f)) \tag{2.47}$$

S, the structure parameter, is the ratio of the transversal radius ω_{xy} to the longitudinal radius ω_z of the confocal volume ($S = \omega_{xy}/\omega_z$) In this way, the diffusion time of a fluorescence molecule can be calculated as:

$$\tau_D = \frac{w_0^2}{4D} \tag{2.48}$$

provided that the confocal volume is known.

The second term in Eq. 2.47 accounts for the existence of a non fluorescent triplet state [84], where τ_f is the relaxation time of the triplet state, and T is the average fraction of fluorescent molecules that are in the triplet state.

In a crowded environment, the diffusion gets anomalous and the particle mean displacement obeys a power law

$$< r^2(t) >= 6\Gamma t^{\alpha} \tag{2.49}$$

The exponent α is the same as in Eq. 2.47. If it differs from 1, the diffusion is said to be anomalous, and if $\alpha < 1$, it subdiffusive.

The effective diffusion coefficient is defined by $D(t) = \Gamma t^{\alpha-1}$. Anomalous diffusion takes place in crowded media and has been used to describe FCS data of viscous systems [85].

FCS measurements were performed with the Leica TCS SP5 II system. Excitation of

Nile Red was performed using an Ar ion laser with a wavelength of 514nm. The confocal volume was determined using the same experimental set-up and measuring a solution of 0.62 nM of Rhodamin 6G in MiliQ water and assuming a diffusion coefficient value of $4.0 \times 10^{-10} m^2 s^{-1}$ [86].

2.4 Rheology

The study of the flow properties of self-assembling systems is relevant from a fundamental point of view, and also for the potential applications of new materials. Therefore, rheology finds applications in a great variety of fields [87–89].

2.4.1 Viscosity

The zero shear viscosity can be measured with the help of a calibrated capillary viscometer, that is a u-shaped piece of glassware with a reservoir and a measuring bulb connected by a capillary. The time that the liquid takes to pass through two calibrated marks is related to the viscosity through Hagen-Piseuille´s law:

$$\frac{dV}{dt} = \frac{\pi R^4 |\Delta P|}{8 L \eta} \tag{2.50}$$

where V is the volume of the liquid, t the time, R the internal radius, L the length of the capillary, ΔP the pressure difference between the two ends, and η the dynamic viscosity of the fluid.

The solution of the differential equation gives

$$\frac{\eta t}{\rho} = A + K t^2 \tag{2.51}$$

with ρ the density of the fluid. A and K are constants that depend on the viscometer geometry. Normally, A can be neglected and the dependence of the viscosity with the time is linear $\eta = \rho K t$.

To measure the zero shear viscosity of samples with viscosities under 200 $mPas$, a micro-Oswald capillary viscometer (Schott) was used at a constant temperature $(25.0 \pm 0.1C)$. By determining the capillary suction time t of a given volume of around 2 ml, the viscosity at a defined cross-section (radius R), could be described via the Hagen–Poiseuille equation

2.50. K is a device-specific constant, given by certified calibration measurements of Schott (model: Ic ($\sim 0.03\ mm^2/s^2$), IIc ($\sim 0.3\ mm^2/s^2$)).

2.4.2 Oscillating Rheology

In an oscillatory measurement, a sinusoidal shear strain at a constant frequency ω and with an amplitude γ_0 is applied, a steady sinusoidal strain or stress results with a fixed phase angle δ between the input and the output signals. For a sinusoidal shear strain $\gamma(t) = \gamma_0 sin(\omega t)$, the stress σ will oscillate sinusoidally as

$$\sigma = \sigma_0 sin(\omega t + \delta) \tag{2.52}$$

Since the stress always leads the strain, the phase angle δ between stress and strain is positive. The complex dynamic shear modulus $G^*(\omega)$ defined by $G'(\omega) + iG''(\omega)$ is given by

$$G^*(\omega) = (\sigma_0/\gamma_0)exp(i\delta) \tag{2.53}$$

The storage shear modulus $G'(\omega) = (\sigma_0/\gamma_0)cos\delta$ is the measure of the elastic energy stored and recovered, and the loss shear modulus $G''(\omega) = (\sigma_0/\gamma_0)sin\delta$ is a measure of the energy dissipated as heat in the cyclic deformation.

2.4.3 High Frequency measurements

The Piezoelectric Rotary Vibrator (PVR) [90] consists of a piezo drive, the lower plate, and the column that connects them (see Figure 2.4). The piezo drive is composed of a six-spoke wheel made out of an aluminum alloy plate. Each spoke has two piezo elements. Three spokes receive a constant amplitude U_{ref} and apply an angular momentum of frequency independent amplitude M on the central column and its plate. The angular deflection φ of the plate is detected by the other three spokes connected to the input of the amplifier, which measures the complex voltage $U = |U|e^{i\Theta}$.

At very small rotary vibrations, the voltage U is proportional to φ, the incoming signal is φ/M and it is related to the sum of the restoring torques of the empty PVR D_0, and the contribution from the material D^*. Therefore, the complex torque of the material is given

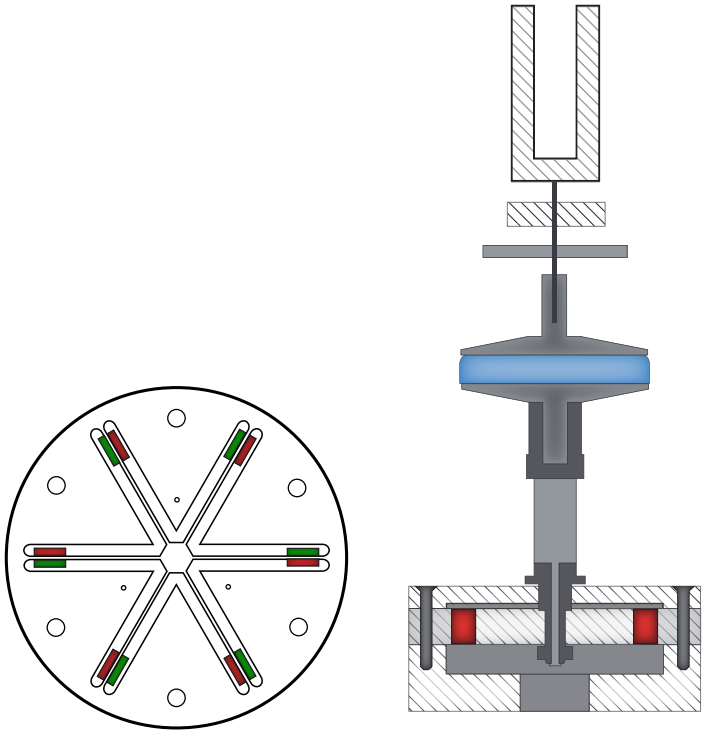

Figure 2.4: Schematic representation of the rheometer with the PRV unit and the top view of the wheel with the piezo elements.

by

$$\Delta = \left(\frac{M}{\varphi}\right) - \left(\frac{M}{\varphi}\right)_0 = D^*_{app}(\omega) \tag{2.54}$$

The resonance of the chosen plate must be taken into account assuming that the restoring torque D_1 of the column and the inertia Θ_1 get into resonance at $\omega_1 = D_1/\Theta_1$. R is the plate radius, d the gap and ρ the density of the material.

$$D^*_{corr}(\omega) = \frac{\Delta\left(1 - \frac{\omega^2}{\omega_1^2}\right)^2}{1 - \frac{\Delta}{D_1}\left(1 - \frac{\omega^2}{\omega_1^2}\right)} \tag{2.55}$$

The restoring momentum D^* is equal to the reaction torque of the viscoelastic vibration. In the case of a plate-plate geometry, the complex modulus G^* is related to D^*_{corr} via

$$D^*_{corr}(\omega) \approx \frac{\pi}{2}\frac{R^4}{d}\left(G^*(\omega) - \frac{\omega^2 d^2 \rho}{2} + ...\right) \tag{2.56}$$

where R is the radius of the plates, d the gap distance, ω the angular frequency, ρ the density of the material. Note that the dependency with the radius is R^4 and with the gap distance $1/d$, meaning that in order to achieve more sensitivity, it is better to use larger

plates that lower the gap distance.

Oscillating Rheology measurements were performed with two instruments

Malvern Instrument

Rheology measurements were carried out using a Bohlin Gemini 150 rheometer equipped with a high-frequency extension with a piezo rotary vibrator [90]. A plate-plate geometry of aluminum was used with a diameter of 40mm. This set-up then allows for measurements from 10 up to 2000 Hz. This overlaps nicely with the conventional set-up in which frequencies of 0.001-20 Hz are covered. The Gap size was 0.1mm and the deformation 0.1.

Ares AG2

Oscillatory measurements presented in chapter 5 were performed at the Rheology Laboratory at the University of Guadalajara (Guadalajara, Jalisco, Mexico) on the instrument Ares AG2 from TA Instruments. A cone-plate geometry of 40mm diameter was used.

2.4.4 Maxwell model for viscoelastic behavior

The relaxation function G(t) describes the decay of the stress after the deformation of the material as a function of time. The complex modulus is related to G(t) via

$$G^* = G(0) + i\omega \int_0^\infty G(t) \exp -i\omega t dt \tag{2.57}$$

Assuming that G(t) decays exponentially with time, $G(t) = G_0 \exp(-t/\tau_R)$, and G(0) is zero, one obtains:

$$G^*(\omega) = \frac{i\omega\tau_R G_0}{1 - \omega\tau_R} \tag{2.58}$$

The elastic modulus G' is described by the real part

$$G' = G_0 \frac{\omega^2\tau^2}{1 + \omega^2\tau^2} \tag{2.59}$$

and the viscous modulus by the imaginary part

$$G'' = G_0 \frac{\omega\tau}{1 + \omega^2\tau^2} \tag{2.60}$$

2.5 Materials and Sample Preparation

2.5.1 List of chemicals

Table 2.1 presents a list of the relevant technical data and physical properties of all the chemicals that were used. The chemical structure is depicted in Figures 2.5 and 2.6.

Chemical	Molecular Formula	Provider	$M_w/gmol^{-1}$	ρ^m/gml^{-1}	$\rho_{SLD}/10^{10}cm^{-2}$
D_2O	D_2O	Euroisotop	20	1.1056	6.36
d_8THF	C_4D_8O	Aldrich	80.16	0.985	6.37
THF	C_4H_8O	Merck	72.11	0.89	0.184
Decane	$C_{10}H_{22}$	Fluka	142.29	0.73	-0.448
TDMAO	$C_{16}H_{35}NO$	Huntsman	257.46	1	-0.23
Triton ® X100	$C_{14}H_{22}OEO_{9.5}$	Aldrich	526	1.07	
Brij ® 30	$C_{12}H_{25}EO_4$	Aldrich	362	0.95	
Rewopal ®	$C_{18} - EO_{150} - C_{18}$	Evonik	7130	1.1	0.263
Nile Red	$C_{20}H_{18}N_2O_2$	Fluka	318.37		
Rhodamine 6G	$C_{28}H_{31}N_2O_3Cl$	Fluka	479.01		

Table 2.1: List of relevant technical data and properties of the chemicals: Chemical structure, provider, molecular weight M_w and mass density ρ^m given by the provider, and scattering length density ρ_{SLD}

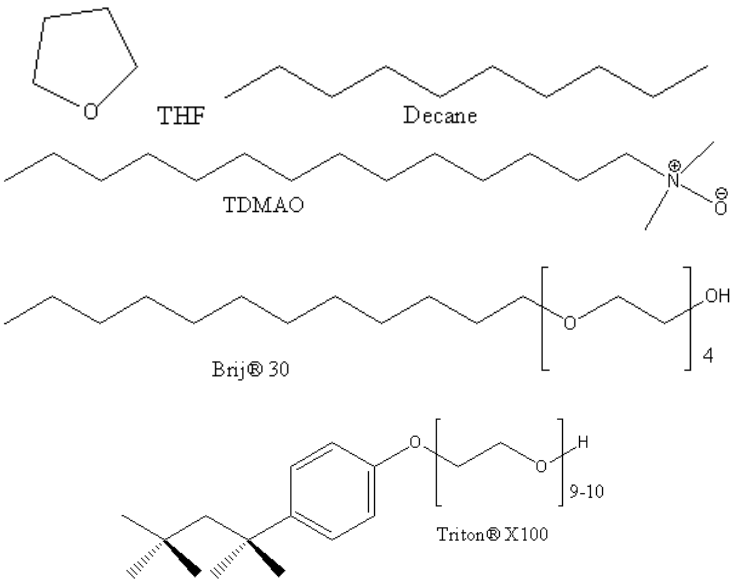

Figure 2.5: Chemical structure of the oils and the surfactants.

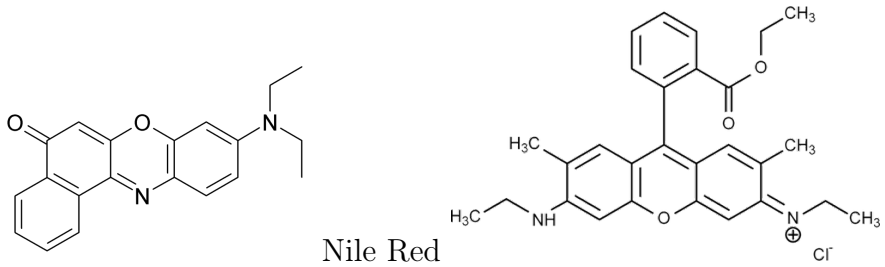

Nile Red Rodamin 6G

Figure 2.6: Chemical structure of the fluorescent dyes.

2.5.2 Microemulsion

TDMAO/Decane/Water

Tetradecyl dimethyl amine oxide (TDMAO, $C_{14}H_{29}N(CH_3)_2O$) was obtained from Huntsman (Empigen OH 25, 24-26%) as a gift. The solutions were freeze-dried until the amount of water reached a value of 2.5 wt%, which was determined via Karl-Fischer-Titration. N-decane ($\geq$ 98%) was obtained from Sigma Aldrich and used as supplied. The samples were prepared by taking the required amount of a stock solution of 200 mM of surfactant. The appropriate amount of oil and water was added to achieve the final composition of the monodisperse [57] microemulsion with 100 mM TDMAO/ 35 mM decane /water.

TX100/B30/Decane/D_2O

The appropriate amounts of Triton® X100 (TX100), Brij® 30 (B30) and Decane ($\geq$ 98%) were purchased from Sigma Aldrich and were used as supplied. They were weighted to obtain a final mixture with final composition 38.9 wt% TX100/ 31.4 wt% B30/ 29.7 wt% Decane, which was diluted with D_2O (Euroisotop, > 99% D) to obtain a final dipersed volume fraction of 14.65%. The turbid solution was stired for 5 hours until an homogeneous transparent solution was obtained. The microemulsion was kept under 25°C to avoid segregation

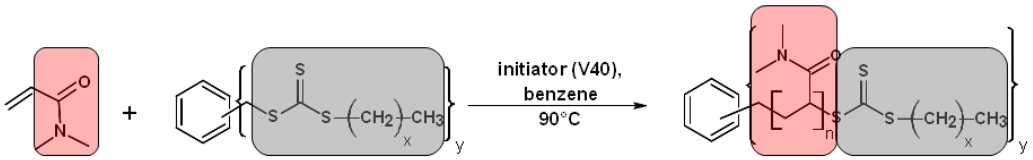

Figure 2.7: One-step preparation of end-capped linear and star polymers via RAFT polymerization using N,N -dimethylacrylamide (DMA) and tailored chain transfer agents.

2.5.3 End-capped Star Polymers

The telechelic star polymers were obtained from the group of André Laschewsky (U. Potsdam). All details concerning synthesis and characterization of the polymers are given elsewhere [91]. The polymers were synthesized using reversible addition fragmentation chain transfer (RAFT) polymerization. The reaction schema is depicted in Figure 2.7. Multifunctional chain transfer agents for RAFT polymerization, designed for this purpose, were used for the polymerization of the hydrophilic monomer N,N-dimethylacrylamide. The polymers are based on hydrophilic blocks with n units, with 2, 3 and 4 arms, with an aliphatic end chain of 4, 12, or 18 carbon units (see Fig. 2.7). Table 2.2 gives the molecular weight as weight (M_w), and number (M_n) average as well as the polydispersity index (PDI= M_w/M_n) of all polymers employed in this study.

Entry	Polymer	f	C_{x+1}	$M_n{}^{t,a}$/KDa	$M_n{}^b$/KDa	$M_w{}^b$/KDa	PDI^b	n	R_{ee} / nm
#1	$(C_4PDMA)_1$	1	C4		53	61	1,15	533	32.4
#2	$(C_4PDMA)_2$	2	C4	87.2	84	96	1.14	422	28.8
#3	$(C_4PDMA)_3$	3	C4	91.3	147	169	1.14	493	31.2
#4	$(C_4PDMA)_4$	4	C4		21.9	24.5	1.12	53	10.3
#5	$(C_4PDMA)_4$	4	C4	85.0	104	111	1.07	261	22.6
#6	$(C_{12}PDMA)_2$	2	C12	24.1	nd	nd			
#7	$(C_{12}PDMA)_2$	2	C12	48.2	590	61	1.05	293	24.0
#8	$(C_{12}PDMA)_2$	2	C12	92.6	112	121	1.08	563	33.3
#9	$(C_{12}PDMA)_3$	3	C12	33.4	nd	nd			
#10	$(C_{12}PDMA)_3$	3	C12		66.5	68.9	1.04	221	20.9
#11	$(C_{12}PDMA)_3$	3	C12	71.0	80.7	84.1	1.04	269	23.0
#12	$(C_{12}PDMA)_3$	3	C12		86.3	87.9	1.06	289	23.8
#13	$(C_{12}PDMA)_3$	3	C12	87.4	104.2	116.1	1.11	348	26.2
#14	$(C_{12}PDMA)_4$	4	C12	44.4	nd	nd			
#15	$(C_{12}PDMA)_4$	4	C12		77.6	83.4	1.07	193	19.5
#16	$(C_{12}PDMA)_4$	4	C12		91.8	96.6	1.05	229	21.2
#17	$(C_{12}PDMA)_4$	4	C12	97.6	110.9	118.1	1.06	277	23.4
#18	$(C_{18}PDMA)_2$	2	C18	24.0	nd	nd			
#19	$(C_{18}PDMA)_2$	2	C18	98.0	nd	nd			
#20	$(C_{18}PDMA)_3$	3	C18	37.6	nd	nd			
#21	$(C_{18}PDMA)_3$	3	C18	83.0	nd	nd			
#22	$(C_{18}PDMA)_4$	4	C18	43.3	nd	nd			

Table 2.2: Polymer structure, number of arms f, sticker length. [a]Expected molar mass $M_n{}^t$. [b]Molar mass as weight (M_w), and number (M_n) average as determined by MALLS-GPC [91] DMA units per arm (n) as calculated from M_n and polydispersity index (PDI) and end-to-end distance of 2 arms (R_{ee}) calculated as $< R_{ee}^2 >= C_\infty 2Nl^2$ ($C_\infty = 9.1$) [92] of all the polymers included in this study.

Chapter 3

Characterization of the telechelic linear and star polymers in non-selective solvent

The size of the polymers, given by the molecular weight is a very important parameter that will determine the properties in solution. Telechelic polymers aggregate in aqueous solutions into flower-like micelles. At a certain concentration the end-capped chains can bridge two micelles and, therefore, form networks [24]. A similar scenario occurs when adding telechelic polymer to microemulsions. The interaction potential and thus the elasticity strongly depends on the degree of stretching of the chains [18]. Consequently, the length of the polymer chain plays a very important role and has to be accordingly investigated.

This chapter presents a Small Angle Neutron Scattering study of hydrophobically modified linear and star polymers in a non-selective, good solvent. The molecular weight, the second virial coefficient and the radius of gyration were determined.

3.1 Small Angle Neutron Scattering in d_8-THF.

We performed Small Angle Neutron Scattering experiments of solutions of different concentrations of the polymer in deuterated THF, in order to determine the molecular weight and the radius of gyration. THF is a good solvent both for the poly(dimethylacrylamide) chain as for the alkyl chains and, consequently, the polymers will not tend to aggregate in the considered concentration regime. Figure 3.1 shows, as an example, the SANS patterns

of $(C_{12}PDMA)_3$ of concentrations 1, 2 and 3 wt% in d_8-THF.

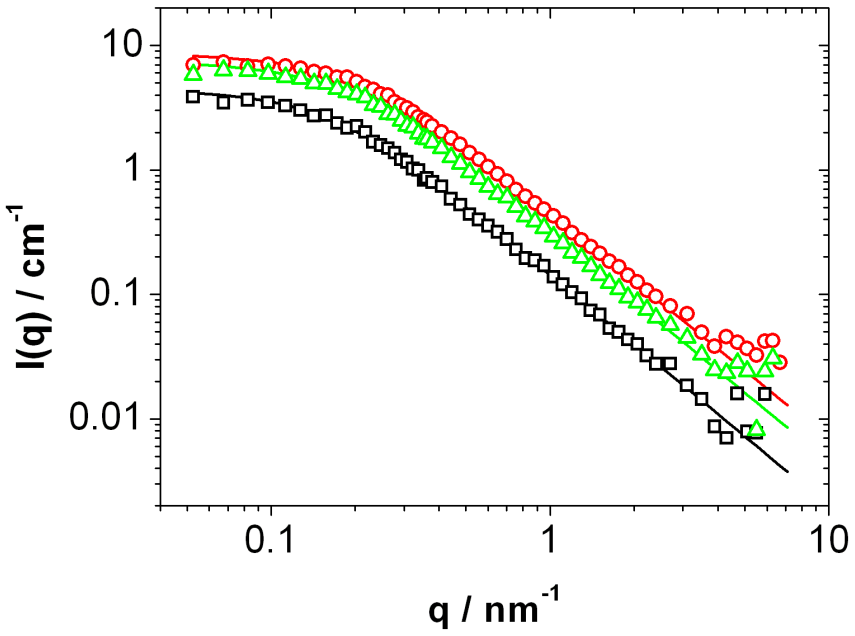

Figure 3.1: SANS patterns of the aggregates of $(C_{12}PDMA)_3$ (sample 10) in d_8-THF at concentrations of 1 (squares), 2 (triangles) and 3 wt% (circles). Solid lines: fits using a generalized Gauss model described by Eq. 2.19

The curves exhibit the typical form of a polymer coil. At the low q limit, we did a Guinier analysis that allowed the determination of the forward scattering and the radius of gyration. The results for the three polymer concentrations for all polymers are collected in Table 3.1. Moreover, the extended Porod Law predicts at high q that the scattered intensity follows a power law of q^n. in the case of polymer coils, n is related to the excluded volume parameter ν as its inverse $n = 1/\nu$. From the slope at high q values of the log-log plot we can determine that the excluded volume parameter is ~ 0.55. Fully collapsed chains have a value of $\nu = 1/3$. Ideal Gaussian chains are expected to have a value of $\nu = 0.5$ and for fully swollen coils $\nu = 0.6$. Real chains in good solvents have experimentally values closer to 0.6 [65].

Polymer	$c \cdot 10^2/g \cdot ml^{-1}$	Gauss coil			Guinier	
		R_G/nm	ν	I(0)/cm^{-1}	Rg/nm	I(0)/cm^{-1}
#1	1.04	6.84	0.55	2.84	5.3 ± 0.1	2.46 ± 0.03
	2.15	6.01	0.54	5.04	4.9 ± 0.1	4.55 ± 0.06
	3.15	5.53	0.54	6.03	4.6 ± 0.1	5.48 ± 0.07
#2	1.03	8.45	0.55	4.05	6.8 ± 0.3	3.6 ± 0.1
	2.06	7.05	0.55	6.63	5.9 ± 0.3	6.1 ± 0.1
	3.12	6.62	0.55	7.15	5.6 ± 0.2	6.6 ± 0.1
#3	1.04	11.3	0.55	6.40	8.5 ± 0.3	5.5 ± 0.1
	2.07	8.66	0.55	8.26	6.7 ± 0.2	7.13 ± 0.09
	3.16	7.80	0.56	10.1	5.8 ± 0.2	8.5 ± 0.2
#4	1.05	4.06	0.46	1.52	3.5 ± 0.1	1.38 ± 0.02
	2.22	3.87	0.48	2.98	3.31 ± 0.07	2.71 ± 0.03
	3.14	3.72	0.48	3.87	3.02 ± 0.07	3.39 ± 0.04
#5	1.05	9.05	0.51	5.39	6.4 ± 0.1	4.25 ± 0.07
	2.26	7.67	0.52	8.48	5.6 ± 0.1	6.93 ± 0.08
	3.15	6.86	0.52	9.67	5.10 ± 0.06	8.12 ± 0.06
#6	1.05	6.71	0.54	2.90	5.4 ± 0.2	2.60 ± 0.06
	2.12	5.95	0.55	2.57	4.8 ± 0.2	2.27 ± 0.05
	3.12	5.60	0.55	5.88	4.6 ± 0.1	5.31 ± 0.07
#7	1.05	9.33	0.55	4.77	7.4 ± 0.5	4.2 ± 0.2
	1.97	7.64	0.55	7.78	6.3 ± 0.2	7.1 ± 0.1
	3.14	6.83	0.55	8.10	5.7 ± 0.2	7.4 ± 0.1
#8	1.04	7.16	0.53	3.33	5.7 ± 0.2	2.93 ± 0.06
	2.21	6.03	0.53	5.67	4.8 ± 0.1	4.97 ± 0.07
	3.13	5.73	0.54	6.58	4.6 ± 0.1	5.83 ± 0.08
#9	1.05	8.57	0.54	4.32	6.7 ± 0.3	3.72 ± 0.03
	1.94	7.11	0.53	6.48	5.5 ± 0.1	5.60 ± 0.08
	3.11	6.62	0.53	8.46	5.3 ± 0.1	7.5 ± 0.1
#10	1.05	8.14	0.53	4.28	5.9 ± 0.2	3.52 ± 0.07
	2.13	6.75	0.55	3.35	5.3 ± 0.2	2.91 ± 0.05
	3.15	6.16	0.54	7.47	4.9 ± 0.1	6.59 ± 0.08
#11	1.04	8.73	0.54	4.47	6.4 ± 0.3	3.7 ± 0.1
	2.13	7.70	0.54	7.42	5.9 ± 0.2	6.4 ± 0.1
	3.13	6.95	0.55	8.55	5.5 ± 0.1	7.5 ± 0.1
#13	1.05	8.23	0.51	4.65	6.0 ± 0.2	3.81 ± 0.07
	2.09	7.15	0.52	7.52	5.27 ± 0.09	6.25 ± 0.07
	3.14	6.48	0.52	8.49	4.88 ± 0.08	7.18 ± 0.07
#14	1.04	9.16	0.52	5.50	6.38 ± 0.2	4.30 ± 0.08
	1.97	7.92	0.53	7.97	5.7 ± 0.1	6.54 ± 0.09
	3.15	7.18	0.53	9.95	5.28 ± 0.09	8.26 ± 0.08
#15	1.05	9.15	0.56	4.58	8.6 ± 0.9	4.5 ± 0.2
	2.24	7.45	0.55	7.73	7.1 ± 0.6	7.5 ± 0.2
	3.14	6.73	0.55	8.00	5.6 ± 0.2	7.3 ± 0.1
#16	1.05	8.43	0.53	4.32	6.3 ± 0.2	3.64 ± 0.07
	2.24	7.26	0.54	7.11	5.6 ± 0.2	6.1 ± 0.1
	3.14	6.49	0.54	8.30	5.1 ± 0.2	7.3 ± 0.1

Table 3.1: Structural parameters obtained by fitting the SANS patterns of linear and star telechelic polymers of several concentrations to the equation of a generalized Gauss coil (Eq. 2.19): radius of gyration R_G, excluded volume parameter ν, and results of the Guinier analysis (Eq. 2.16) at low q: forward scattering $I(0)$ and radius of gyration R_G.

A more detailed structural picture can be obtained by a model analysis of the curves. We have already determined that the polymers in THF are relatively swollen coils. For this reason, the model of the coil needs to include the excluded volume parameter ν. This can be done with the general expression for the a Gauss polymer coil described by equation 2.19. This model has three fit parameters, the forward scattering, I(0), the radius of gyration of the polymer coil, R_G, and the excluded volume parameter ν.

The fitted parameters of the samples of the polymers at 3 different concentrations in d_8-THF are collected in table 3.1. One observes that the radius of gyration decreases with increasing concentration. The radius of gyration obtained by the Guinier fit is smaller than the one obtained from the generalized Gauss coil expression.

3.1.1 Molecular weight

The molecular weight can be determined from the concentration dependence of the forward scattering I(0), that is described by the Zimm equation [93]

$$\frac{c}{I(0)} = \frac{d^2 N_{AV}}{\Delta\rho^2 M_W}\left(1 + 2A_2 M_W c\right) \tag{3.1}$$

where d is the polymer density (1.05 g/cm^3), N_{AV} the Avogadro constant, $\Delta\rho$ the difference of the scattering length densities of polymer and solvent, and c_g the weight concentration of polymer.

The scattering length density variation $\Delta\rho$ was calculated as the difference of the scattering of the polymer (assumed to be that of PDMA) and the average scattering length density of the sample $\rho_{sample} = \phi_{pol}\rho_{pol} + (1 - \phi_{pol})\rho_{solvent}$. The scattering length densities are listed in Table 2.1.

Figure 3.2 shows the Zimm plots for scattering intensity at zero angle $I(0)$ (see Table 3.1) at different polymer concentrations in d_8-THF. Using Eq. 3.1, from the intercept the molecular weight can be obtained and and the second virial coefficient from the slope. The wight average molecular weight and the second virial coefficient A_2 are listed in Table 3.2. For comparison, the wight average and number average molar masses obtained from Size Exclusion Chromatography with light scattering detection (SEC-MALLS). The molecular weight M_W is somewhat larger, but in very good agreement, as the one determined with SEC-MALLS.

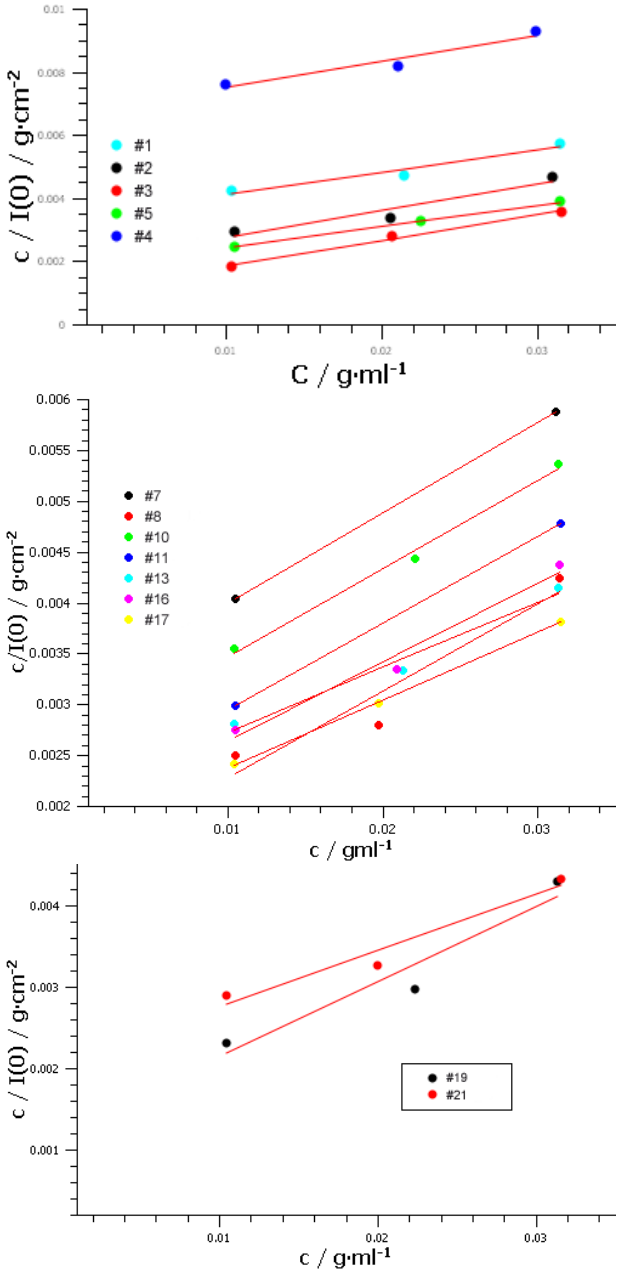

Figure 3.2: Zimm plots for the a)xC4-PDMA, b)xC12-PDMA, c)xC18-PDMA polymers obtained from SANS measurements of the polymers in d8-THF. $c/I(0)$ (being $I(0)$ the forward scattering is plotted against the polymer concentration c. The linear fits correspond to Eq. 3.1 and the results are in Table 3.2.

3.1.2 Radius of Gyration

As already stressed above, the radius of gyration obtained for polymer solutions in THF decreases with the polymer concentrations. This means that the radius of gyration shrinks with increasing polymer concentration due to the osmotic pressure of the surrounding coils.

Sample Code	Polymer	n[a]	M_n^a KDa	M_w^a KDa	M_W^b KDa	$A_2^b \cdot 10^4$ / $mol \cdot cm^3 \cdot g^{-2}$	R_G^c/nm	$A_2^c \cdot 10^4$ $mol \cdot cm^3 \cdot g^{-2}$
#1	(C_4PDMA)	533	53	61	67 ± 7	1.6 ± 0.4	7.93	2.51
#2	(C_4PDMA)$_2$	422	84	96	120 ± 33	1.9 ± 0.7	9.70	1.60
#3	(C_4PDMA)$_3$	493	147	169	219 ± 24	1.8 ± 0.3	15.66	2.26
#4	(C_4PDMA)$_4$	52	22	25	34 ± 2	1.49 ± 0.04	4.626	1.46
#5	(C_4PDMA)$_4$	261	104	111	128 ± 2	1.8 ± 0.5	11.48	2.2
#7	(C_{12}PDMA)$_2$	296	59	61	73	1.96	7.53	1.82
#8	(C_{12}PDMA)$_2$	563	112	121	158 ± 64	1.9 ± 2	11.95	2.13
#10	(C_{12}PDMA)$_3$	221	67	69	86 ± 5	1.9 ± 3	8.28	2.11
#11	(C_{12}PDMA)$_3$	269	81	84	104 ± 4	1.4 ± 3	10.08	2.14
#12	(C_{12}PDMA)$_3$	289	83	88	108	$1.89 \pm \infty$	10.11	2.54
#13	(C_{12}PDMA)$_3$	348	104	116	108 ± 11	1.4 ± 2	10.38	1.81
#16	(C_{12}PDMA)$_4$	229	92	97	120 ± 17	1.7 ± 3	9.83	1.74
#17	(C_{12}PDMA)$_4$	277	111	118	131 ± 1	1.5 ± 2	10.83	1.58
#19	(C_{18}PDMA)$_2$				186 ± 90	2.0 ± 2	12.01	1.89
#21	(C_{18}PDMA)$_3$				109 ± 18	$1.5\pm$	10.27	2.21

Table 3.2: Polymer Parameters.[a] Molecular weight average in weight, M_w, and number, M_n measured by MALLS-GPC, and DMA units per arm n calculated(from M_w). [b] Molecular weight M_w and second virial coefficient A_2 obtained via Zimm plot (Eq. 3.1).[c] Radius of gyration at infinite dilute conditions $R_G(0)$ and second virial coefficient A_2 obtained from the concentration dependence of the radius of gyration (Eq. 3.3).

The concentration dependence of the radius of gyration can be obtained from the following expression [94, 95]:

$$R_G(c) = R_G(0)\left[\sqrt{\frac{M_W}{RT}\frac{d\Pi}{dc}}\right]^{-1} \tag{3.2}$$

This assumption is valid if $c < 2c^*$. The overlap concentration c^* is related to A_2 through $c^* \cong 1/A_2 M_W$. Therefore, the assumption holds and the radius of gyration at infinite dilution may be expressed as

$$\frac{1}{R_G(c)^2} = \frac{1}{R_G(0)^2}(1 + 2A_2 M_w c) \tag{3.3}$$

Consequently, the linear fit of $1/R_G(0)$ vs. c yields the radius of gyration at infinite dilute conditions and the second virial coefficient.

We can compare this experimental values with the theoretical radius of gyration, given by [22]

$$R_G^2 = (3 - 2/f)\frac{C_\infty (N/f) l^2}{6} \tag{3.4}$$

where N is the total number of monomer units in the polymer, l is the length of a polymer, f is the number of arms in the star and C_∞ is a correction constant that accounts for the local stiffness of the polymer chain. PDMA in a good solvent like water has a value of $C_\infty = 9.3$ [92]

Consequently, the radius of gyration scales with f^- and $M_W^{0.5}$. Figure 3.3 shows the radius of gyration extrapolated to zero concentration as a function of the weight average molecular weight M_W. We fitted the data to a power law of the molecular weight in the form of M_W^x and the best result was obtained for $x = 0.5$. However, there were no significant difference with the number of arms.

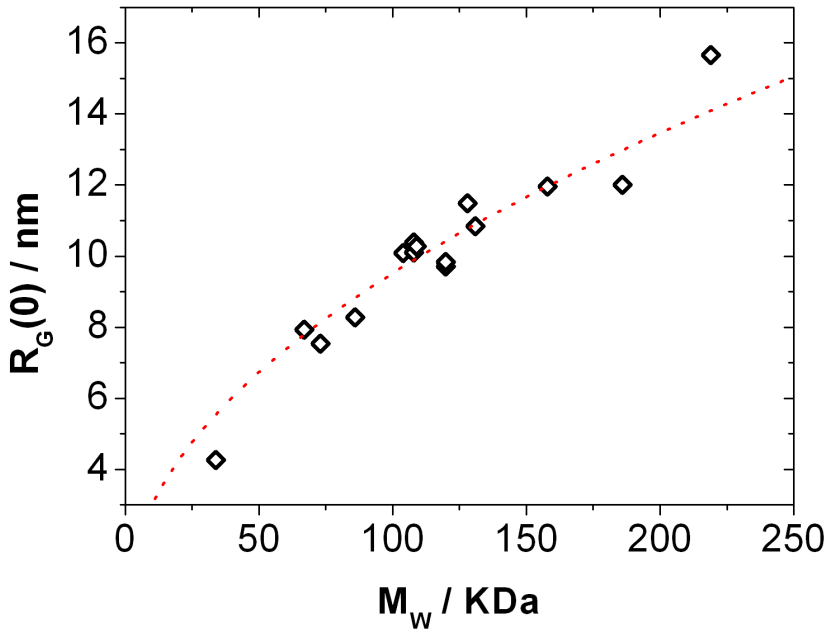

Figure 3.3: Radius of gyration R_G as a function of the molecular weight M_W determined with equations 3.3 and 3.1, respectively with the scattering data of telechelic linear and star polymer solutions in d_8-THF measured on SANS2D, ISIS. The dotted line is the fit to a power law of the molecular weight in the form of Mx, the best result was obtained for $R_G(0) = 0.925 M_W^{0.5}$.

The second virial coefficient A_2 results obtained with Eqs. 3.1 and 3.3 are in very good agreement with each other (see Figure A.1). A_2 is in all cases positive. Thus, meaning repulsive interaction. This is typical to occur for polymers in a good solvent. A_2 is expected

to scale with the molecular weight as $A_2 \propto M^{3\nu-2}$ [96, 97]. However, we did not observe any tendency, perhaps because the data is very noisy (see Figure A.1).

3.2 Summary

As a first step, pure polymers were dissolved in a good non-selective solvent to evaluate their molecular weight, gyration radii and 2nd virial coefficient. The SANS curves of the novel end-capped linear and star poly(dimethylacrylamide) were modeled with the expression for a general Gauss coil yielding the forward scattering $I(0)$, radius of gyration R_G and the excluded volume parameter ν. The excluded volume parameter was found to be between 0.5 and 0.6 indicating that the coils are rather swollen. The molecular weight determined from the concentration dependence of the forward scattering via Zimm plot is in very good agreement with the ones obtained by SEC-MALLS [91]. The radius of gyration decreases with the polymer concentration and the value at infinite dilution $R_G(0)$ scales with $M_W^{0.5}$. The second virial coefficient A_2 was obtained from the concentration dependence of the forward scattering and of the radius of gyration. Both methods yielded very similar results. A_2 is in all cases positive as it is expected for polymers in good solvents and no strong dependence on the molecular weight was obtained.

Chapter 4

Structure and Dynamics of telechelic star polymers in aqueous solutions

Due to the long hydrophilic DMA blocks that are common to the polymers prepared, all of them are well soluble in water, and thus, their behavior in aqueous solution could be characterized by means of rheology, DLS, and SANS. Depending on the length of the alkyl end groups incorporated, hydrophobic aggregation is expected as it is known for previously studied linear and star like hydrophobically end-capped polymers [15, 27, 98, 99].

4.1 C4 end-capped linear and star polymers

The C4 end-capped polymers were soluble in water and the solutions were low viscous. The end alkyl chains with 4 carbon atoms are rather short in comparison with the length of the hydrophilic chains (see Table 2.2). Consequently, it is not clear a priori whether the polymer molecules will aggregate or not.

In order to characterize the structure of aqueous solutions of C4 end-capped PDMA, we performed SANS measurements of solutions of $(C_4PDMA)_2$, $(C_4PDMA)_3$ and $(C_4PDMA)_4$ solutions with 1 and 5 wt% concentration (see Figure 4.1).

The curves exhibit the typical form of a polymer coil. The extended Porod Law predicts at high q that the scattered intensity follows a power law of q^n. in the case of polymer coils, n is related to the excluded volume parameter ν as its inverse $n = 1/\nu$. From the slope at high q values of the log-log plot we can determine that the excluded volume parameter is

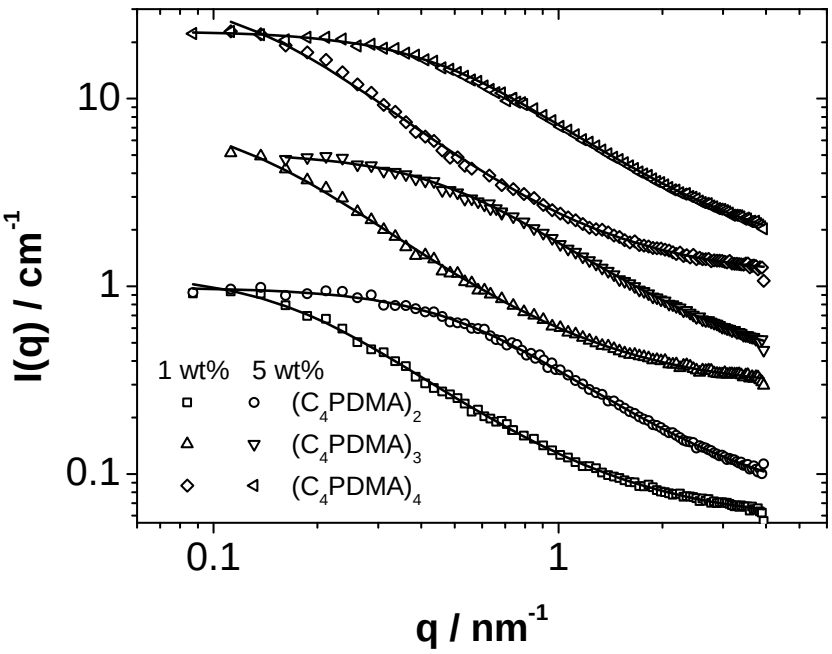

Figure 4.1: SANS patterns of $(C_4PDMA)_2$ (#2 in Table 2.2), $(C_4PDMA)_3$ (#3) and $(C_4PDMA)_4$ (#5) at 1 and 5 wt% in D_2O measured at PAXY. The curves are vertically shifted a factor 5 for $(C_4PDMA)_3$ and a factor 15 for $(C_4PDMA)_3$. Solid lines: Fits using a generalized Gauss expression (Eq. 2.19)

~ 0.65. Fully collapsed chains have a value of $\nu = 1/3$. Ideal Gaussian chains are expected to have a value of $\nu = 0.5$ and for fully swollen coils $\nu = 0.6$. Real chains in good solvents have experimentally values closer to 0.6 [65].

A more detailed structural picture can be obtained by a model analysis of the curves. Since the polymers in water are very swollen coils, the model of the coil needs to include the excluded volume parameter ν. This can be done with the general expression for the a Gauss polymer coil described by equation 2.19. This model has three fit parameters, the forward scattering $I(0)$, the radius of gyration of the polymer coil R_G, and the excluded volume parameter ν. This model fits very good the experimental data and thus seems to be a very good description of the structure of the polymer solutions. The parameters obtained from the fits are in Table 4.1

One observes from the SANS results (see Table 4.1) that the excluded volume factor ν is larger that 0.6 indicating that the polymers are highly swollen in water. The radius of gyration R_G scales with the molecular weight of the polymer and decreases with the

Polymer	M_w / KDa	R_G / nm	c / wt%	I(0) / cm^{-1}	ν	R_G / nm
$(C_4PDMA)_2$ #2	96	14.41	1	1.12	0.65	7.66
			5	0.93	0.65	2.52
$(C_4PDMA)_3$ #3	169	12.11	1	1.58	0.65	10.66
			5	0.97	0.65	2.73
$(C_4PDMA)_4$ #5	111	7.08	1	1.76	0.62	10.00
			5	1.08	0.65	2.81

Table 4.1: Structural parameters of C_4 end-capped polymers. Molecular weight by MALLS-SEC in water–acetonitrile M_W, radius of gyration calculated from Eq. 4.1, concentration of polymer in D_2O c, and parameters obtained by fitting the SANS data with Eq. 2.19: forward scattering $I(0)$, excluded volume parameter ν, and radius of gyration R_G.

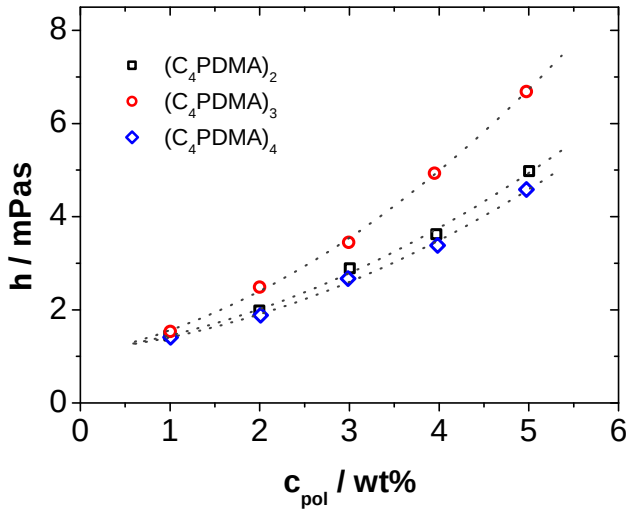

Figure 4.2: Zero shear viscosity of $(C_4PDMA)_2$ (squares, #2 in Table 2.2), $(C_4PDMA)_3$ (cicles,#3) and $(C_4PDMA)_4$ (diamonds, #5) in water as a function of the polymer concentration at a constant temperature of 25°C. The dotted lines are guides to the eye.

polymer concentration due to the osmotic pressure of the surrounding coils [94, 95]. From the forward scattering $I(0)$ it can be deduced that the scattering arises from polymer molecules that do not aggregate.

Figure 4.2 shows the zero shear viscosity of $(C_4PDMA)_2$, $(C_4PDMA)_3$ and $(C_4PDMA)_4$ in water as a function of the polymer concentration. The viscosity increases as a function of the polymer concentration. The viscosity increase is higher when the polymer has a higher molecular weight or size. The viscosity increases as a consequence of the increase in the polymer volume fraction, which is larger for polymers with larger molecular weight at a given concentration. This behavior does not depend on the polymer architecture and indicates that the polymers do not aggregate in water.

4.2 C12 end-capped linear and star polymers

4.2.1 SANS

In order to learn about the structure of the polymers in aqueous solution, SANS experiments were performed on 1 wt% and 5 wt% solutions of polymer samples with dodecyl stickers (entries #8, #13 and #17, see Table 2.2) in D_2O. The scattering curves, plotted in Fig. 4.3, show similar scattering patterns for the various polymers at a given concentration. Hence, the number of arms appears to have little impact on their supramolecular structure, at the length scales under investigation.

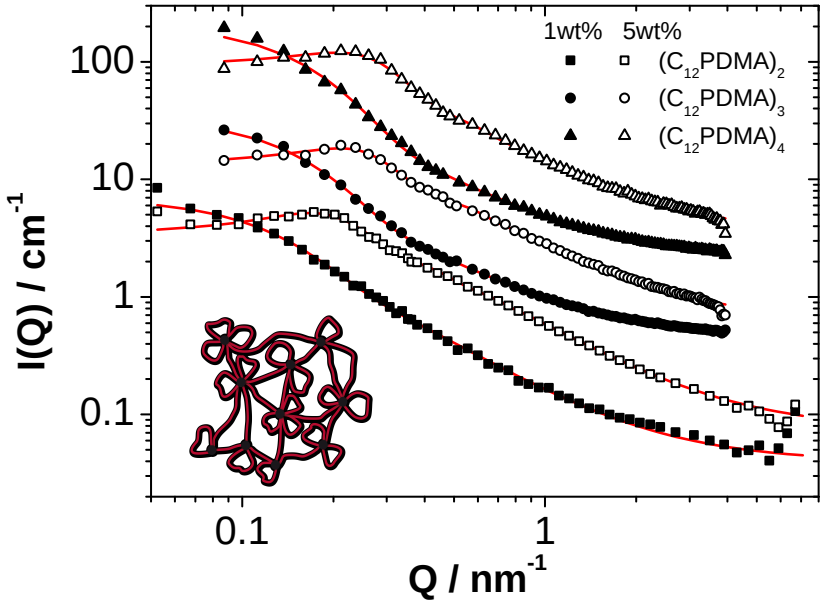

Figure 4.3: SANS patterns of the aggregates of $(C_{12}PDMA)_2$ (squares, #8 in Table 2.2), $(C_{12}PDMA)_3$ (circles, #13) and $(C_{12}PDMA)_4$ (triangles, #17) at concentrations of 1 and 5 wt% in D_2O at room temperature. The absolute intensity is correct for both $(C_{12}PDMA)_2$ curves, subsequent curves are multiplied by a factor 2n for better visibility. The lines correspond to the fitted curves with a star form factor and a hard sphere structure factor (Eq. 4.2). The first two curves ($(C_{12}PDMA)_2$) are from SANS2D and the rest from PAXY.

All samples exhibit scattering patterns as typically observed for spherically symmetric aggregates. In the case of the more concentrated solutions, the aggregates interact repulsively as indicated by a correlation peak. Most probably the hydrophilic polymer chains, which present a much larger volume fraction than the end groups in particular as the PDMA will be strongly hydrated, introduce significant repulsive interaction into this system. The attractive part of the interaction due to bridging is overwhelmed by an effective

repulsive interaction due to the numerous surrounding hydrophilic chains, which give rise to substantial steric hindrance. The mean spacing of the aggregates was calculated from the position of the peak (see Table 4.2). This distance may be compared to the radius of gyration R_G of a star polymer which can be calculated as [22]

$$\left\langle R_G^2 \right\rangle = \left(3 - \frac{2}{f}\right) \frac{C_\infty (N/f) b^2}{6} \tag{4.1}$$

where N is the total number of monomer units in the polymer, b is the length of the monomer, f is the number of arms in the star and C_∞ is a correction constant (accounting for the local stiffness of the polymer chain) that is 9.3 for PDMA in water [92]. The mean spacing of the aggregates decreases with the end-to-end distance of the polymer. Assuming a cubic packing of the aggregates (around the hydrophobic cores), we can obtain the number of the dodecyl chains per micelle (N_{St}) (see Table 4.2) and therefore the average number of polymer molecules associated with one micelle (N_{agg}) directly from the position of the correlation peak.

Assuming that the polymers self-assemble into flower-like micelles, like represented in the inset of Fig. 4.3, that interact with a spherically symmetric potential, the scattering intensity can be approximated as:

$$I(q) = nV^2 \Delta\rho^2 P(q) S(q) \tag{4.2}$$

where n is the number density of scatterers, V their volume, $\Delta\rho$ the difference between the coherent scattering length density of the micellar unit and the one of the solvent, P(q) the form factor, and S(q) the structure factor that takes into account the interactions between the aggregates. In order to describe the conformational structure of the aggregates we employed a form factor for a star proposed by Fetters et al. [21] which has been commonly used to describe the structure of flower-like micelles formed by telechelic polymers [13, 23, 100]:

$$nV^2 \Delta\rho^2 P_{Star}(q) = I(0) e^{(-q^2 R_G^2/3)} + \frac{\alpha}{q\xi} \Gamma(\mu) \frac{\sin(\mu \arctan(q\xi))}{(1 - q^2\xi^2)^{\mu/2}} \tag{4.3}$$

The first term of Eq. 4.3 is the Guinier approximation of the scattering intensity of the aggregates with radius of gyration R_G, and forward scattering $I(0)$ defined by the scattering of the dried volume of polymer given by $nV^2\Delta\rho^2$. The second term accounts for

the monomer–monomer correlations with α being the scale parameter, ξ the correlation length inside the star, and $\mu = 1/\nu - 1$ where ν is the excluded volume parameter and $\Gamma(\mu)$ is the gamma function of argument μ. To account for the repulsive interactions, a hard sphere structure factor, S(q,R_{HS},ϕ_{HS}) with the Percus–Yevick closure relation [68, 70] was employed, where R_{HS} is the effective hard sphere radius, that defines the interaction length, and the volume fraction (ϕ_{HS}) is determined by the number density ^1N of hydrophobic cores given by:

$$\phi_{HS} = nV = \frac{N_{AV} C_{wSt}}{M_{St} N_{St}} \frac{4}{3} \pi R_{HS}^3 \tag{4.4}$$

where N_{AV} is the Avogadro number and C_{wSt} , M_{St} , and N_{St} are the weight concentration, molecular weight and the aggregation number of the stickers, respectively. According to Eq. 4.4, the volume fraction ϕ_{HS} and the hard sphere radius R_{HS} are directly related to each other and enter only as one additional fit parameter which is the aggregation number N_{St}. One observes that R_{HS} (Table 4.2) is closely related to the length of the polymer.

Polymer	M_W (KDa)	R_G (nm)	c (wt%)	R_G (nm)	ξ (nm)	R_{HS} (nm)	ϕ_{HC} $\cdot 10^4$	$2\pi/q_{max}$ (nm)	N_{agg}	N_{St}
$(C_{12}PDMA)_2$ #8	121	12.5	1.0	12.8	8.3					
			5.0	8.6	3.7	13.8	1.84	26.5	10.4	20.6
$(C_{12}PDMA)_3$ #13	116	10.6	1.0	10.9	6.8					
			5.0	8.7	3.8	10.8	2.93	29.7	7.4	22.3
$(C_{12}PDMA)_3$ #17	118	9.8	1.0	10.3	7.5					
			5.0	6.44	2.9	10.3	3.8	33.5	5.3	21.0

Table 4.2: Structural parameters. Molecular weight by MALLS-SEC in water–acetonitrile M_W, radius of gyration calculated from Eq. 4.1, concentration of polymer in D_2O c, volume fraction of thedodecyl stickers ϕ_{HC}, aggregation number (per polymer molecule) N_{agg}, aggregation number of the stickers N_{St} (obtained from the position peak), radius of gyration R_G, correlation lengthinside the star ξ, and hard sphere radius R_{HS} (obtained from fits with Eq. 4.2).

At concentrations higher than the overlap concentration, the aggregation number is expected to increase as a consequence of the repulsion between the hydrophilic chains and at the same time the probability of bringing hydrophobic stickers together rises correspondingly [101]. It is interesting to note that N_{St} remains constant regardless of the number of arms of the polymer. The same result is obtained if with polymers of lower molecular weight [102]. This confirms that the free energy to form loops is irrelevant in the self-assembling process when the aggregation number is large enough as reported by Sèrèro et

al. [13]

Russel et al. [18] also reported that the aggregation number does not depend on the conformational energy of the polymer, i.e. the energy of loop formation. But the free energy of forming loops should different for polymers with different architectures and thus should have an impact on the micelle inteconection.

4.2.2 Dynamic light scattering

In order to obtain further insight into the structural and dynamical properties of these end-capped star polymers in aqueous solution, DLS measurements on 1 and 5 wt% solutions of the same samples (#8, 13 and 17) were done. The obtained intensity correlation functions $g^{(2)}(t)$ are shown in Fig. 4.4. The curves of samples with 1 wt% polymer exhibit an apparently rather simple decay, where the characteristic time is shifted to larger times with increasing number of arms. Nonetheless, the CONTIN analysis (see Fig. **??**) yields a rather complex distribution function of the decay times, where the maximum moves to larger times with the number of arms. Although this analysis must be taken with some care given the proximity of the maxima, it appears that there are 3 relaxation modes where the relative amplitudes change with the architecture of the polymer.

Additionally, a comparison of mono-exponential, a stretched exponential and a bi-exponential fit (see Fig. 4.5) shows that the correlation function results from the sum of at least two diffusive modes, as both show a q^2 dependence. Therefore, the curves were analyzed as a sum of two decaying exponential functions. The two effective diffusion coefficients (Table 4.3) correspond to the coexistence of small objects of 17 nm and of larger ones of around 200 nm. The fraction of larger aggregates increases with the number of arms (see Fig. 4.5). Also, the scattered intensity (listed in Table 3) increases with the number of arms supporting this idea. The hydrodynamic radii of the smaller-sized aggregates are in rather good agreement with the R g obtained by SANS (Table 4.2). The somewhat larger value for the hydrodynamic radius is presumably due to the slowing down of the diffusion process by the PDMA corona of these aggregates.

In the case of 5 wt% samples one observes an even much more complex relaxation behaviour that extends over more than 5 orders of magnitude in time. Such complex relaxation patterns are frequently observed for polymeric networks, but have also been seen for water-in-oil microemulsion droplets that are cross-linked by amphiphilic polymers.75

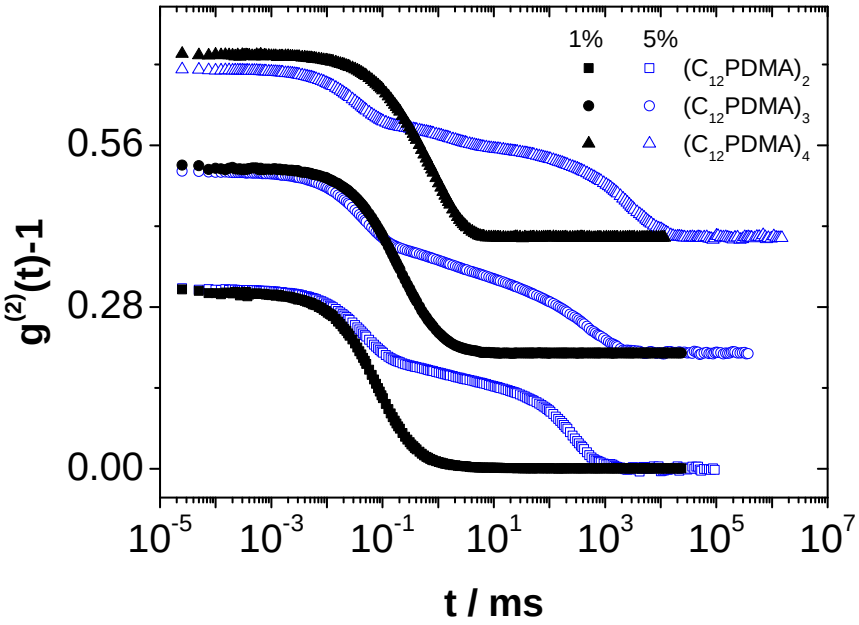

Figure 4.4: Intensity correlation function $g^{(2)}(t) - 1$ as a function of time for 1 and 5 wt% solutions of $(C_{12}PDMA)_2$ (#8), $(C_{12}PDMA)_3$ (#13) and $(C_{12}PDMA)_4$ (#17) in water at a scattering angle of 90degC and a temperature of 25 C (curves are correct for $(C_{12}PDMA)_2$ and shifted upwards by adding 0.2 or 0.4 to the corresponding curves).

In our case, the relaxation always proceeds via three clearly separated modes, as similarly observed before in the case of the classical associative telechelic $C_{12}-EO_{460}-C_{12}$ [15]. This demonstrates that one does not observe a simple diffusion process here, but the complex behaviour has to be associated with the network formed by the polymers in solution. Previous studies on model networks formed by simple telechelic polymers showed similarly three relaxation modes, where the fast one is associated with the droplet diffusion, the intermediate one is independent of q , and the slow one is typically also diffusive [103, 104].

For the 5 wt% samples the $g^{(2)}(t)$ data were fitted to a sum of one simple exponential and two stretched exponential functions:

$$|g^{(2)}(t) - 1| = \left[a_1 \cdot e^{-t/\tau_1} + a_2 \cdot e^{(-t/\tau_2)^{\beta_2}} + a_3 \cdot e^{(-t/\tau_3)^{\beta_3}}\right]^2 \tag{4.5}$$

From the angular dependence of the relaxation times (Fig. 4.6) we can conclude that the fast relaxation is purely diffusive as shown by its q^2 dependence. The effective collective diffusion coeficients are larger than what is expected from the size of the aggregates obtained by means of SANS. This is typical for repulsive interaction which enhances collec-

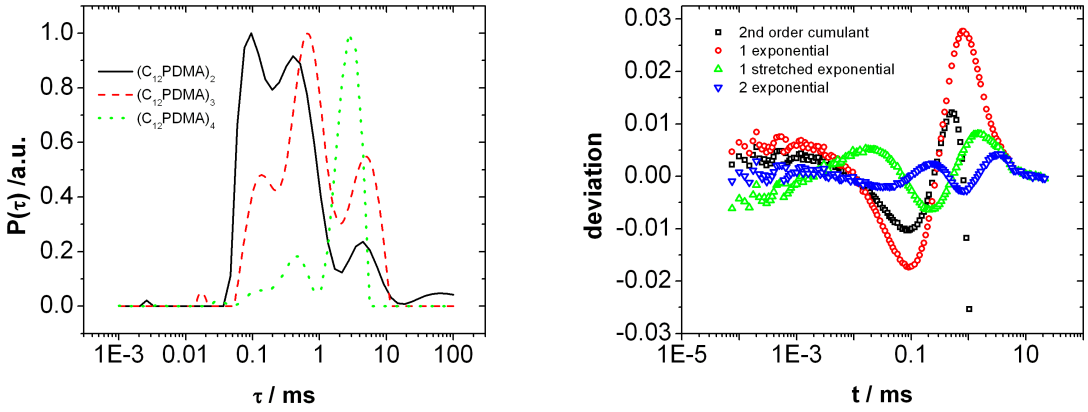

Figure 4.5: a) Distribition function of the decay times as obtained from CONTIN analysis of the autocorrelation functions of 1wt% solutions of $(C_{12}PDMA)_2$, $(C_{12}PDMA)_3$, $(C_{12}PDMA)_4$ in water.b) Residuals of the second order cumulant, mono-exponential decay, one stretched exponential decay and a bi-exponential decay fit.

Polymer	c (wt%)	a_{fast}	$10^{12}D_f$ (m^2s^{-1})	R_H (nm)	$10^{12}D_2$ (m^2s^{-1})	t_2 (ms)	r	t_R (ms)	G_0 (Pa)	$N_{St}(G_0)$
$(C_{12}PDMA)_2$	1.0	(0.7)	15.6	15.6	1.23		1.44			
7	5.0	0.26	53.8	4.5		1.3		9.1	72	0.32
$(C_{12}PDMA)_3$	1.0	(1.5)	13.8	17.6	2.1		4.63			
11	5.0	0.11	58.3	4.2		2.2		12	529	3.3
$(C_{12}PDMA)_3$	1.0	(5.4)	15	16.2	1.2		16.2			
14	5.0	0.05	71.5	3.4		1.8		16	2813	26

Table 4.3: Parameters obtained from DLS, SLS and rheology for $(C_{12}PDMA)_2$,$(C_{12}PDMA)_3$ and $(C_{12}PDMA)_4$ with concentrations of 1 and 5 wt%. Polymer concentration c, Diffusion coefficients D, relative amplitude of the fast diffusive mode for Eq. 4.5 a_{fast}, Rayleigh ratio R_θ, hydrodynamic radius R_H obtained from D_1, Relaxation time of the intermediate relaxation mode as obtained from Eq. 4.5, structural relaxation time τ_R, plateau elastic modulus G_0, aggregation number N_{St} obtained from G_0.

tive diffusion substantially compared to the non-interacting case [105]. The intermediate relaxation mode is almost independent of q , while the slow relaxation mode shows a rather strong dependency with the scattering vector, following a power law of 2–4, the exponent increasing substantially with increasing number of arms. Such behavior is characteristically observed for viscoelastic networks with physical cross-links [79, 106].

Interestingly, the slower modes become more prominent when going from the 2-arm to the 4-arm polymer. This indicates that the tendency for aggregation increases with the number of arms. In particular, the intermediate relaxation mode, which is independent of q , becomes more pronounced. This mode appears to be linked to the rheological properties

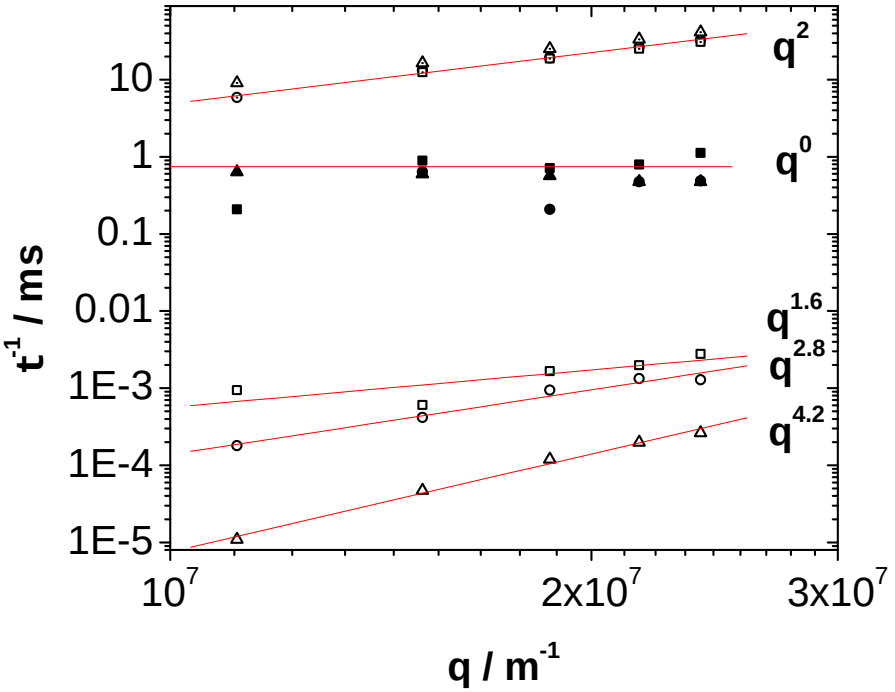

Figure 4.6: q dependency of the three relaxation times for 5 wt% solutions of $(C_{12}PDMA)_2$ (squares,#8), $(C_{12}PDMA)_3$ (circles, #13) and $(C_{12}PDMA)_4$ (triangles, #17).

of the samples (see Fig. 7) and its characteristic time appears to be directly related to the rheological relaxation time (τ_R). Thereby it would be a direct measure of the elastic properties of the formed networks.

4.2.3 Rheology

Figure 4.7 shows the zero shear viscosity of aqueous solutions of $(C_{12}PDMA)_2$,$(C_{12}PDMA)_3$ and $(C_{12}PDMA)_4$ as a function of the polymer concentration. We obtain a viscosity increase of several orders of magnitude by just a few weight percent polymer concentration, which is a typical behavior for such systems [11].

The increase in viscosity is considerably larger as the number of arms per polymer is increased, this can be explained by the formation of larger aggregates (clusters) by the polymers with more arms that leads to a higher effective volume fraction and thus to a viscosity increase.

At 5 wt%,a network is formed as already observed by SANS and DLS and the samples are highly viscous. In order to gain further information about their rheological behaviour the frequency dependent viscoelastic properties of these transient networks were deter-

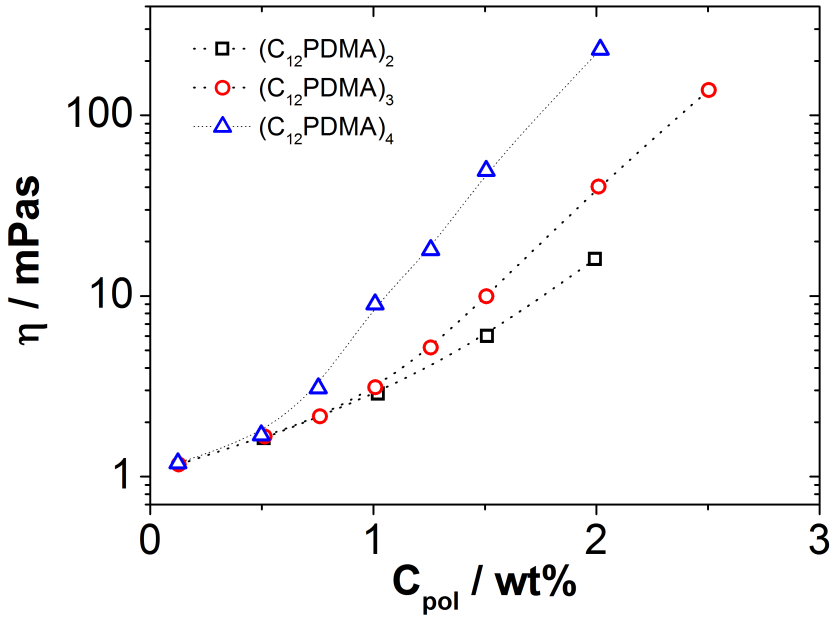

Figure 4.7: Zero shear viscosity for solutions of $(C_{12}PDMA)_2$ (squares,#8 in Table 2.2), $(C_{12}PDMA)_3$ (circles, #13) and $(C_{12}PDMA)_4$ (#17) in water as a function of the polymer concentration measured at 25°C. The dotted lines are guides to the eye.

mined by oscillatory shear experiments over an extended frequency range with a particular emphasis on the high frequency range. The obtained values for storage modulus G' and loss modulus G'' are given in Fig. 4.8. Both moduli are increasing for lower frequencies but not with the power law of 2 and 1, respectively, as predicted by the Maxwell model. Accordingly, these are not simple rheological systems but G' nonetheless effectively approaches a plateau value for frequencies above 100 Hz.

The crossover po int of G' and G'' can be taken for determining the characteristic rheological relaxation time, which increases from 9 to 16 ms when going from the 2-arm to the 4-arm polymer. This time is of the same order of magnitude as the q -independent intermediate relaxation process of DLS, thereby indicating that here the same process is monitored and they follow exactly the same tendency. At the same time, the plateau value of the elastic modulus G_0 increases from 79 to 2800 Pa. This shows that with increasing number of arms the relaxation process becomes slower and at the same time the elastic properties of the network increase substantially.

According to a simple network theory [107], the high frequency storage modulus is given by $G_0 = nk_BT$, where n is the number density of elastically connected points. This theory can be applied to the experimental data and from the number density n one can calculate

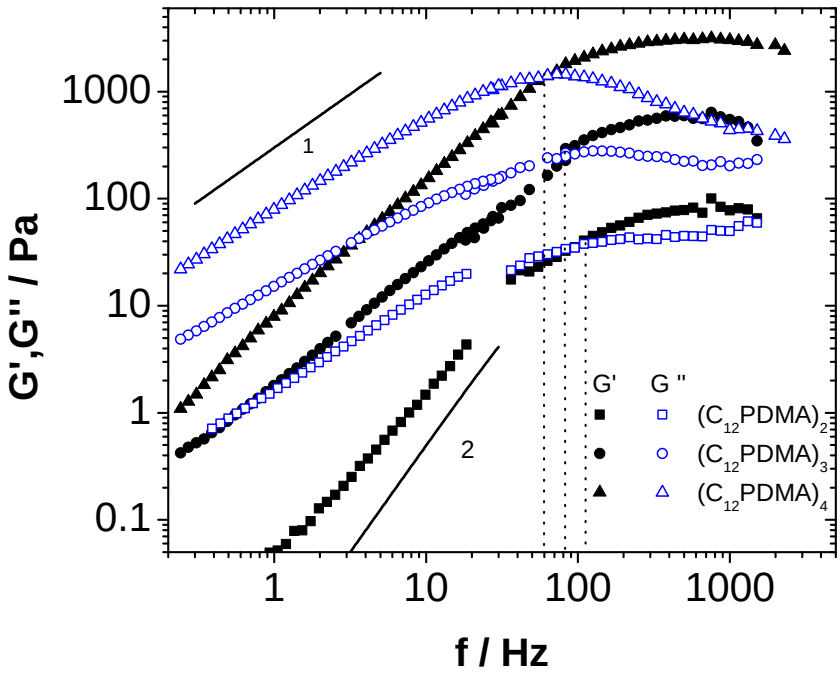

Figure 4.8: Storage modulus (G') and loss modulus (G'') as a function of the frequency (f) for 5 wt% solutions of 2C12 (121 kDa), 3C12 (116 kDa) and 4C12 (118 kDa) PDMA in water at room temperature. The solid lines indicate the respective power of 1 and 2 predicted by the Maxwell model. The dotted lines indicate the position of the cross-over frequency.

the corresponding theoretical number of elastic chains per aggregate (see Table 4.3).

Both DLS and rheology show that the polymers with more arms show a higher preference for interaggregate association than for intraaggregate association, i.e. for forming networks. In addition, the increase of the shear modulus G_0 apparently is directly related to the increase of the amplitude of the intermediate relaxation process observed in DLS which demonstrates that they are directly linked to each other and occur with the same characteristic time.

4.2.4 Conclusion

SANS studies of these highly water-soluble polymers revealed that their end-groups self-assemble in aqueous solution. While at lower concentrations flower-like micelles seem to exist, higher concentrations resulted in the formation of a transient network of polymer micelles. However, SANS did not show a peculiar effect of the number of arms of the star polymers on the structure of the networks, so that e.g. the number of hydrophobic dodecyl

chains is constant at about 20, irrespective of the number of arms. When looking into the dynamic properties of the networks using DLS and rheology, the number of arms and the tendency to form a network in between the micelles are correlated. DLS shows already a more complex behavior for dilute (1 wt%) samples, exhibiting a multi-modal relaxation, presumably due to the formation of clusters. The more concentrated (5 wt%) and highly viscous samples show even 3 relaxation modes. While the first is diffusive and related to the size of the contained hydrophobic domains, the characteristic time of the second mode is independent of q, and the relaxation rates of the third mode show a power law dependence on q that rises from 1.6 for the 2-arm polymer to 4.2 for the 4-arm polymer. The second mode shows a similar timescale as the characteristic time of rheology, and both methods agree well in the general trend of the values found. Our initial hypothesis that a branched amphiphilic polymer might show a higher tendency to form a network than a linear analogue is thus confirmed for their behaviour in aqueous solution. Importantly, this behaviour does not affect the static structure seen by SANS, but it affects in a similar way both DLS measurements and rheological behaviour. Future work will be directed towards the question whether such polymers are suitable for exerting rheological control in microemulsions as well.

Chapter 5

TDMAO/Decane/Rewopal 6000DS

The addition of telechelic polymers to oil in water microemulsions has been intensively studied with respect to the phase behavior [41, 44], structure [40, 43, 45], rheological and dynamical properties [42, 46, 108, 109], however studies where the relation between the microstructure and dynamics is addressed are rare [110].

Thus, in this chapter we present a complete study with SANS, rheology, DLS and FCS measurements of a model microemulsion with composition TDMAO 100mM / Decane 35mM / Water(D_2O) upon addition of a commercially available hydrophobically modified PEO polymer with structure C_{18}-EO_{150}-C_{18} (Rewopal 6000DS). This polymer is employed in many formulations as a rheological modifier. This study should serve as a reference for the further investigations with the telechelic star polymer, which possess a correspondingly more complex architecture.

5.1 Phase Behavior

The addition of Rewopal 6000DS up to 3.5wt% to the microemulsion consisting of TDMAO 100mM / Decane 35mM /Water (D_2O) resulted in homogeneous, transparent samples with increasing viscosity. No yield stress was observed. For a polymer concentration higher that 3.5wt%, the samples became turbid while still viscous, but no phase separation occured, even after centrifugation.

The phase behavior and the mixture properties depend strongly on the ratio between the end-to-end distance of the polymer and the distance between the droplets [41, 52]. The end-to-end distance of the PEG chain of the polymer C_{18}-EO_{150}-C_{18} was calculated

according to the Flory-Huggins-theory $R_{ee} = \sqrt{4Nl_{EO}}$ (l_{EO}=3.75 Å) [65, 92]. The value of R_{ee} is 9.2 nm. Assuming a cubic arrangement of the oil droplets, the distance between the droplets' centers is 13.6 nm and the distance between the droplets' surfaces is 8.20 nm. Therefore, the end-to-end distance of the hydrofilic chain of the polymer is considerably smaller the distance between the droplets.

5.2 SANS

To understand how the microstructure of the microemulsion/HM-polymer mixtures affects the dynamic and rheological properties, a comprehensive study of the structure is needed. For this reason, SANS measurements were performed for samples with microemulsions (TDMAO 100mM/Decane 35mM/D2O) and telechelic polymer added.

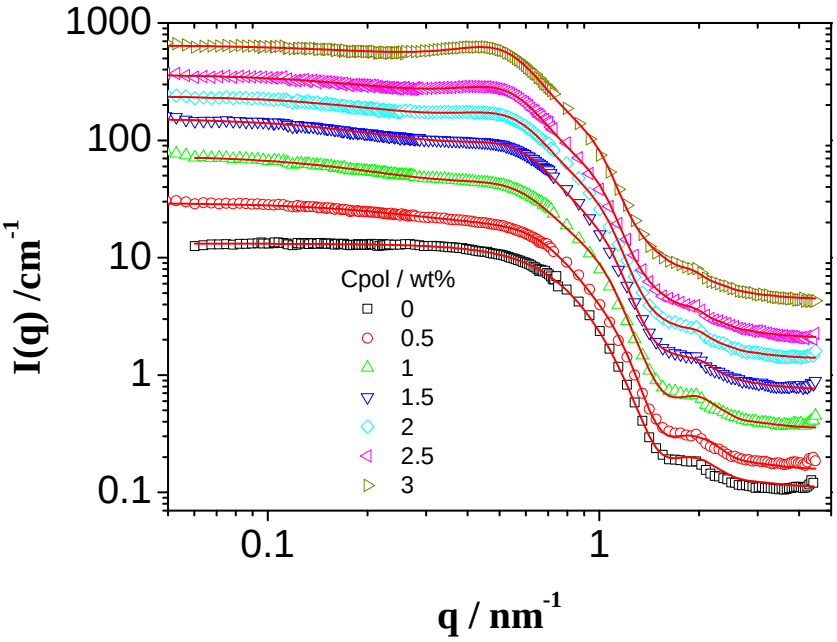

Figure 5.1: Scattering intensity patterns of the aggregates of microemulsion(squares) and with polymer concentrations between 0 and 3 wt% at temperature of 25°C on the instrument KWS2 (Garching, Munich). The curves are shifted by a factor 2^n

Figure 5.1 shows the scattering intensity against the magnitude of the wave vector q of the microemulsion with Rewopal 6000DS concentrations between 0 and 3wt%. At first look, the unchanged position of the minimum at high q is the sign that the average size of

the droplets is not influenced by the polymer. The upturn of the intensity at low q by the addition of small amounts of polymer indicates the presence of large objects, which likely are linked microemulsion clusters and/or attractive interactions. This indicates that the addition of hydrophobically modified polymer induces an effective attractive interaction between the oil droplets. With increasing polymer content, a correlation peak appears suggesting an effective repulsive interaction. The fact that the position of the peak remains constant inferes that there is a preferred distance between the droplets, which is simply given by their constant number density as the droplet size does not change.

In order to obtain more detailed information about the structure, a model analysis of the data was performed. Assuming that the scattering mainly arises from the microemulsion, the scattered intensity can be expressed as follows:

$$I(q) = n_s V_s \Delta\rho^2 P(q) S(q) \tag{5.1}$$

n_s is the particle density, V_s is the volume and $\Delta\rho$ is the scattering length density contrast. P(q) is the form factor accounting for the shape and size of droplets and S(q) is the structure factor accounting for interactions between the droplets and I_{inc} accounts for the incoherent scattering. The decoupling of P(q) and S(q) is strictly only valid for monodisperse systems, but commonly employed as well for polydisperse systems [111].

For $P(q)$ the model of an homogeneous sphere was employed with the spherical particles having a log-normal size distribution of radii. The scattering length density contrast is calculated as the difference between the scattering length density of the aggregates and the average scattering length density of the sample (More information can be found in Section 2.1).

The attractive potential was modeled with Baxter´s model [71], which corresponds to the sticky hard-sphere limit where the attraction range becomes infinitesimally small while the attraction strength becomes infinite in such a way that the second virial coefficient B_2 remains finite. The interaction potential for a Sticky Hard Sphere (SHS) model is described

by the following expression:

$$\frac{U(r)}{k_B T} = \begin{cases} \infty & \text{for} \quad 0 < r < 2R_{HS} \\ \ln \frac{12\tau\Delta}{2R_{HS}+\Delta} & \text{for} \quad 2R_{HS} < r < 2R_{HS} + \Delta \\ 0 & \text{for} \quad r > 2R_{HS} + \Delta \end{cases} \tag{5.2}$$

Here k_B is the Boltzmann constant, T the absolute temperature, R_{HS} is the hard sphere radius and Δ is the width of the attractive well. In the SHS model, when applied, the limit $\Delta \to 0$ is taken. Thus, only a single parameter, the stickiness parameter τ, characterizes the adhesive strength. The significance of τ is the dimensionless temperature, and its inverse, τ^{-1} , is a measure of the stickiness of the particles. The case $\tau^{-1} = 0$ corresponds to hard spheres. This model is theoretically convenient because it has an analytic solution within the Percus–Yevick closure [68] and, consequently, it has been often used in comparison to experiments [112]

C_{pol} /wt %	$I_{inc}{}^*/\ cm^{-1}$	$\Delta\rho$ /nm-4	ϕ	σ^*	R */nm	$R_{HS}{}^*$ /nm	$\phi_{HS}{}^*$	τ^*
0	0.099	6.43	3.30	0.14	2.71	4.11	0.04	∞
0.25	0.087	6.42	3.29	0.14	2.71	5.06	0.06	0.35
0.5	0.077	6.40	3.28	0.14	2.71	5.74	0.06	0.25
0.75	0.093	6.39	3.28	0.14	2.71	6.37	0.05	0.20
1	0.087	6.37	3.27	0.14	2.71	6.67	0.05	0.17
1.25	0.090	6.36	3.26	0.14	2.71	6.59	0.05	0.19
1.5	0.093	6.34	3.25	0.17	2.74	6.43	0.08	0.22
1.75	0.096	6.33	3.24	0.18	2.72	6.48	0.09	0.24
2	0.114	6.31	3.23	0.18	2.77	6.60	0.10	0.25
2.25	0.099	6.30	3.23	0.19	2.75	6.60	0.11	0.27
2.5	0.103	6.29	3.22	0.19	2.77	6.75	0.12	0.27
2.75	0.108	6.27	3.21	0.20	2.75	6.81	0.14	0.30
3	0.110	6.26	3.20	0.20	2.80	6.83	0.15	0.32

Table 5.1: Structural parameters. Droplet volume fraction ϕ, scattering length density contrast $\Delta\rho$ and parameters (*) obtained from fitting the SANS curves with Eq. 6.2: incoherent background I_{inc}, radius of the droplets R, standard deviation of the Log-Norm distribution σ, hard sphere radius R_{HS}, hard sphere volume fraction ϕ_{HS} and the stickiness parameter τ.

The results of the fits with our model are listed in Table 5.1. The fitted curves (see Fig. 5.1) describe very well the experimental data. Hence, our model seems to describe accurately the structure of the samples

Quantitative analysis of the scattering data based on Eq. 6.2 permits us to extract the mean radius of the spherical droplets are equal to 2.7 nm with a standard deviation of 0.14.

This results are in very good agreement with the ones previously reported for the same system [57]. Although, the standard deviation is somewhat higher because it includes the experimental smearing that was not taken into account in the model.

One would expect that the radius of the droplets decreases when polymers are anchored to the surface. The addition of end-modified polymer means an additional number of chains in the interface, which also have a more voluminous polar part, both facts contribute to a decrease of the droplet radius. Theoretical models developed for membranes decorated with small amounts of anchored polymers predict a radius decrease [113]. However, this predictions are for coiled chains, and telechelic polymers anchored to oil droplets as loops or bridges are rather stretched. Additionally, the grafting density is too low to affect the curvature of the microemulsion interface. Previous SANS studies in analogous systems [40, 43, 45] also showed that the droplet size does not change with the presence of HM-polymer.

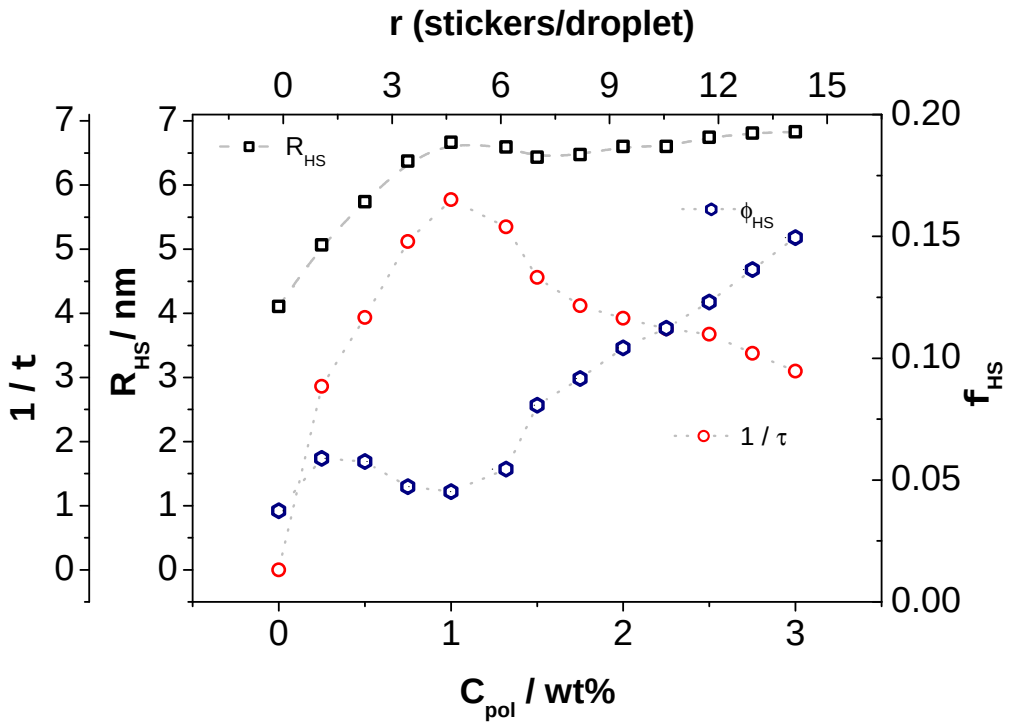

Figure 5.2: Parameters of the sticky hard sphere structure factor: Hard sphere radius R_{HS} and stickiness $1/\tau$ as a function of the polymer concentration obtained by fits of SANS data (Eq. 6.2)

The stickiness, represented by $1/\tau$, first increases with the polymer content until it reaches a maximum at a polymer concentration of 1wt%. For higher polymer concentration,

the stickiness deccrases monoticallly. For higher polymer content of more than 4 stickers per droplet the repulsive interaction becomes more pronounced again, which arises from the volume requirements of the hydrophilic chains. This can also be seen nicely in Fig. 5.2, which depicts the increase of the effective hard sphere volume fraction as a function of the polymer concentration.

The attractive component of the interaction can be understood as the gain in entropy due to the possibility of the chains to form a bridge momentarily. This would mean that during this time two droplets come closer to another in a lower volume fraction. After percolation, the net interaction is repulsive because they resist interpenetration.

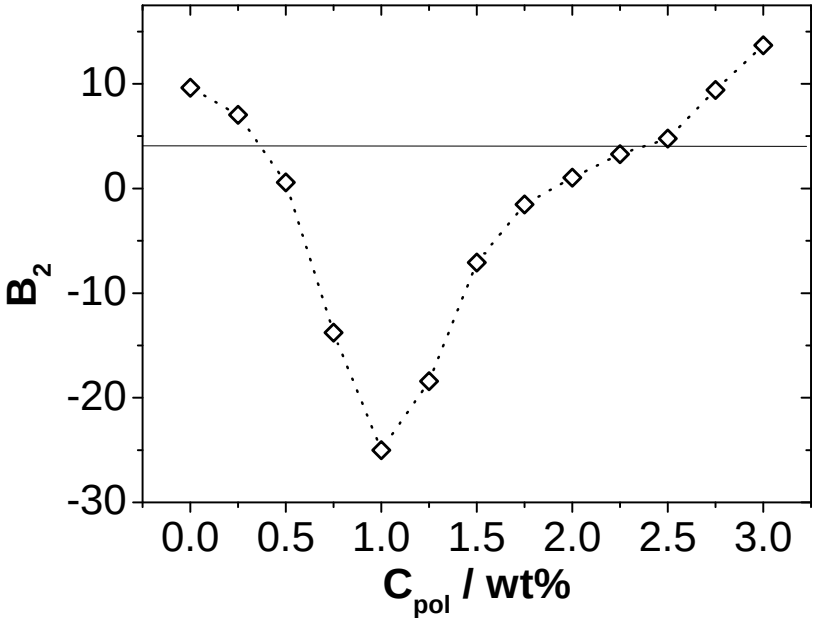

Figure 5.3: Dimensionless second virial coefficient as a function of the added polymer concentration calculated with Eq. 5.3 with the structural parameters obtained from the SANS data. Line: $B_2 = 4$

Another way of describing the droplet interactions is given by the dimensionless second virial coefficient $B_2 = \frac{2\pi}{V}\int_0^\infty (1 - exp(-U(r)/k_BT))r^2dr$ that is independent of the form of the potential [114]. The dimensionless second virial coefficient for a sticky hard sphere potential is defined as

$$B_2 = \frac{1}{V_{droplets}}\left\{\frac{2\pi\sigma_{HS}^3}{3} - \frac{1}{\tau}\frac{\pi\sigma_{HS}^3}{6}\right\} \tag{5.3}$$

where σ_{HS} is the hard sphere diameter, τ the stickiness parameter and $V_{droplets}$ the

volume of the droplets ($V = 4\pi R^3/3$), the radius of the droplets R being 2.71 nm. We calculated B_2 with the parameters obtained from the SANS fits (see Table 5.1) and the results are plotted in Figure 5.3. From the definition of B_2, the excluded volume contribution (neglecting a hydration shell) is represented by $B_2 = 4$. If $B_2 < 4$ the interaction is attractive and if $B_4 > 4$ the interaction is repulsive.

The pure microemulsion has a value of $B_2 > 4$. The addition of polymer results in an increase in the attraction reflected in a big decrease on the value of B_2 until a concentration of polymer of 1wt%, when the value of B_2 starts to increase again. From a concentration of 2.5 %, the nett interaction is repulsive.

5.3 Rheology

In order to characterize the macroscopic properties of the system, rheology measurements were performed. Above a the percolation concentration, the samples exhibit viscoelastic behavior.

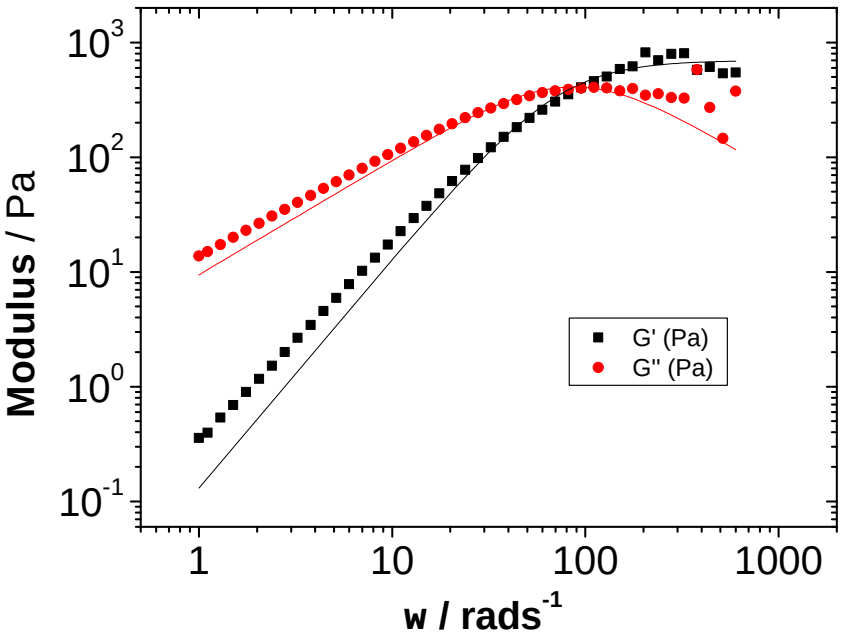

Figure 5.4: Storage (G') and loss (G'') moduli as a function of the frequency (ω) for microemulsion with 3,38wt% of C_{18}-EO_{150}-C_{18} measured with the instrument AR-G2 at a constant temperature of 25°C

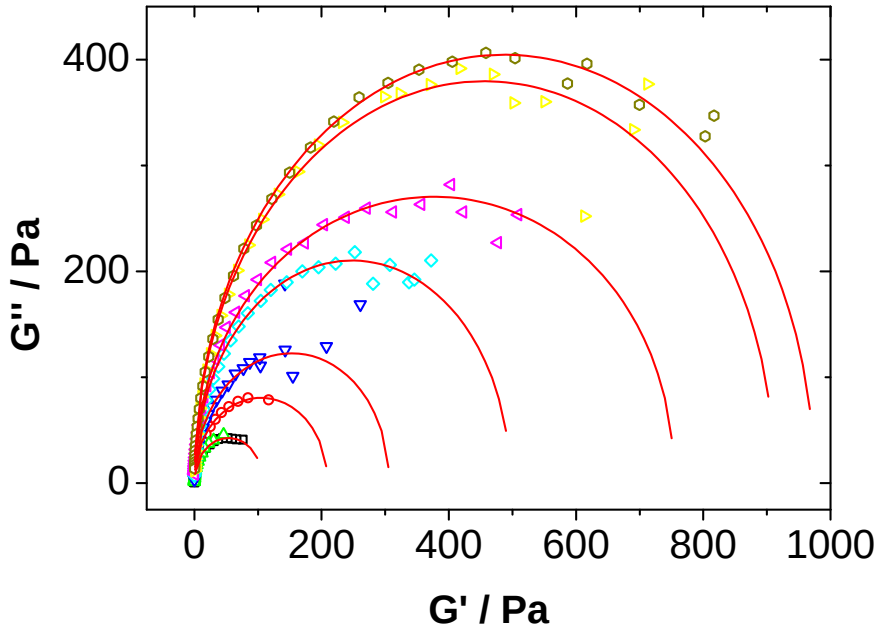

Figure 5.5: Cole-Cole representation of the loss modulus G' as a function of the storage modulus G'' for mixtures of microemulsion consisting of TDMAO 100mM / Decane 35mM / water with different quantities of C_{18}-EO_{150}-C_{18} added. Measured with the instrument AR G2. The lines represent the fits with Equation 5.4

As an example, the viscoelastic response to an applied oscillatory deformation of the microemulsion with 3.38 wt% added is shown in Figure 5.4. At low frequencies, the viscous modulus is higher than the elastic modulus and the sample behaves as a viscous liquid. At high frequencies, the samples behaves elastically. The crossover frequency or alternatively, the crossover time, corresponds to the structural relaxation time. In the case shown here, we arrived at a rheological relaxation time of 0.011 s. The data was fitted to the equations of the Maxwell model for linear viscoelasticity, described by equations 2.59 and 2.60. We observe that the model describes well the data with small deviations. Therefore, the structural relaxation may be described by one relaxation process.

Alternatively, the data can be represented as the Cole-Cole representation of the storage modulus G' against the loss modulus G''. For the Maxwell model, it will be described by

$$G''(\omega) = [G'(\omega)G_0 - G'(\omega)^2]^m \tag{5.4}$$

with $m = 0.5$, i.e, the equation of a circle, and G_0 the plateau modulus. The best fits

were obtained for a value of $m = 0.482$, thereby indicating almost perfect Maxwellian behavior. The plateau modulus values obtained by fitting with Eq. 5.4 are listed in Table 5.2. Additionally, The relaxation time may be obtained from the maximum of the curve, which is the point at which G' is equal to G''. The plateau value modulus increases with the concentration of C_{18}-EO_{150}-C_{18} added in a monotonic manner. This is due to the fact that there are more bridges.

The concentration dependence of the plateau modulus G_0 is depicted in Figure 5.6. Previous works on microemulsion networks have shown that the transition from the fluid

C_{pol} / wt%	r	G_0 / Pa	τ_R / ms	$G_0/\nu k_B T$
1.72	8.08	103	104.9	0.017
1.96	9.04	170	56.6	0.025
2.18	10.06	209	52.1	0.028
2.45	11.29	306	56.6	0.037
2.67	12.33	496	64.7	0.054
2.90	13.40	754	56.6	0.076
3.14	14.50	912	64.7	0.085
3.38	15.62	974	64.7	0.084

Table 5.2: Rhological parameters for microemulsions with C_{18}-EO_{150}-C_{18}. Polymer concentration c, number of stickers per droplet r, and parameters derived from the fit using Eq. 5.4 of the Cole-Cole representation: high frequency modulus G_0, relaxation time τ_R and reduced modulus $G_0/\nu k_B T$.

low-viscous phase to the viscoelastic phase occurs at the percolation concentration [44,110, 115]. The percolation theory predicts that the zero shear viscosity and the high frequency modulus are described by the following equations [116]

$$\eta \propto (c_p - c)^{-k} \tag{5.5}$$

$$G_0 = G_{00}(r - r_c)^t \tag{5.6}$$

where c_p is the percolation concentration and the exponents have values of $k \approx 0.7$ and $t = 1.7$. We fitted the experimental data of G_0 with Equation 5.6. We fixed the value of t to 1.7 and the best fit was obtained for a percolation concentration of 1.32 wt% (see Fig. 5.6), which corresponds to 6.1 stickers per droplet. This is considerabbly higher than the value of 0.6 predicted by the Flory-Stockmayer theory, on a Bethe lattice for a random bond percolation [116]. The reason for this, is because not all the polymer chains are

forming a network link. According to a simple network theory [107], the high frequency storage modulus is given by $G_0 = \nu k_B T$, where ν is the number density of elastically connected points. The reduced high modulus, calculated by deviding by the number of polymer chains, (see Table 5.2) is much lower than 1, meaning that not all the polymer chains are elastically active. This is mainly due to the loop formation [110] but there may also be constribution of network failures [34].

The fraction of loops is higher than the bridge fraction because the end-to-end distance of the polymer is smaller than the distance between the droplets. The formation of bridges is still possible if the EO chain stretches. The contour length of the EO chain is 56.3 nm, which corresponds to the completely stretched chain. Nevertheless, it is energetically not so favorable.

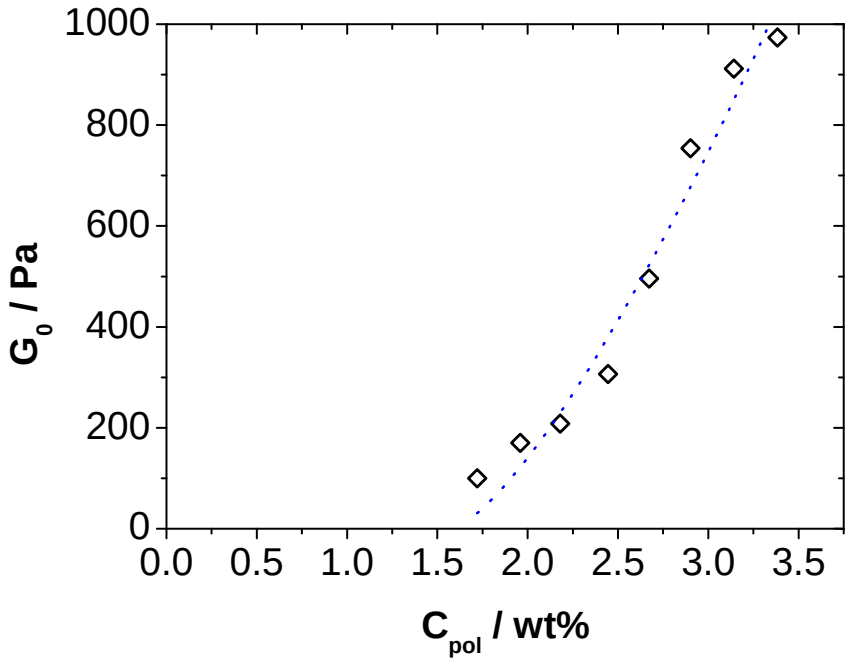

Figure 5.6: High frequency modulus of microemulsions-HM polymer mixtures as a function of the concentration of C_{18}-EO_{150}-C_{18} measured with the instrument AR-G2 at a constant temperature of 25°C. Dotted line: $G_0 = 307(c - 1.32)^{1.7}$

The relaxation time remains constant with the polymer concentration (see Table 5.2). This is not surprising because the relaxation time is related to the lifetime of a bond in the network. In this case, the process of breaking and reforming a link is controlled by the residence time of the sticker in the oil droplet.

The zero shear viscosity is related to the high frequency modulus via $\eta_0 = G_0 \tau_R$. Since

the relaxation time is constant with the concentration, the viscosity dependence with the concentration is dominated by the contribution of G_0.

Figure 5.7 shows the zero shear viscosity for microemulsions-HM polymer mixtures as a function of the concentration of C_{18}-EO_{150}-C_{18}. The viscosity increases with increasing polymer concentration. The increase can be divided into to three regimes. At low polymer concentration, the viscosity increases what appears to be quadratically with the concentration. In the second regime, at intermediate polymer concentration the rise is more pronounced. In the third regime the increase follows a power law with the concentration and the samples have a viscoelastic behavior.

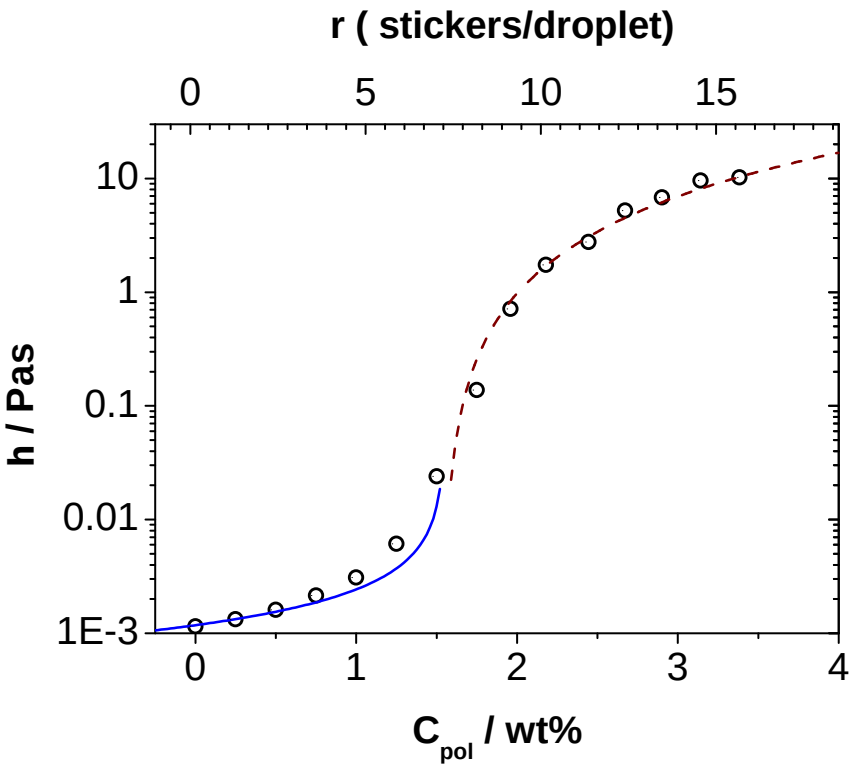

Figure 5.7: Zero shear viscosity of microemulsions-HM polymer mixtures as a function of the concentration of C_{18}-EO_{150}-C_{18} measured with with a capillary viscosity until a concentration of 2wt% and with the instrument AR-G2 above this concentration at a constant temperature of 25°C. Solid line: $\eta_0 = 0.0016(1.54 - c)^{-0.7}$. Dashed line: $\eta_0 = 3.6(c - 1.54)^{1.7}$

In the low concentration regime the viscosity increases due to the increase of effective volume fraction due to the formation of loops decorating the droplets. The viscosity can

be expressed as

$$\eta_r = 1 + \frac{5}{2}\phi_{eff} + O(\phi_{eff}^2) \tag{5.7}$$

However, the dependence of the effective volume fraction ϕ_{eff} is not trivial. As an alternative, one could also describe the viscosity increase with a percolation expression as $\eta \propto (c_p - c)^{-k}$ below the percolation concentration c_p and $\eta \propto (c - c_p)^{\gamma}$ above the percolation concentration.

The percolation equations are able to describe the viscosity at low concentrations and at high concentrations very well (see Fig. 5.7), yielding a percolation concentration of 1.54wt% or, equivantely, 7.1 stickkers or 3.5 polymers per droplet. This value is in very good agreement with the one obtained by fitting the high frequency modulus.

Here, it should be said that the percolation theory considers permanent bonds and this is not the case in the microemulsion/ HM-polymer networks, where the lifetime of a bond is given by the residence time of the sticker in the oil droplets. Nevertheless, the high frequency modulus is measured at times shorter than the relaxation time and the bonds can be considered as permanent.

5.4 Dynamic light scattering

To further investigate the dynamic properties of the system, we performed dynamic light scattering experiments on the polymer/microemulsion mixtures. Figure 5.8 shows the intensity correlation function $g^2(t)$ for a scattering angle $\theta = 90°$ and for various concentrations of C_{18}-EO_{150}-C_{18} added to the microemulsion. The curve of the microemulsion exhibits a monoexponential decay arising from the Brownian motion of the oil droplets in water. Upon addition of polymer the relaxation becomes slower and the correlation function starts deviating from monoexponential behavior. A second relaxation mode appears and its amplitude and characteristic time increase with increasing concentration of polymer.

In order to identify first the number of relaxation modes, the size distributions were obtained by inverse Laplace transformation using CONTIN analysis [77]. The evolution of these distributions are presented in figure 5.9. The decay time distribution of the pure microemulsion is monomodal. When adding polymer there are 3 concentration regimes. First, below 1.25 wt% the distribution is bimodal, then a third mode becomes visible. The

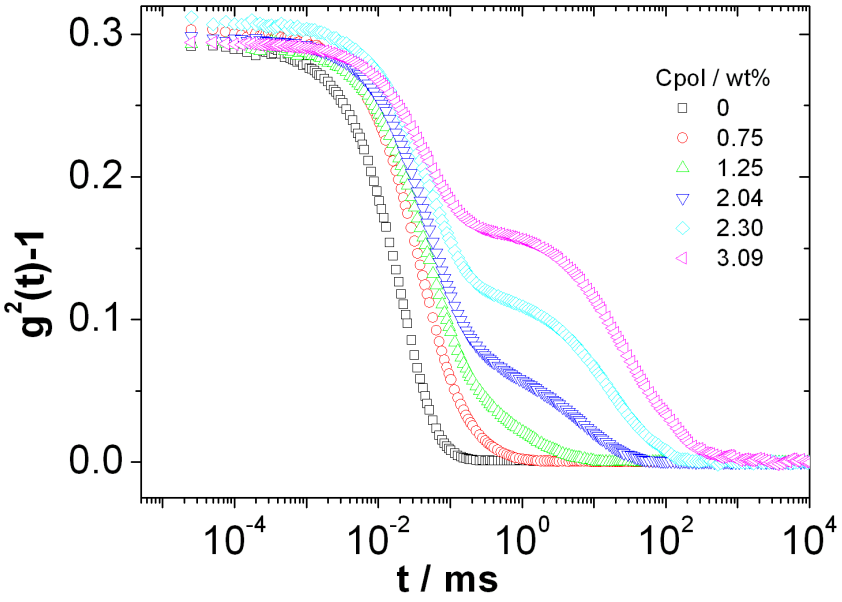

Figure 5.8: Intensity correlation function of microemulsions with several concentrations of C_{18}-EO_{150}-C_{18} added measured at a scattering angle of $\theta = 90°$ and a temperature of 25°.

slowest mode then becomes for further increasing polymer concentration more prominent and moves to longer times, while the intermediate mode almost vanishes.

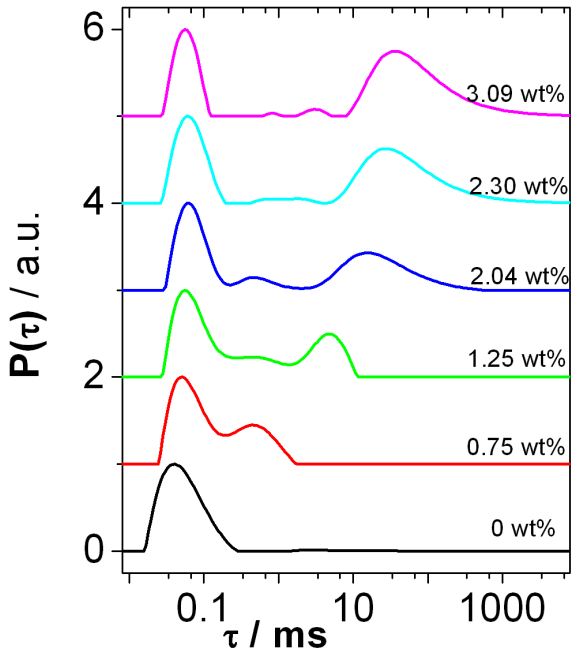

Figure 5.9: Intensity weighted decay time distributions of microemulsion with C_{18}-EO_{150}-C_{18} determined by dynamic light scattering for a polymer concentration of 0, 0.75, 1.25, 2.04, 2.30 and 3.09 wt%

However, the results obtained by CONTIN must be treated with caution when the distributions are too closely spaced. Thus, once identified the number of modes that appeared in each regime, it makes more sense to analyze the results in terms of a sum of normal or stretched exponential decays of $g^1(t)$, where the amplitudes a_i and parameters β_i may provide useful information. Thus, the curves were fitted to the following expression:

$$|g^{(2)}(t) - 1| = \left[a_{fast} \cdot e^{-t/\tau_{fast}} + a_{slow} \cdot e^{(-t/\tau_{slow})^{\beta_{slow}}} \right]^2 \tag{5.8}$$

The fast relaxation time τ_{fast} was in all cases diffusive since it exhibits a q^2 dependence. Thus, the fast relaxation mode is due to the diffusion of the oil droplets, as it has been found in previous investigations [42, 110].

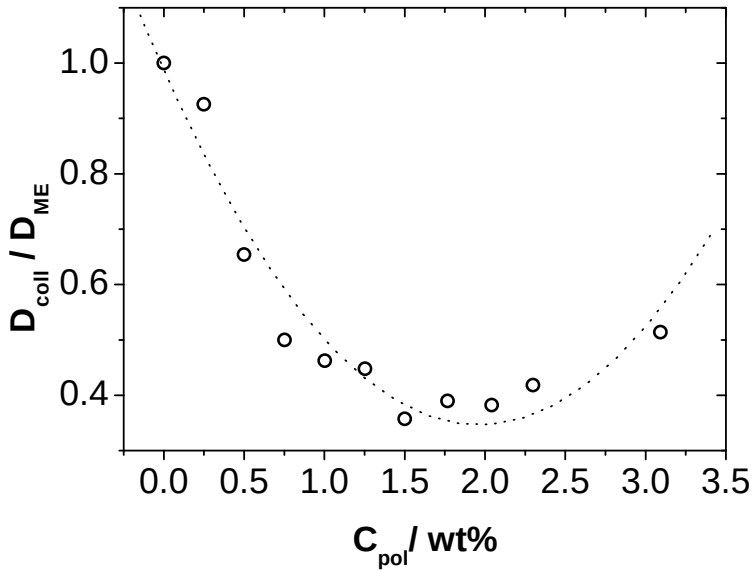

Figure 5.10: Reduced collective diffusion coefficient D_{coll}/D_{ME} calculated as $D_{coll} = 1/(\tau_{fast}q^2)$. D_{ME} is the diffusion coefficient of the microemulsion without polymer. The dotted line is a guide to the eye

The collective diffusion coefficient is related to the fast relaxation time through $1/\tau_{fast} = D_{coll}q^2$. The normalized diffusion coefficient as a function of the concentration of C_{18}-EO_{150}-C_{18} is represented in Figure 5.10. As the polymer is added, the attractive interactions slow down the diffusion. This is consistent with our structural picture that showed a large increase of the attractive interaction upon addition of the polymer, which is in agreement with a corresponding slowed down diffusion. The maximum of the virial coefficient B_2 in

Figure 5.3 coincides roughly with the minimum of D_{coll} in Figure 5.10.

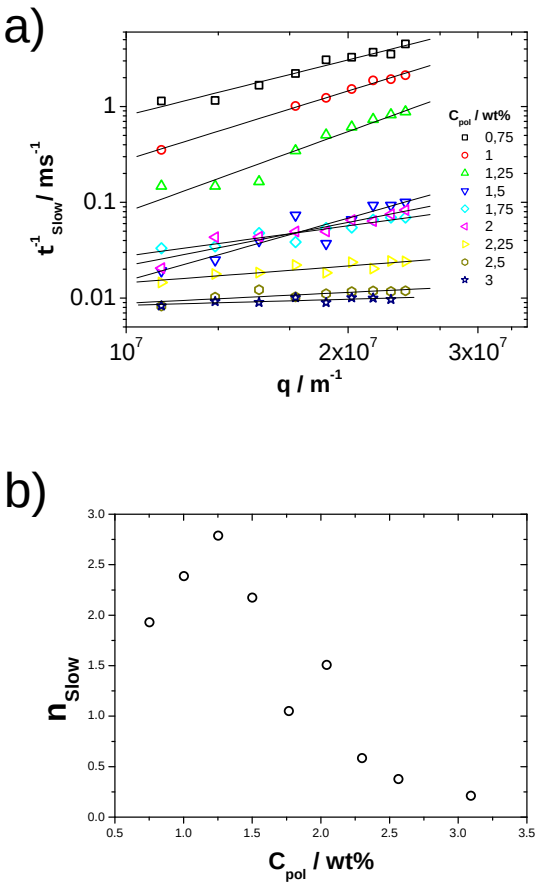

Figure 5.11: a) Slow relaxation time inverse τ_{slow}^{-1} as a function of the magnitude of the scattering vector q. Solid lines: fits with equation $\tau_{slow}^{-1} \sim q^{n_{slow}}$. b) q-dependance exponent n_{slow} as a function of the polymer concentration added to microemulsion.

Figure 5.11 shows the q dependence of the slow relaxation mode. The curves were fitted to the expression $\tau_{slow}^{-1} \sim q^{n_{slow}}$. At low polymer content, the q dependence is around 2, indicating a diffusive mode. By increasing the polymer concentration, n_{slow} until almost zero at a polymer concentration of 3.3 wt%.

The second relaxation mode appears in microemulsion networks and it is not always diffusive. In the cases of a nondiffusive second mode [**?**, 103, 108] it was shown for that the relaxation time was strongly correlated with the terminal relaxation time of an oscillatory shear experiment and was thus interpreted as the average lifetime of the network junctions. In our case the relaxation time of the second relaxation mode τ_{slow} increases with the polymer concentration. When the exponent n_{slow} tends to zero, the relaxation time is about 100 ms, which is very near to the values obtained for the structural relaxation time

(see Table 5.2).

5.5 FCS

In order to gain a further understanding of the dynamic properties of the system, fluorescence correlation spectroscopy measurements were performed. As a probe molecule we chose a hydrophobic dye (Nile Red) that is solubilized in the oil droplets, assuming a negligible solubility of the dye in water. With this method we can determine the self diffusion coefficient D_{self} of the droplets. Figure 5.12 shows the correlation functions for the studied microemulsion with increasing concentrations of C_{18}-EO_{150}-C_{18}.

The curves exhibit a single decay that may be described by Eq. 2.47. The decay times,

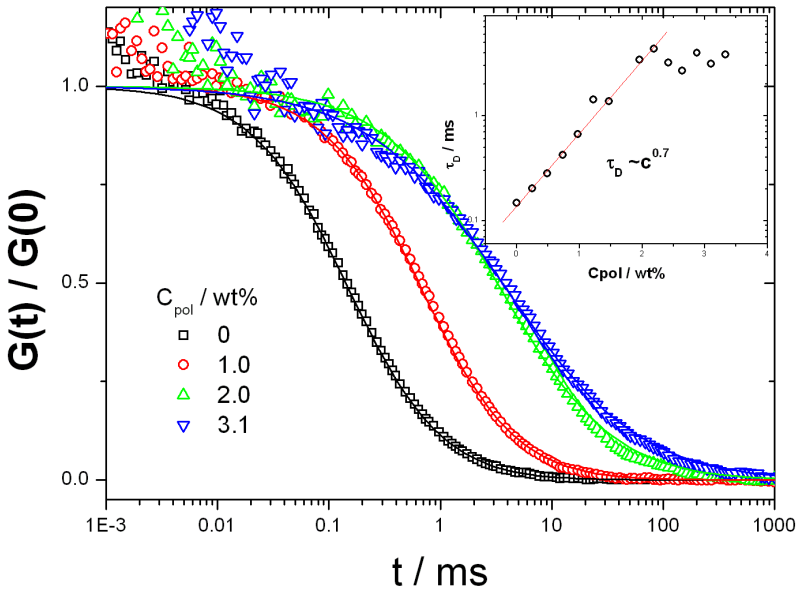

Figure 5.12: Normalized autocorrelation function of microemulsion with C_{18}-EO_{150}-C_{18} of different concentrations. The lines are the fits with Eq. 2.47 yielding the parameters listed in table 5.3. The inset plots the relaxation time as a function of the polymer concentration

listed in Table 5.3, increase monotonically with the polymer concentration until a concentration of 2wt%. After this concentration, the time remains constant but the anomalous diffusion, characterized by the stretched parameter γ being smaller than 1, becomes larger.

The inset of Figure 5.12 shows the concentration dependence of the relaxation time. The time follows a power law of $\tau_D \sim c^{0.7}$. The relaxation time starts to be constant at a

C_{pol}/wt%	τ_D/ms	α
0	0.15	0.99
0.25	0.20	0.94
0.49	0.28	0.99
0.74	0.42	0.97
0.99	0.67	0.98
1.22	1.44	0.96
1.47	1.38	0.88
1.96	3.41	0.83
2.18	4.34	0.80
2.41	3.20	0.74
2.64	2.69	0.74
2.87	3.98	0.80
3.33	3.81	0.70
3.10	3.12	0.64

Table 5.3: FCS fit parameters for microemulsion/ HM-polymer obtained by fitting the FSC autocorrelation functions with Eq. 2.47. Diffusion time τ_D and anomalous diffusion exponent α.

concentration of 2wt%.

The anomalous diffusion exponent α as a function of the polymer concentration is plotted in Figure 5.14. A low polymer concentration the exponent is almost 1, so the diffusion of the droplets is simple. At a concentration higher that 1wt% the exponent α starts to decrase with the polymer concentration. Interestingly, this concentrations coincides with the concentration at which repulsive interactions du to network formation start to appear, as shown by a minumum in the second virial coefficient B_2 obtained by SANS (see Fig. 5.3) and a minumum in the collective diffusion coefficient obtained by DLS (see Fig 5.10).

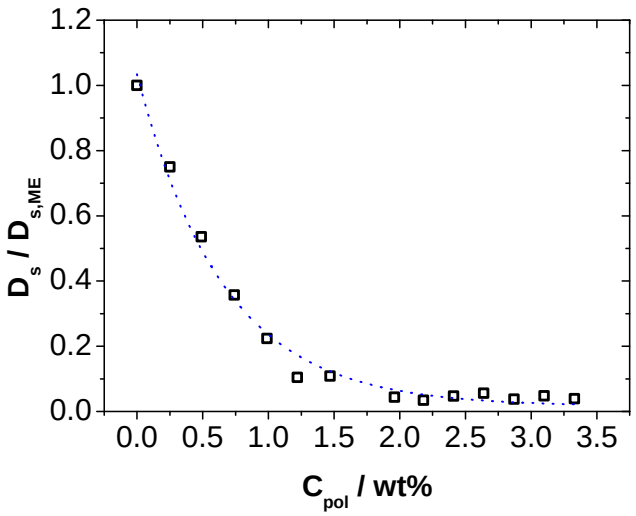

Figure 5.13: Reduced self diffusion coefficient $D_s/D_{s,ME}$ calculated as $D_s = w_0/(4\tau_D^{\alpha})$. $D_{s,ME}$ is the self diffusion coefficient of the microemulsion without polymer. The dotted line is a guide to the eye

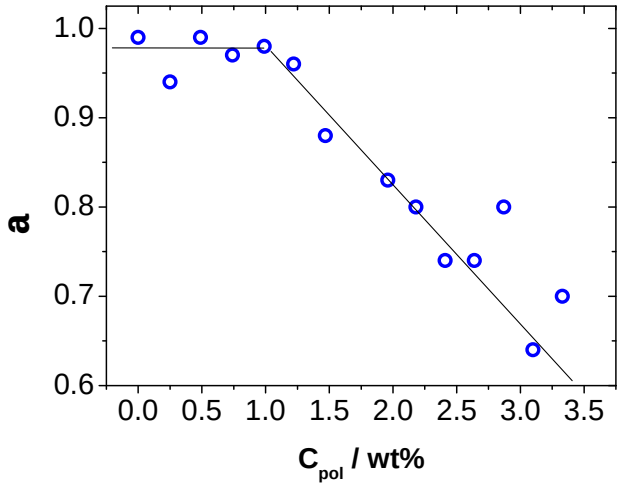

Figure 5.14: Anomalous diffusion exponent α as a function of the concentration of C_{18}-EO_{150}-C_{18} for microemulsion/ HM-polymer obtained by fitting the FSC autocorrelation functions with Eq. 2.47. The lines are only guides to the eyes.

5.6 Conclusion

The structure and dynamics of an oil in water microemulsion with admixed telechelic polymer with structure C_{18}-EO_{150}-C_{18} has been studied in detail. SANS experiments showed that the form and size of the oil droplets are not modified by the presence of the polymer. However, the addition of telechelic polymer induces an attractive interaction due to the bridging and a repulsive interaction due to the presence of the chains between the droplets. At low polymer concentration, the attractive component dominates, whereas the repulsive part becomes more important by adding more polymer.

Moreover, the polymer induces a considerable increase in viscosity of several orders of magnitude. The concentration dependence of the viscosity was described with a percolation model, yielding a percolation concentration of 1.5 wt% or equivalently 7 stickers per droplet. Above the percolation concentration, the samples show a viscoselastic behavior, that was described by an almost perfect simple Maxwell model with one relaxation time. The structural relaxation time is constant ($\sim$ 60 ms) with the polymer content. The high freaquency modulus and zero shear viscosity may be described by a percolation model yielding a percolation concentration of 1.37 and 1.55 wt% respectively. Since the relaxation time was constant with the polymer concentration, the exponent of the concentration dependence over the percolation threshole was in both cases 1.7, in excellent agreement with the values predicted by percolation theory [116].

The concentration fluctuations show a multimodal relaxation process that was modeled by a sum of two stretched exponential functions. The fast mode is diffusive and the collective diffusion coefficient decreases with the polymer concentration as a consequence of the attractive interdroplet interactions. The relaxation time of the slow mode increases with the polymer concentration and its dependence with the scattering vector q varies from 2 (diffusive) to almost zero (subdiffusive). The relaxation time in the latter case appears to be correlated to the structural relaxation time τ_R obtained by rheology.

FSC measurements show an increase of the diffusion time with the number of polymer molecules per droplet. The self diffusive behavior changes qualitatively from normal to anomalous diffusion at a polymer concentration of about 1.0 wt %, which corresponds to 4.5 stickers per droplet. This behavior, typical for diffusion of bodies in crowded media, is a clear indicator of the beginning of the network formation.

The beginning of the formation of a network is characterized by a minimum in the

value of the second virial coefficient, a minimum in both in the collective and self diffusion coefficients, the appearance of a slow relaxation mode in the density and concentration fluctuations and the start of anomalous diffusion.

Chapter 6

Structure and Dynamics of telechelic star polymer and microemulsion mixtures

The structural and dynamical properties of oil-in-water microemulsion (O/W ME) modified with telechelic linear and star polymers of different functionality (number of hydrophobically end-capped arms) were studied by means of DLS, SANS, and high frequency rheology measurements. For that purpose tailor-made newly synthesized hydrophobically end-capped poly(N,N-dimethylacrylamide) (PDMA) star polymers of variable number of end-caps of different alkyl chain length, synthesized by the RAFT method were employed.

6.1 Systems studied

As a first step the macroscopic phase behavior of the microemulsions composed of 100 mM TDMAO / 35 mM decane was studied as a function of the amount of the different (Table 6.1) added polymers. All the mixtures of microemulsion and polymer up to 8 wt% of polymer are homogeneous, transparent and stable but they differ substantially with respect to their viscosity. Samples with C4 end-capped polymer are liquid-like, with C12 viscous, and with C18 very viscous (honey-like). In general, an increase of the polymer concentration leads to a pronounced increase of the systems viscosity.

The molecular parameters of the polymers used in this study are listed in Table 6.1. The number of stickers per droplet r is the ratio between the number density of stickers

Polymer	n	M_n^a/KDa	M_w^a/KDa	PDI^a	M_w^b	R_{ee}(2 arms) / nm	r/wt%^{c}
$(C_4PDMA)_3$	493	147	169	1.15	219	28.4	0.15
$(C_{12}PDMA)_2$	293	59	61	1.05	73	21.9	0.38
$(C_{12}PDMA)_3$	221	67	69	1.04	86	19.2	0.49
$(C_{12}PDMA)_4$	229	92	97	1.05	120	19.4	0.48
$(C_{18}PDMA)_3$	330	nd	nd	nd	109	24.0	0.32

Table 6.1: Polymer parameters: Molar mass as weight (M_w), and number (M_n) average as determined by MALLS-GPC; DMA units per arm (n) as calculated from M_n and polydispersity index (PDI) and end-to-end distance of 2 arms (R_{ee}) calculated as $< R_{ee}^2 >= C_\infty 2nl^2$ ($C_\infty = 9.1$) [92]. ^{b} Weight average molar mass M_w obtained from SANS in d8-THF as reported in ref [91]. ^{c} Number of stickers per droplet r per 1 wt % of polymer.

n_{St} and the number density of droplets $n_d = \phi/V_p = 3\phi/4\pi R^3$, assuming all end stickers to be located within the microemulsion droplets.

$$r = n_{St}/n_d \tag{6.1}$$

with R being the radius obtained by SANS (2.4 nm).

The average distance between the microemulsion droplets can be calculated assuming a cubic packing of the spheres $d = \sqrt[3]{4\pi R^3/3\phi}$, for the given concentration and for their radius of 2.4 nm. This yields a value of d=13.2 nm for our system of 100 mM TDMAO and 35 mM decane (which has a volume fraction of 0.0357). This distance is somewhat shorter than the send-to-end distance R_{ee} of the bridging polymers (see Table 6.1), which means that the polymers should be able to bridge the droplets effectively [52], and thereby even would have a tendency to be "squeezed together" by the presence of the droplets. The end-to-end distance of two arms (listed in Table 6.1) was calculated as $< R_{ee}^2 >^{1/2}= (C_\infty 2nl^2)^{1/2}$ where l is the length of a N,N'-dimethylacrylamide monomer (0.23 nm) and $C_\infty = 9.1$ for PDMA in water [92].The length of two arms of the polymers is about 20 nm (See Table 6.1). This length can be compared to the distance between the droplets, that is 13 nm. Note, that the length of the polymers is considerably larger than the distance between the droplets. Therefore, we expect a network to form easily. Furthermore, no phase separation is expected [41].

6.2 Structure of the Microemulsion/Polymer Systems - SANS

Comprehensive mesoscopic structural information is required for a better understanding of the formed microemulsion/polymer mixtures. For this reason SANS measurements were performed for samples with microemulsions (TDMAO 100mM/Decane 35mM/D_2O) and telechelic star polymer added, where the length of the sticker, the concentration of polymer and the number of arms were varied.

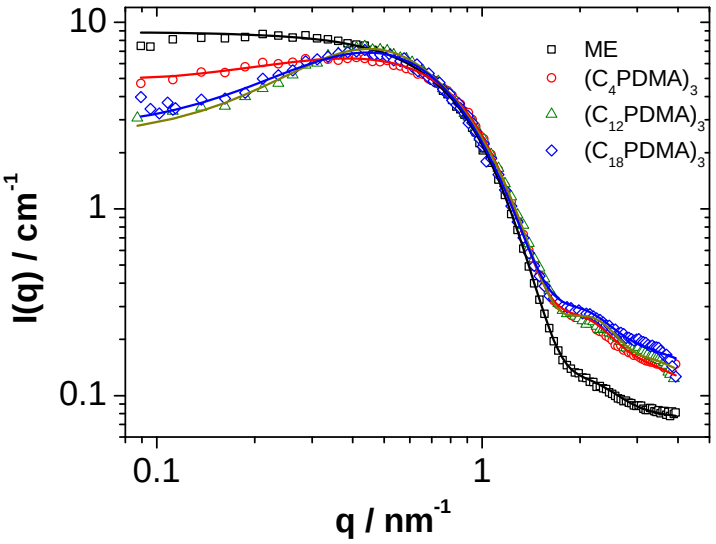

Figure 6.1: SANS patterns of the aggregates of microemulsion (squares) and with $(C_4PDMA)_3$ (circles), $(C_{12}PDMA)_3$ (triangles) and $(C_{18}PDMA)_3$ (diamonds) at a concentration of 5 wt% added polymer in D_2O at room temperature. The lines correspond to the fits with eq.6.2

Figure 6.1 shows scattering patterns of the pure microemulsion and the system with 5 wt% of 3-arm polymers with varying end-cap length (4, 12 and 18 carbon units). The pure microemulsion shows the typical scattering pattern of sterically repulsively interacting spherical aggregates. The polymer-containing samples show a much more pronounced correlation peak and a higher scattering intensity in the high q-range. The latter is due to the scattering of the polymer chains and to an increased incoherent scattering due to the higher concentration of H-atoms in the sample. In the intermediate q-range the scattering curves are basically superimposed. This indicates that the droplet structure of the microemulsion remains unaltered by the polymer addition. The decreasing scattering intensity at low q and the corresponding evolution of a correlation peak arises from an

increased repulsive interaction due to the presence of the polymer chains between the microemulsion droplets. This leads to an effectively excluded volume between the droplets. The scattered intensity for polymer containing microemulsion droplets was expressed by the expression derived by Fuchs et al. [117] for polymer-colloid mixtures:

$$I(q) = n_s V_s^2 \Delta\rho_s^2 P_s(q) S_{ss}(q) + n_p V_p^2 \Delta\rho_c^2 S_{pp}(q) + I_{inc} \tag{6.2}$$

The total scattering intensity $I(Q)$ is expressed in terms of the droplet and polymer segment scattering lengths, $\Delta\rho_s$ and $\Delta\rho_p$, V_s and V_p their volumes, and their number densities n_c and n_p, the normalized form factor accounting for the shape and size of oil droplets ($P_s(q)$). $S_{ss}(q)$ is the structure factor accounting for interactions between droplets and I_{inc} accounts for the incoherent scattering. Cross terms taking into account the correlations between the droplets and the polymer were neglected here. The decoupling of $P(q)$ and $S(q)$ is strictly only valid for monodisperse systems, but commonly employed as well for polydisperse systems [111]. For $P_s(q)$ the model of an homogeneous sphere was employed,

$$P_s(q) = n_s \int LogNorm(R) \left(3\frac{sinqR - qRcosqR}{(qR)^3}\right)^2 \tag{6.3}$$

with the spherical particles having a log-normal size distribution of radii:

$$LogNorm(R) = n_s/R\sigma(2\pi)^{1/2} exp(-[ln(R) - \sigma]^2/2\sigma^2) \tag{6.4}$$

The polydispersity index PDI of this distribution is identical to the variance σ. The values of $\Delta\rho$ are the difference of the scattering length density of the aggregates and the average scattering length density of the sample, which depends on the sample composition. (described it in more detail in the supporting information).

$S_{pp}(q)$ is the structure factor of the polymer segments and there is no explicit polymer form factor. The scattering can be modeled according to a correlation term [22]:

$$n_p V_p^2 \Delta\rho_c^2 S_{pp}(q) = \frac{\alpha}{q\xi}\Gamma(\mu)\frac{sin(\mu arctan(q\xi))}{(1 - q^2\xi^2)^{\mu/2}} \tag{6.5}$$

with $\Gamma(\mu)$ the gamma function with argument $\mu = 1/\nu - 1$ and ν being the excluded volume parameter from the Flory mean field theory with a value of $\nu = 3/5$, as typical for polymers swollen in good solvents. The parameter α is the forward scattering and ξ is the

correlation length of the polymer network.

For the long range repulsion we employed a S(q) based on a potential U(r) of a hard sphere with a Yukawa tail [118]:

$$\frac{U(R)}{k_B T} = \begin{cases} \infty & \text{for } 0 < R < R_{HS} \\ U_0 exp(-z(R - R_{HS}))/r & \text{for } R > R_{HS} \end{cases} \tag{6.6}$$

where R_{HS} is the hard sphere radius. For $R > R_{HS}$ a Yukawa potential was chosen as it has been proven to successfully describe the long range repulsion, for instance in electrostatically repulsive colloids [119] or soft colloids such as star polymers [72]. The radius and the volume fraction of the hard sphere in this model are constrained to be defined by those of the sphere form factor. The parameter U_0 is the potential energy at the particle surface and z its range. The direct correlation function C(r) is obtained by solving the Ornstein-Zernike equation which has an analytical solution for the mean spherical approximation (MSA) [118]. The Fourier transformed correlation function C(q) solved for macro-ion solutions was taken [**?**] and the structure factor is

$$S(q) = \frac{1}{1 + n_s C(q)} \tag{6.7}$$

where n_s is the number density of the oil droplets.

In addition, we studied the effect of the polymer concentration. Exemplarily, the scattering patterns of the pure microemulsion and the microemulsion with 2, 5 and 8 wt% of $(C_{12}PDMA)_3$ are shown in Figure 6.2(a). As observed above, the scattered intensity increases at high q due to the incoherent scattering and the scattering of the chains. Both contributions increase proportionally to the amount of polymer. Again, the size of the microemulsion droplets, as indicated by the intermediate q-range, is not affected. With increasing polymer concentration the correlation peak becomes more pronounced. This indicates a higher repulsive interaction due to a larger amount of hydrophilic polymer chains between the droplets, that are functioning like an effective excluded volume.

Finally, in order to elucidate the effect of the number of arms the SANS patterns for 5wt% solutions of $(C_{12}PDMA)_2$, $(C_{12}PDMA)_3$ and $(C_{12}PDMA)_4$ with similar molecular weight in microemulsion are given. They show no significant difference at identical polymer concentration (Figure 6.2(b)). This means that neither the droplet structure nor their

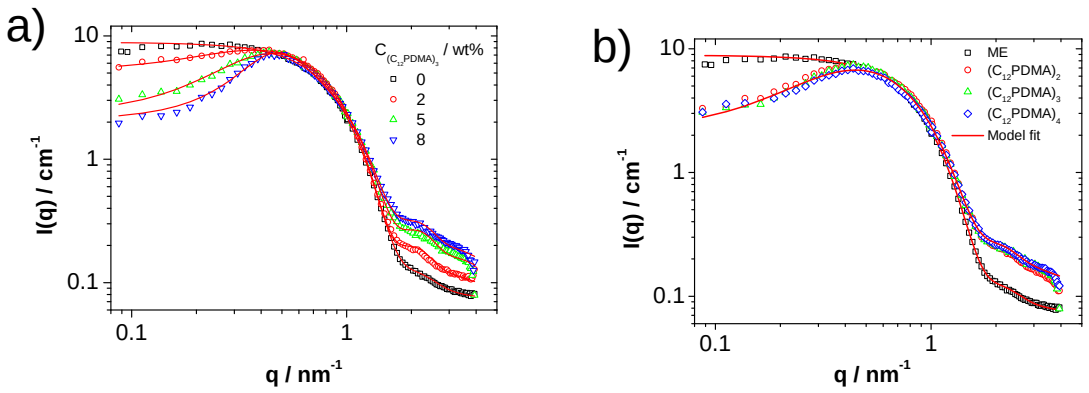

Figure 6.2: SANS patterns of the aggregates of microemulsion at room temperature (a) with increasing content of added $(C_{12}PDMA)_3$ and (b) with $(C_{12}PDMA)_2$, $(C_{12}PDMA)_3$ and $(C_{12}PDMA)_4$ at a concentration of 5 wt% added in D_2O

interactions are affected by the number of arms of the polymer present.

The fit of the curve of the pure microemulsion by using the model described by Eq. 6.2 without the chain contribution $P_c(q)$ (the second term in Eq. 2) yields a radius of 2.4 nm with a standard deviation of the log-normal distribution of 0.18. This value is higher than the previously reported one of $\sigma = 0.102$ [57], because it also contains the experimental smearing.

The curves of the polymer containing samples were fitted using Equation 6.2. The radius of the droplets R, and the standard deviation of the log-normal distribution σ were kept constant according to the values obtained from the microemulsion. The volume fraction was fixed according to the sample composition. The scattering length density difference was calculated as the difference of the scattering length of the droplets and the sample average scattering length density (see supp.info). The hard sphere radius R_{HS} and the hard sphere volume fraction ϕ_{HS} were chosen to be equal to the microemulsion droplet radius and droplet volume fraction, respectively. In this way, the number density is kept constant and the number of parameters in decreased. R_{HS} might be slightly larger for the droplets but this additional repulsion is included in the interaction potential. The prefactor of the chain scattering form factor α, the blob size ξ, and the structure factor parameters U_0 and z were fitted. All the parameters are listed in Table 6.2. This model fits our experimental data rather well, and accordingly seems to be an accurate description of the structural situation.

As to be expected, α is simply proportional to the amount of polymer contained (see

Polymer	C [wt%]	ϕ	r	I_{inc} [cm^{-1}]	α [cm^{-1}]	$\Delta\rho$ [cm^{-2}]	z [nm^{-1}]	U_0 [k_BT]	B_2
-	0.0	0.032	0			6.43	0.106	0.03	4.11
$(C_4PDMA)_3$	5.0	0.031	1.1	0.077	0.81	6.17	0.134	0.11	7.11
$(C_{18}PDMA)_3$	5.0	0.031	1.7	0.107	0.82	6.17	0.049	0.81	13.8
$(C_{12}PDMA)_3$	2.0	0.032	1.0	0.076	0.38	6.32	0.153	0.19	4.37
$(C_{12}PDMA)_3$	5.0	0.031	2.7	0.093	0.81	6.17	0.079	1.20	13.8
$(C_{12}PDMA)_3$	8.0	0.030	4.5	0.11	1.09	6.01	0.114	3.94	18.2

Table 6.2: SANS parameters of the curves presented in Figures 3 and 4. Polymer concentration C, droplet volume fraction ϕ, number of stickers per droplet r, scattering length density contrast $\Delta\rho$ and the parameters obtained from the fits using Eq.2: incoherent background I_{inc} (error: 0.9%), prefactor of the polymer chain correlation term α (error: 3%), the range z (error: 10%) and the strength U_0 (error: 6%) of the repulsive interaction potential. The radius of the sphere R (and hard sphere radius R_{HS}) was 2.37 nm (error: 0.2%) and the chain blob size ξ was 1.82 nm (error: 0.2%). The hard sphere volume fraction ϕ_{HS} was the same as the droplet volume fraction.

Table C3). The parameters z and U_0 are strongly coupled but nonetheless there seem to be some clear trends to be observed for the different systems. When the same concentration of $(C_{12}PDMA)_3$ and $(C_{18}PDMA)_3$ is added, U_0 and z are relatively similar. This is not surprising since both polymers have the same length and the same number of chains are present in the sample. In the case of $(C_4PDMA)_3$, U_0 is substantially lower because the smaller anchoring of the short C4 chain in the microemulsion droplets is much weaker and accordingly it only leads to a much less pronounced repulsion. Therefore, we can state that the structure does not depend on the sticker length, if the sticker has a minimum length. This is in good agreement with previous results with C12 and C18 telechelic polymers, where the effective interaction between the droplets was found to be independent of the sticker length [44]. The effective interaction must be independent of the nature of the stickers, if the time they spend out of the droplets is negligible. This does not hold for the C4 stickers, and thus the effective repulsion is less pronounced.

Moreover, we observe a pronounced increase of U_0 with increasing polymer concentration, which is in agreement with the intuitively expected proportionality of K to the number of stickers per droplet, r. In order to quantify the interaction in a more stringent way, we calculated the dimensionless second virial coefficient as

$$B_2 = \frac{2\pi}{V}\int_0^\infty (1 - exp(-U(r)/k_BT))r^2 dr \tag{6.8}$$

From the definition of B_2, the excluded volume contribution is represented by $B_2 = 4$. If $B_2 < 4$ the interaction is attractive and if $B_4 > 4$ the interaction is repulsive. The results are summarized in Table 6.2. The second virial coefficient B_2 for the microemulsion is 4, i.e., it behaves like a model hard sphere system as it has been seen frequently before for nonionic microemulsions [4, 57, 105, 110, 120–122].

In general, the microemulsion/polymer mixtures have values of B_2 higher than 4 (see Table6.2), indicating that the net interaction between the droplets is repulsive. B_2 is proportional to the number of stickers per droplet r, and apparently, each connecting chain has a similar contribution to the overall repulsion. The repulsion itself arises from the fact that the end-to-end distance of the polymers, which is also the average spacing between the hydrophobic stickers, is larger than the average spacing between the microemulsion droplets. Accordingly having two stickers in neighboring droplets leads to a repulsion between them. In contrast, if the polymer length is smaller than the interdroplet distance, the net interaction is expected to be attractive, leading to phase separation [40, 53].

In summary, we find that the addition of the telechelic polymers has virtually no effect on the droplet structure of the microemulsions, but mainly affects their interaction potential and thereby their structure factor, rendering the droplet interactions increasingly repulsive.

6.3 Rheology

In order to gain quantitative insight into the thickening behavior of the end-capped star polymers, we performed rheological measurements for the polymers of various architectures and different sticker lengths.

First, we considered the effect of the sticker length on the viscosity of microemulsion-3-arm polymer mixtures. Fig. 6.3(a) shows oscillatory measurements of samples with 5 wt% of $(C_{12}PDMA)_3$ and $(C_{18}PDMA)_3$. The curves show the typical behavior of a viscoelastic fluid with an increase of the storage modulus G' and the loss modulus G'' with increasing frequency until at a certain frequency where G' reaches a plateau. The viscoelastic behavior can to a first approximation be described by the Maxwell model, described by Equations 6.9 and 6.10.

$$G' = G_0 \frac{\omega^2 \tau_R^2}{1 + \omega^2 \tau_R^2} \tag{6.9}$$

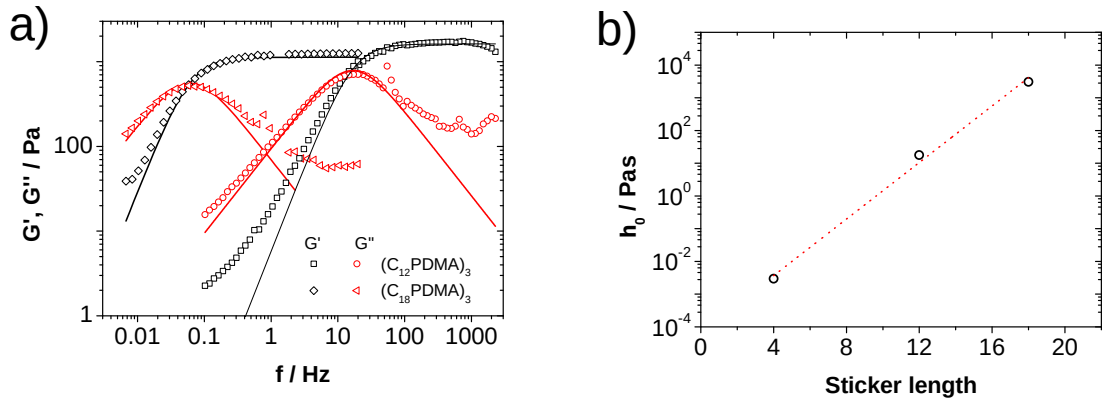

Figure 6.3: a) Storage (G') and loss modulus (G'') as a function of the frequency (f) solutions of $(C_{12}PDMA)_3$ and $(C_{18}PDMA)_3$ of a concentration of 5wt% (solid lines are fits with Eqs. 6.9 and 6.10).b) Effect of end-cap chain length in terms of carbon units on the zero shear viscosity for a concentracion of 5wt%. The dotted line represents the fit using $\eta_0 \sim \exp(E_a^*/k_BT)$.

$$G'' = G_0 \frac{\omega\tau_R}{1+\omega^2\tau_R^2} \tag{6.10}$$

where G_0 is the shear modulus, and τ_R is the characteristic time of the relaxation process and the angular frequency is $\omega = 2\pi f$. This simple model describes the experimental data very well. Deviations at high frequency, especially in the case of G'', appear in such systems because in this frequency regime the links can be regarded as permanent and the system behaves rather rubber-like yielding a higher G'' than predicted by the Maxwell model [110]. The obtained values of G_0 and τ_R are collected in Table 6.3. The plateau modulus G_0 for C12 and C18 is of the same order of magnitude and the slight difference can be attributed to the somewhat different number of stickers per droplet r. The structure of the network is very similar as observed by SANS. However, the structural relaxation time differs markedly depending on the sticker length for C12 and C18. The structural relaxation time is related to the lifetime of a network junction. Assuming that the lifetime is the residence time of the alkyl chain of a surfactant in a micelle, it is related to the activation energy E_a for the exit of a sticker from the microemulsion droplet by the Arrhenius law $\tau_0 \sim \exp(E_a/k_BT)$. For linear saturated chains, the activation energy is 1.1-1.2 k_BT per CH_2 [?]. The relaxation time of the C18 stickers is 300 times larger than for C12, corresponding to an E_a of 1.0 k_BT per CH_2.

The zero shear viscosity is directly proportional to the structural relaxation time $\eta_0 = \tau_R G_0$. Figure 6.3(b) shows the zero-shear viscosity η_0 for the samples containing 5 wt% of

Polymer	C/ wt%	r	η_0/Pas	G_0/Pa	τ_R/ms	D_{eff}/m^2s^{-1}	$<\tau_2>/ms$	β_2
$(C_4PDMA)_3$	5	0.76	$2.95{\cdot}10^{-3}$			$5.78\cdot10^{-11}$	1.02	0.66
$(C_{12}PDMA)_3$	5	2.5	17.1	1608	11.1	$7.40\cdot10^{-11}$	64.7	0.31
$(C_{18}PDMA)_3$	5	1.6	$3.09\cdot10^3$	1129	$2.73{\cdot}10^3$	$6.60\cdot10^{-11}$	$4.36{\cdot}10^3$	0.68

Table 6.3: Rheological parameters for different sticker lengths obtained from the fit with Eqs. 6.9 and 6.10: plateau modulus G_0, relaxation time τ_R and zero shear viscosity. As the sample with $(C_4PDMA)_3$ was too fluid to be measured with the Gemini rheometer, the viscosity was measured with a capillary viscometer. In addition, effective diffusion coefficient D_{eff}, mean value of the second relaxation time $<\tau_2>$, and stretching parameter β_2 as obtained from DLS.

3-arm polymers with different stickers. One observes a very pronounced viscosity increase, which rises exponentially with the number of methylene groups of the sticker in the form of $\eta_0 \sim \exp(E_a^*/k_BT)$, yielding a value of 1.0 k_BT per CH_2 group. Since the values of the plateau modulus G_0 are very similar, the viscosity variation is dominated by the variation in the relaxation time. This value is close to the 0.9 K_BT reported before [27] for the viscosity of linear hydrophobically end-capped polymers. The somewhat higher viscosity values in our case suggest that the trithiocarbonate group adds hydrophobicity to the sticker.

In the next step, we consider the variation of the polymer concentration. The mixtures of telechelic star polymers and microemulsions exhibit an increase on the viscosity upon increasing concentration of polymer, such that the relaxation time and the value of the plateau modulus become higher (Fig. 6.4).

The evolution of the plateau modulus G_0 with the number of stickers per droplet r for different number of stickers per polymer is illustrated in Figure 6.5. We note that the values of the plateau modulus differ largely for the three polymers at a given concentration, where SANS shows no differences on the local structure and only small changes in the interaction potential. From the percolation theory [116] one expects

$$G_0 = G_{00}(r - r_c)^a \tag{6.11}$$

where r_c is the percolation threshold and a is predicted to be about 1.7 [116]. The percolation threshold r_c is 0.93, 0.8 and 0.6 for $(C_{12}PDMA)_2$, $(C_{12}PDMA)_3$, and $(C_{12}PDMA)_4$, respectively. This decrease may be explained by a decreasing probability of having a polymer not connecting different droplets but instead forming loops. The best results were

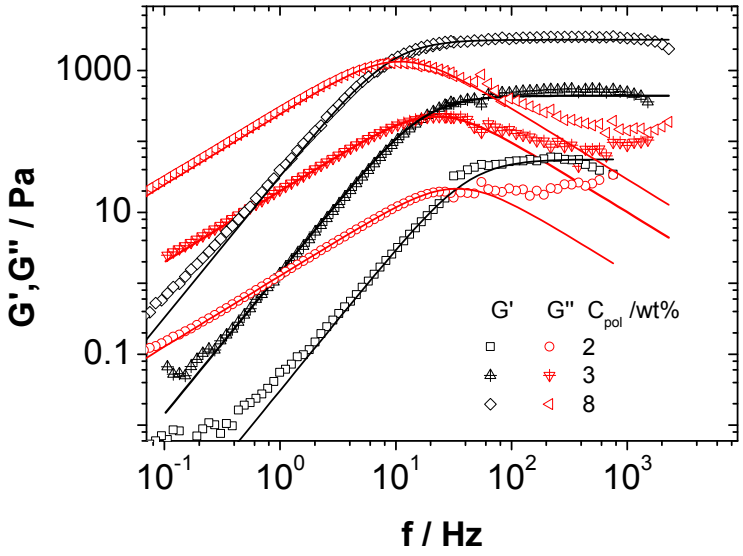

Figure 6.4: Storage (G') and loss modulus (G'') as a function of the frequency (f) for solutions of $(C_{12}PDMA)_3$ in microemulsion (35 mM TDMAO/100 mM decane) for different polymer concentrations. The symbols correspond to the experimental data, the lines to the fit analysis with the Maxwell model (Eqs. 6.9 and 6.10)

Polymer	G_{00} / Pa	r_p
$(C_{12}PDMA)_2$	480	0.93
$(C_{12}PDMA)_3$	600	0.80
$(C_{12}PDMA)_4$	786	0.64

Table 6.4: Fit parameters to the the power law $G_0 = G_{00}(r - r_c)^{1.2}$ of the plateau modulus as a function of the number of stickers per droplet r for $(C_{12}PDMA)_2$, $(C_{12}PDMA)_3$ and $(C_{12}PDMA)_4$ added to the microemulsion.

found for a value of the exponent $a = 1.2$. This value differs somewhat from the one predicted by theory (1.7) [116] and found experimentally for microemulsions with bifunctional telechelic polymers (1.4-1.6) [108, 110, 123]. Hence, the curves follow the same power law but they differ in the magnitude of the modulus, being larger with increasing number of arms.

The inset of Figure 6.5 shows the relaxation times obtained from the fits of the rheological data using Eq. 6.9. Interestingly, all fall on top of each other, i.e., they are described by a master curve for the various systems studied. The relaxation process depends only on the sticker length and the effective connectivity of the droplets. Experimentally we find that τ_R follows a power law of r with an exponent of 0.66, where this exponent describes the increase of connectivity due to the increasing number of bridges present. For a

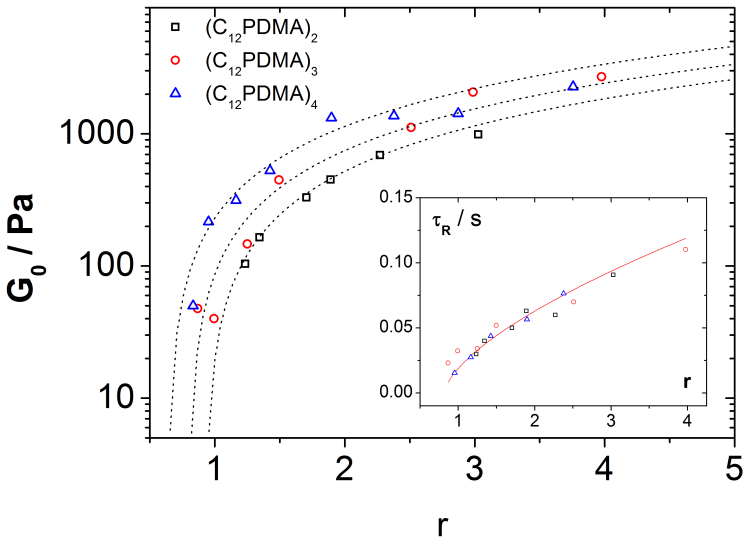

Figure 6.5: Plateau modulus as a function of the number of stickers per droplet r. The lines are the fits to the power law $G_0 \propto (r - r_c)^{1.2}$ (see Table 6.4). The inset shows the relaxation time τ_R as a function of r. The line corresponds to the equation $\tau = 8(r-0.8)^{0.66}$

simple network model G_0 is proportional to the number density, n, of rheologically active cross-linking points [107]

$$G_0 \cong nk_BT \tag{6.12}$$

where n can be approximated by the number density of polymer chains linking two droplets. For our multi-bridging polymers the number of links will be related to the number of arms f by:

$$G_0 = N_p f(f-1)k_BT \tag{6.13}$$

where n_p is the number density of polymer molecules. As r is fn_p/n_d (n_d being the number density of microemulsion droplets) we expect:

$$G_0 = rn_d(f-1)k_BT \tag{6.14}$$

This means that the shear modulus is expected to increase linearly with the number of branching points of the polymer. Indeed, all the data could be reasonably well fitted by the expression $G_0/n_pk_BT = 0.3(f-1)(r-r_p)^{1.2}$ (see Fig. 6.6).

The reduced modulus G_0/n_pK_BT, n_p being the number density of linking polymers, should be 1 for an ideal elastic network. However it is normally smaller due to network failures, such as dangling or backfolding arms, or due to higher order links. The ratio is

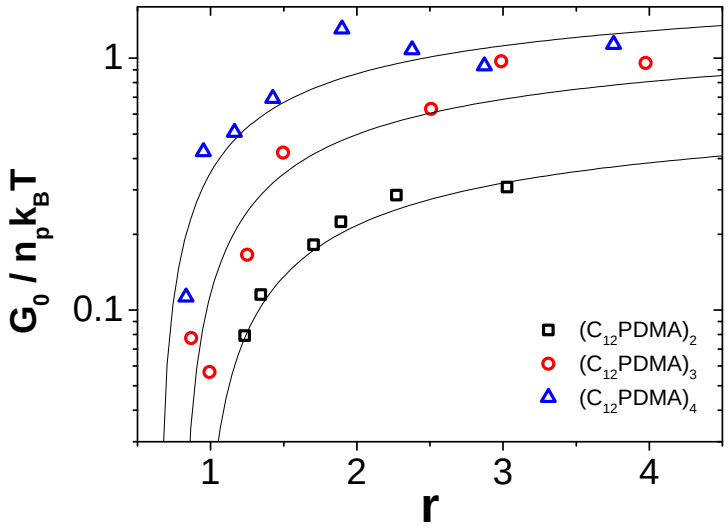

Figure 6.6: Reduced plateau modulus G_0/n_pk_BT as a function of the number of stickers per droplet r. n_p is the number density of linking polymers. The lines are $G_0/n_pk_BT = 0.3(f-1)(r-r_p)^{1.2}/r$.

approaching unity (see Fig. 6.6) with increasing r. This demonstrates that the portion of network failures is lower when increasing the number of arms from 2 to 4. Hence, the effectiveness of network forming increases with increasing number of end-capped arms in a polymer.

6.4 Dynamic Light Scattering (DLS)

The rheological results indicate rather complex dynamical properties of the multi-arm polymer / microemulsion system, that depend on concentration, sticker length, and number of arms. In order to gain further insight into these dynamical properties comprehensive DLS measurements were performed.

First, we consider the variation of the concentration. Figure 6.7(a) depicts the change of $g^{(2)}(t)$ as a function of the amount of added $(C_{12}PDMA)_2$. As to be expected, the pure microemulsion exhibits a single relaxation mode due to the diffusion of the droplets in the aqueous medium. The curve can be described by a single exponential function

$$|g^1(t)| = a_1 \exp(-t/\tau_1) \tag{6.15}$$

where the effective diffusion coefficient D_{eff} is related to the fast relaxation time as

$$D_{eff} = \frac{1}{\tau_1 q^2} \tag{6.16}$$

Thus, it can be related to the hydrodynamic radius R_H through the Stokes-Einstein equation $R_H = k_B T/6\pi\eta D$, where k_B is the Boltzmann constant, T the temperature, and η the viscosity of the solvent. The hydrodynamic radius R_H of the microemulsion droplets is 2.7 nm, which is in very good agreement with the radius obtained by SANS (2.4 nm). The somewhat higher value for R_H can be attributed to a hydration shell of the microemulsion droplets of 0.3 nm, as similarly deduced before from scattering experiments [57, 124, 125].

Upon addition of $(C_{12}PDMA)_2$ to the microemulsion, the obtained correlation functions change little until a concentration of about 1 wt% is surpassed (Fig. 6.7a). Only for concentrations above 2 wt% clearly a second much slower relexation mode becomes visible, while for the highest concentrations of 6 and 8 wt%, a third relaxation mode is observed clearly. This was seen before also for end-capped PEO in aqueous solution [15, 108]. This becomes further evidenced when looking at the CONTIN evaluation [126] of these autocorrelation functions (Fig. C5), where for the higher concentrations slower modes are clearly indicated, while the relaxation is monomodal without and for low polymer content. For the samples exhibiting a multimodal relaxation mechanism, this is also the concentration regime, where the samples become substantially more viscous.

The dynamic behavior depends also strongly on the number of arms of added telechelic polymer, as shown in Figure 6.7(b). The appearance of the slower relaxation becomes much more pronounced upon addition of $(C_{12}PDMA)_3$, and occurs already for lower polymer concentration. This trend is continued for the addition of the 4-arm telechelic polymer $(C_{12}PDMA)_4$ (Fig. C4). The presence of these slower relaxation modes is also visible from the corresponding CONTIN analysis (see Fig. C5). In general, the slowest relaxation mode moves to increasingly longer times upon increasing the polymer concentration, while the intermediate mode becomes smaller.

Typically a multimodal relaxation is observed for viscoelastic microemulsion/polymer networks, which becomes increasingly pronounced with increasing elasticity and number of arms of the telechelic polymers. However, compared to the rheological changes, DLS is much more sensitive to the multi-functionality of the polymers. Apparently the relaxation

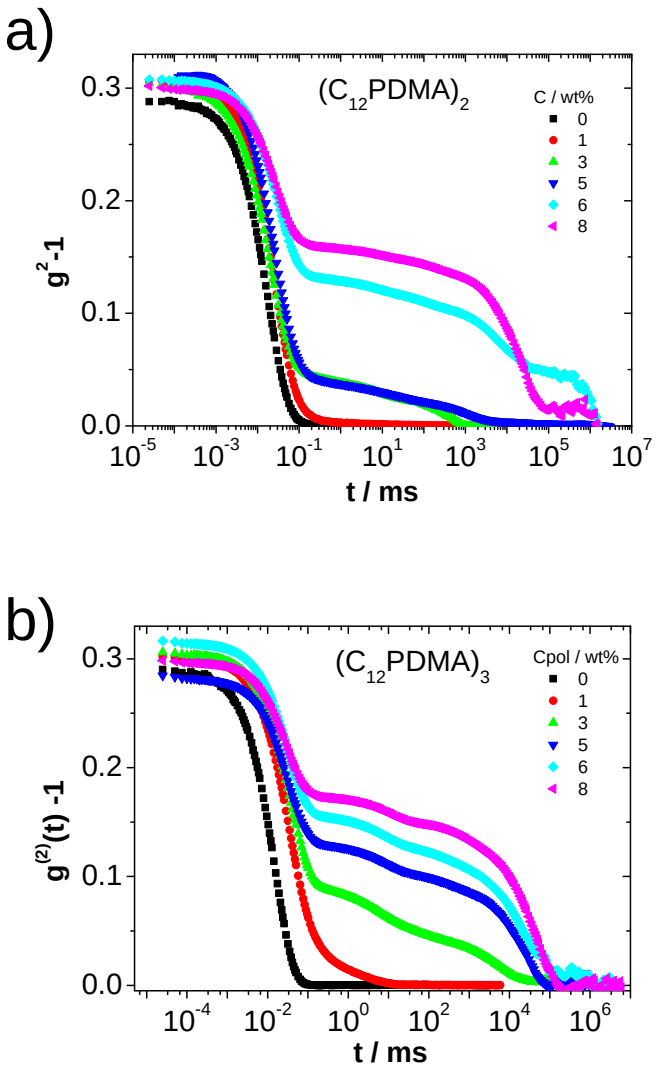

Figure 6.7: Intensity autocorrelation function $g^{(2)}(t) - 1$ as a function of time for (a) $(C_{12}PDMA)_2$ and (b) $(C_{12}PDMA)_3$ for various concentrations of polymer added to the O/W microemulsion (data taken at a scattering angle of 90° and a temperature of 25°C).

mechanisms observed by light scattering are very sensitive to the connectivity and the dynamic properties of the networks formed by bridging the microemulsion droplets. In addition to the fast relaxation that corresponds to the diffusion process of the individual microemulsion droplets, one observes an intermediate decay in the range of 10 ms and an additional slow and broad decay in the range of 1-100 s, i.e., in the range that is at the limit that can be explored by conventional DLS. These slower relaxation modes become more prominent with increasing polymer concentration and with the number of arms f.

The CONTIN analysis must be treated with caution as the distributions deduced often are too closely spaced to be reliable. Thus we analyzed the autocorrelation functions in

terms of a sum of normal or stretched exponential decays $g^{(1)}(t)$. Accordingly, the curves were fitted to a generalized Kohlrausch-Williams-Watt (KWW) equation [78–80]:

$$|g^{(1)}(t)| = a_1 \cdot e^{-t/\tau_1} + \sum a_i \cdot e^{-(t/\tau_i)^{\beta_i}} \tag{6.17}$$

A similar approach was applied before for describing the DLS data of an O/W microemulsion bridged by a PEO distearate [42]. In addition to the conventional diffusion of the microemulsion droplets (τ_1), this expression describes the additional relaxation modes of the viscoelastic network, by one or two stretched exponentials for the slower modes, respectively. The parameters a_i are the amplitudes for the respective relaxation modes with decay times τ_i and $\beta_i (0 < \beta < 1)$ is a measure of the width of the distribution of relaxation times [76]. The more β differs from 1, the broader the distribution of relaxation rates is. In general, Equation 6.17 allows for a quantitative description of the DLS data.

The slower relaxation processes can arise from different mechanisms which may be distinguished by the q-dependence of the relaxation time τ, which typically follows a power law ($1/\tau \sim q^{\alpha}$, α being 2 for diffusive processes).

As already stated above, the fast relaxation is purely diffusive as shown by the q^{-2} dependence of its relaxation time (see Figure 6.8). In contrast, the intermediate relaxation time τ_2 shows almost no q-dependence and therefore is apparently independent of size. For the case of viscoelastic polymer networks such a q-independent ($\alpha = 0$) relaxation has been reported before [81, 82]. In this case, the relaxation time is strongly correlated with the relaxation time of oscillatory shear experiments and thus was interpreted as the average lifetime of the network junctions [103, 108]. In our case, the relaxation time of the second relaxation mode τ_2 is in the same range as the rheological relaxation time (see Table 6.3), and remains constant with increasing polymer concentration (see Tables C4-6). The stretching exponent β_2 is typically in the range of 0.35-0.8, becoming somewhat larger with increasing polymer concentration (see Tables C4-6). Thus the values of β_2 observed are similar to the value of 0.82 reported before for PEO distearate [42].

The slowest relaxation mode shows a rather unspecific q-dependence. This has mainly to be attributed to the fact that for such long times, the limits of conventional DLS is reached and consequently, the relaxation times obtained have rather larger uncertainties. This applies similarly to β_3 which typically is in the range of 0.4-0.8, and increases somewhat when going from the 3-arm to the 4-arm polymer, thereby indicating to become a

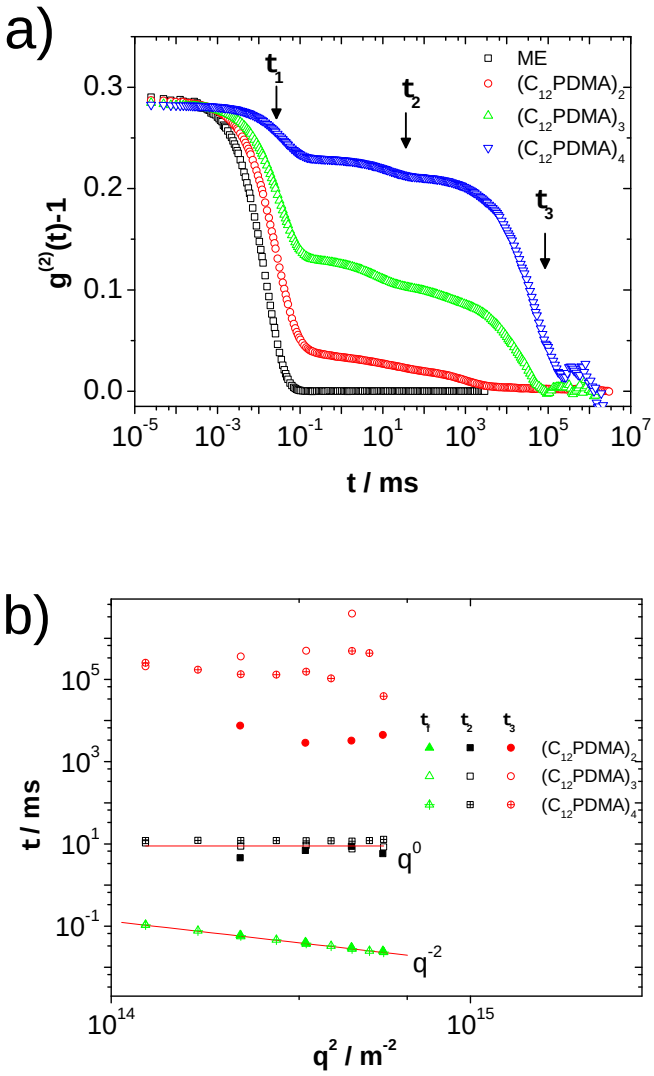

Figure 6.8: Intensity autocorrelations functions $g^{(2)}(\tau)$ (taken at 90°) (a) and q-dependence of the different relaxation times fitted using equation 6.17 for solutions of $(C_{12}PDMA)_2$, $(C_{12}PDMA)_3$ and $(C_{12}PDMA)_4$ 5wt% in microemulsion solution at a scattering angles from 50° to 130° and a temperature of 25°C

more well-defined relaxation process. The slowest relaxation mode could not be directly linked to structural features of the network. Most likely, it is associated with a kind of "breathing mode" of the network.

The effective diffusion coefficient of the droplets was obtained from the q^2 dependence of τ_1 calculated with Eq. 6.16 (see Fig. C4) for $(C_{12}PDMA)_2$, $(C_{12}PDMA)_3$ and $(C_{12}PDMA)_4$ at each measured concentration. Comparing the diffusion constant with the diffusion in the neat microemulsion, the fast relaxation may be assigned to collective diffusion of the microemulsion droplets as it has already been seen in previous investigations [42]. The relative effective diffusion D_{eff}/D_0 coefficient is depicted in Figure 6.9 (a) (where D_0 is the diffusion coefficient of the polymer-free microemulsion droplets). The ratio D_{eff}/D_0 first decreases with the polymer concentration indicating attractive interactions. This can be explained by the formation of dimers, trimers, etc. of connected microemulsion droplets for low content of bridging polymer. As to be expected for such a scenario, this effect becomes more pronounced with increasing number of arms as then the polymer is more effective in forming such small clusters of droplets. The subsequent rise of D_{eff} with increasing r is simply related to the increasing repulsive interaction between the droplets introduced by increasing concentrations of the polymer.

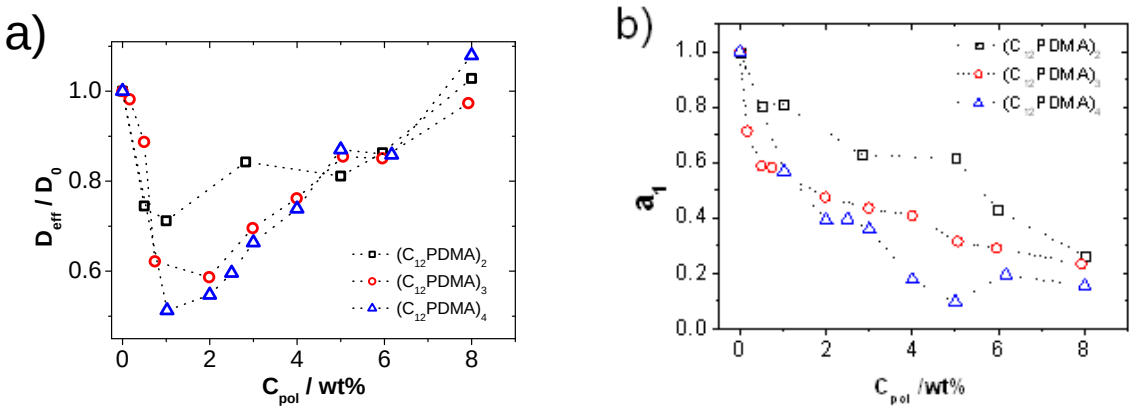

Figure 6.9: (a)Effective diffusion coefficient of the droplets and (b) amplitude of the fast relaxation mode for solutions of $(C_{12}PDMA)_2$, $(C_{12}PDMA)_3$ and $(C_{12}PDMA)_4$ in microemulsion as a function of the number of stickers per polymer.

At the same time, the reduction of the amplitude a_1 of the fast relaxation mode (Figure 6.9(b)) upon addition of polymer becomes more pronounced with increasing number of arms f, i.e., the slower modes become much more prominent. These slower relaxation modes

have to be related to the formation of a more complex network with increasing number of arms.

Finally, we consider the variation of the sticker length. The intensity correlation functions for microemulsion without, and with 5 wt% of 3-arm polymers added, which vary with respect to their end-cap length (4, 12 and 18 carbon units), are given in Figure 6.10. Again the intermediate relaxation time is of the same order of magnitude as the structural

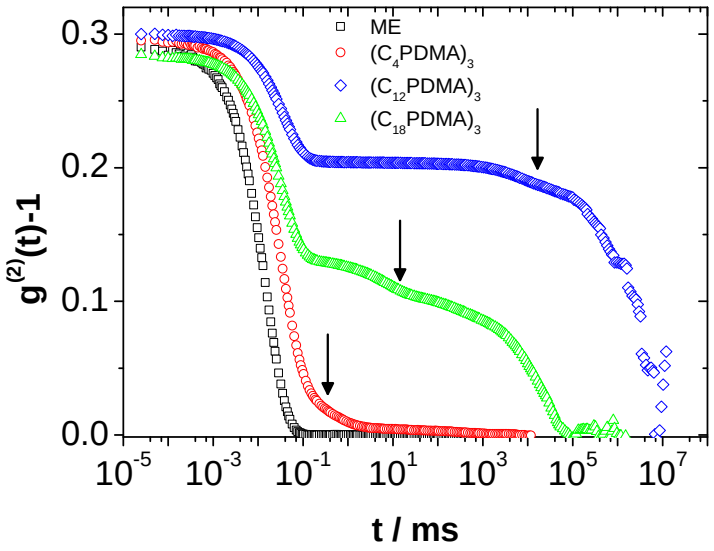

Figure 6.10: Intensity correlation function $g^{(2)}(t)$-1 as a function of time for systems of $(C_4PDMA)_3$, $(C_{12}PDMA)_3$ and $(C_{18}PDMA)_3$ 5wt% in microemulsion solution at a scattering angle of 90° and a temperature of 25°C. The arrows indicate the position of the second relaxation mode.

relaxation time from rheology (see Table 6.3). Moreover, it gives an activation energy per CH_2 group (as derived from the dependence of the time constant on the chain length of the alkyl sticker) of $0.6k_BT$ (for $\theta = 90°$) similar to the value from rheology experiments, corroborating the relation between this relaxation mode and the structural relaxation seen in rheology.

In general, it can be stated that the DLS experiments show the most pronounced and complex effects of polymer addition on the properties of the microemulsions, especially with respect to its dependence on the number of arms but also to the length of the stickers. While the network formation is clearly visible in the rheological properties, it leads to very pronounced changes of the DLS curves and additional, slower relaxation modes are observed. Apart from the fast relaxation, which can be attributed to the diffusion of the microemulsion droplets or clusters thereof, and the intermediate relaxation mode, which

is directly related to the rheological relaxation of the network, also a third still slower relaxation mode is observed that can not be connected to a simple structural relaxation process of the network. We suggest that this slowest relaxation is attributed to a breathing mode of the network, as indicated before for polymer networks [**?**].

6.5 Conclusions

The structure and dynamics of droplet O/W microemulsions with admixed telechelic multi-arm polymers are presented. The length of the hydrophobic alkyl sticker, the concentration of polymer and, in particular, the number of arms were varied. Though all microemulsions become more viscous upon polymer addition, the detail behavior depends strongly on the molecular architecture of the added polymer. An increase of the sticker length has an enormous impact on the rheology and on the dynamic properties due to a stronger affinity of the end-cap chain to the oil droplets. The viscosity of such systems scales with the relaxation time τ_R (via $\eta_0 = G_0\tau_R$), which is determined by the exit time τ_{exit} of an alkyl chain from a microemulsion aggregate, the latter increasing exponentially with the alkyl chain length ($\tau_{exit} \sim exp(n(CH_2))$.

At the same time, the structure of the microemulsion droplets, as seen by SANS, is hardly affected by the addition of polymer. Its presence only leads to an enhanced repulsive interaction, which is proportional to the polymer concentration and arises from the steric requirements of the hydrophilic polymer chain, irrespective of the number and the length of the stickers. This is a result of the fact that in our system the mean spacing between the microemulsion droplets is smaller than the end-to-end distance of the polymer chains (the natural spacing of the stickers). Under these conditions, the formation of loops is much less likely than the formation of bridges. In contrast, the effect of polymer addition on the dynamic properties as observed by DLS and rheology is much more pronounced and complex. These mixtures become increasingly viscous with polymer addition and the structural relaxation time of rheology depends strongly on the length of the hydrophobic sticker and the number r of polymer stickers per microemulsion droplet, while we find a universal scaling of τ_R on r, independent of the number of arms.

The shear modulus G_0 depends only little on the sticker length, but mostly on the sticker concentration, i.e., the network structure is generically the same. In contrast, the

rheological relaxation time does not depend on the number of arms, but increases with increasing sticker number per droplet. The effect of the polymer architecture is more subtle, we find that the shear modulus is proportional to the number of arms, as that determines the number of bridges between the microemulsion droplets. This might be the result of having less network failures when using polymers with higher functionalities, without affecting the fundamental morphology of the network formation significantly.

In DLS a second and third relaxation mode appear upon polymer addition. These become much more pronounced with increasing concentration and depend strongly on the number of arms and the length of the sticker. For the linear compound, i.e. the classical two arm system, only a small slower relaxation mode is observed in addition to the droplet diffusion mode. In contrast, for the 3- and 4-arm polymers, the two slow modes become dominant. The intermediate mode corresponds to the rheological relaxation and is independent of q. The slowest mode is attributed to some larger scale domain-like relaxation or "breathing" of the network, whose origin is not really clear at this moment. In parallel with rheology, one finds that the structural relaxation time increases largely with increasing sticker length. In general, these differences may be attributed to the increasing immunity against network ruptures with increasing number of arms [127].

In summary, the morphology of the polymers allows to control the dynamic properties of the networks formed by them over a large range. Accordingly, both the relaxation times and the shear modulus can be varied over several orders of magnitude. This allows to form microemulsions of relatively low viscosity up to effectively gelled ones and with relaxation times from the millisecond to the hours range. Rheology and the dynamical behavior in general can be controlled via the polymer concentration and, in particular, by the number of arms (for G_0) and the length of the hydrophobic sticker (for τ_R). This means that the architecture of these newly synthesized telechelic polymers is suitable for tailoring the rheological and dynamical properties of microemulsion over a large range, without affecting the basic microemulsion droplet structure, which may be a key for many of their future applications.

Chapter 7

Structure and phase behavior of telechelic star polymer and a nonionic microemulsion

Up to this point microemulsion networks with tailor made hydrophobically modified linear and star polymer, where the length of the hydrophilic chains, i.e. the length of the arms, was considerably larger than the interdroplet distance have been presented. However, when the end-to-end distance of the polymer chain is equal or smaller than the mean separation of the droplets, phase separation is expected to occur [40].

The phase separation between a highly connected phase in equilibrium with a dilute droplets, decorated by polymer, has a purely entropic origin [41]. Therefore, the phase behavior is very robust and will not depend on the detailed properties of the polymers or the drops. However, the polymer architecture should have an impact on the phase behavior of microemulsion/ HM-polymer mixtures. For this reason in this chapter presents the phase behavior, structure and dynamics of a nonionic microemulsion with an interdroplet distance comparable to the length of the polymers.

7.1 Pure Microemulsion

In order to characterize the effect of the telechelic polymers on the microemulsion, we

first characterized the microemulsion without polymer by means of SANS and DLS.

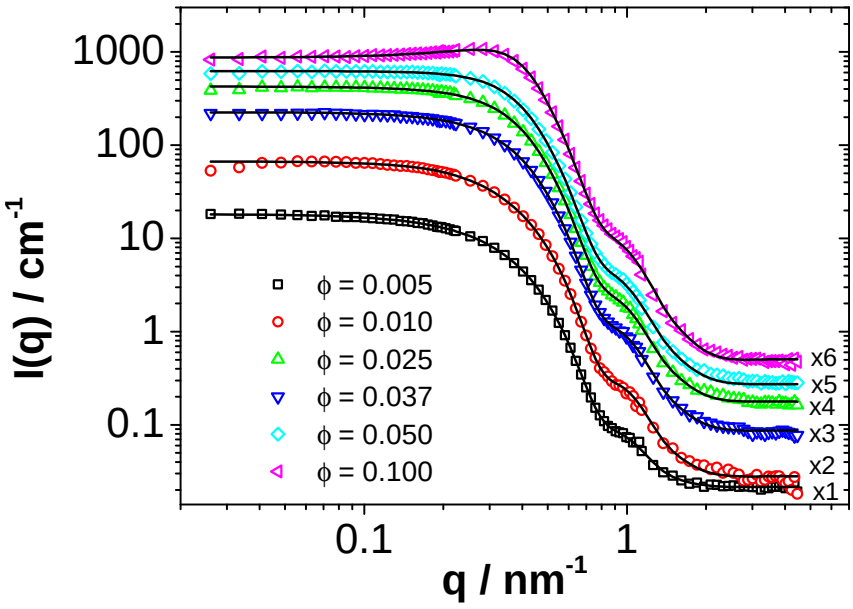

Figure 7.1: SANS intensity patterns of the pure microemulsion system TX100 / B30 / Decane / D_2O and different volume fractions ϕ. Each data set is vertically shifted by a factor n indicated next to the curve. Solid lines: Fits using Eq. 7.1

Figure 7.1 shows the Small Angle Scattering patterns of the pure microemulsion system TX100 / B30 / Decane / D_2O and different volume fractions ϕ. The scattering intensity is given by

$$I(q) = nV^2\Delta\rho^2 P(q)S(q) + I_{inc} \tag{7.1}$$

where n is the number density of scatterers, V their volume, $\Delta\rho$ the difference between the coherent scattering length density of the micellar unit and the one of the solvent, P(q) the form factor, and S(q) the structure factor that takes into account the interactions between the aggregates.

The curves were fitted with with a model of core-shell spheres with a monodisperse shell thickness and an inner radius R_{core}, with the density number N(R_{core}) having a log-normal size distribution (Eqs. 2.23 and 2.26) and the hard sphere structure factor (Eq. 2.30).

The fits, represented by the solid lines in Figure 7.2, are in very good agreement with the experimental data. Thus, our model provides an accurate description of the microemulsion structure. The fit parameters are collected in Table D.1. The hydrophobic core radius R_{core}=4.9 nm, the polydispersity $\sigma \approx 0.19$ and the shell thickness t_{shell}= 1.2 nm remain

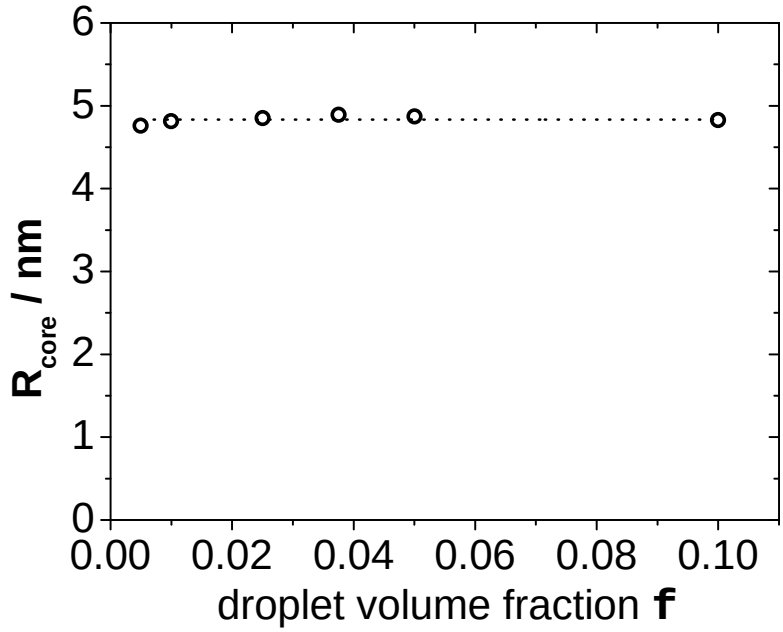

Figure 7.2: Radius of the hydrophobic core of the microemulsion obtained by fitting the SANS data with Eq. 7.1

constant for all droplet volume fractions between 0.005 and 0.1 within experimental accuracy.

The dynamic behavior of the pure microemulsion was studied by means of Dynamic Light Scattering. The intensity autocorrelation functions showed a single relaxation mode. The relaxation time τ could be extracted from a second order cumulant analysis [128, 129] of the intensity autocorrelation functions. The decay rate $\Gamma = \tau^{-1}$ varies linearly with the square of the scattering vector q and the slope is the collective diffusion coefficient $D_c = 1/\tau q^2$.

Figure 7.3 shows the collective diffusion coefficient as a function of the droplet volume fraction. D_c varies with the volume fraction as a consequence of the interparticle interactions [130]. We found a linear dependence of D_{coll} with the volume fraction: $D_{coll} = D_0(1 - k_D\phi)$ (solid line in Figure 7.3). We obtain a value of $k_D = 1.67$. The positive value of the slope k_D indicates a repulsive interaction, which is very near to the k_D value for a hard sphere interaction potential $k_D(\mathrm{HS}) = 1.45$ [131]. From the extrapolation of the diffusion coefficient D_{coll} to zero volume fraction a free diffusion coefficient $D_0 = 3.30 \cdot 10^{-11}$ $m^2 s^{-1}$ is obtained. The hydrodynamic radius, calculated through the Stokes- Einstein relation, is $R_H = 7.40$ nm. The radius obtained by SANS $R = R_{core} + t_{shell} = 6.02$ nm.

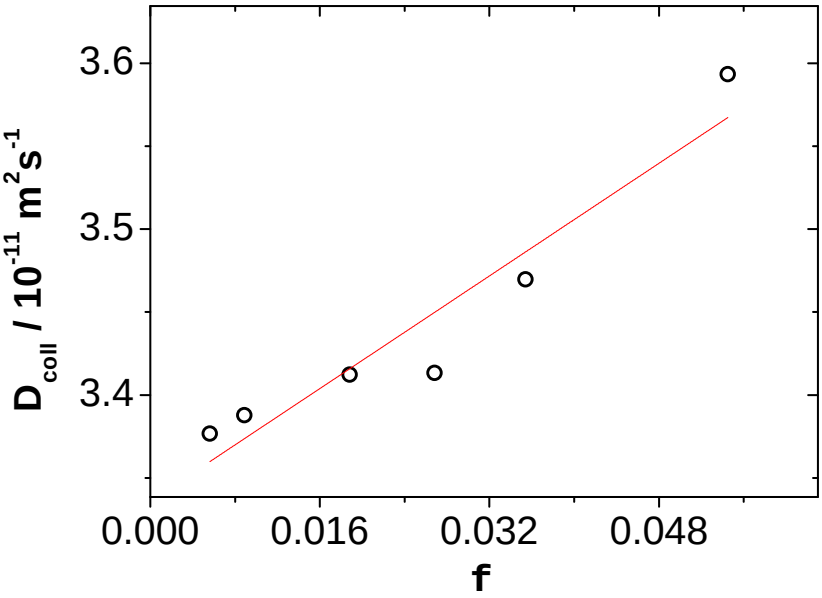

Figure 7.3: Collective diffusion coefficient D_{coll} as a function of the droplet volume fraction ϕ. Solid line: linear fit of $D_{coll} = f(\phi)$(see text)

This suggests that the ethylene oxide corona of the droplets is surrounded by a shell of hydration water. The hydrodynamic radius is closer to the hard sphere radius obtained by SANS $R_{HS} \sim 7.2$ nm.

7.2 Microemulsion with polymers

The molecular parameters of the polymers that we added to our microemulson are listed in Table 7.1. The end-to-end distance of 2 arms was calculated as $< R_{ee}^2 >= C_\infty 2nl^2$ ($C_\infty =$

Polymer	M_n/kDa	R_{ee}/nm
$(C_{12}PDMA)_2$	24.1	7.6
$(C_{12}PDMA)_3$	30.2	6.8
$(C_{12}PDMA)_4$	40.5	7.0
$(C_{12}PDMA)_3$	90	12.1

Table 7.1: Molecular parameters of the end-capped linear and star polymers

9.1 [92]). In the previous section we showed that the microemulsion with composition TX100/B30/Decane in water has a constant size in the considered volume fractions. The distance between the droplets, assuming a primitive cubic packing, is defined as $d = \sqrt[3]{1\pi R_c^3/3\phi}$, where R_c is the radius of the core (R_c =4.8 nm) and ϕ_c the volume fraction of the core. The distance between the droplet surfaces is $d^* = d - 2R$, where the droplet radius is R = 6.02 nm. For instance, for a droplet volume fraction of ϕ_c =0.02, d^* =22 nm and for ϕ =0.1, d =5nm. This means that varying the droplet concentration, d can be varied so that it is larger than the end-to-end distance of the polymer $R_{ee} < d^*$, equal $R_{ee} = d^*$ or smaller than the polymer end-to-end distance.

7.2.1 Phase Behavior

Figure 7.4 shows the phase behavior for the addition of telechelic linear and star polymers with structure $(C_{12}PDMA)_2$, $(C_{12}PDMA)_3$ and $(C_{12}PDMA)_4$ with similar length (see Table 7.1). The phase diagrams show the number of C_{12} groups (Stickers) per droplet. The three systems present a different phase behavior. However they have common characteristics. In all the cases, there is a large monophasic region, which can be subdivided into two regions according to the rheological properties. At low values of r and ϕ, the solutions are low viscous and at larger values of r and ϕ the solutions are high viscous, i.e. they show a viscoelastic behavior. This two regions are separated by the percolation line (dotted line in Figure 7.4) and by a two phase region.

The phase separation is very slow. Rheological experiments of such systems (see Chapter 6), show that the relaxation time is related to the time for the change rearrangement between the droplets, is around 50 ms for the C_12 end-capped. In order to consider the

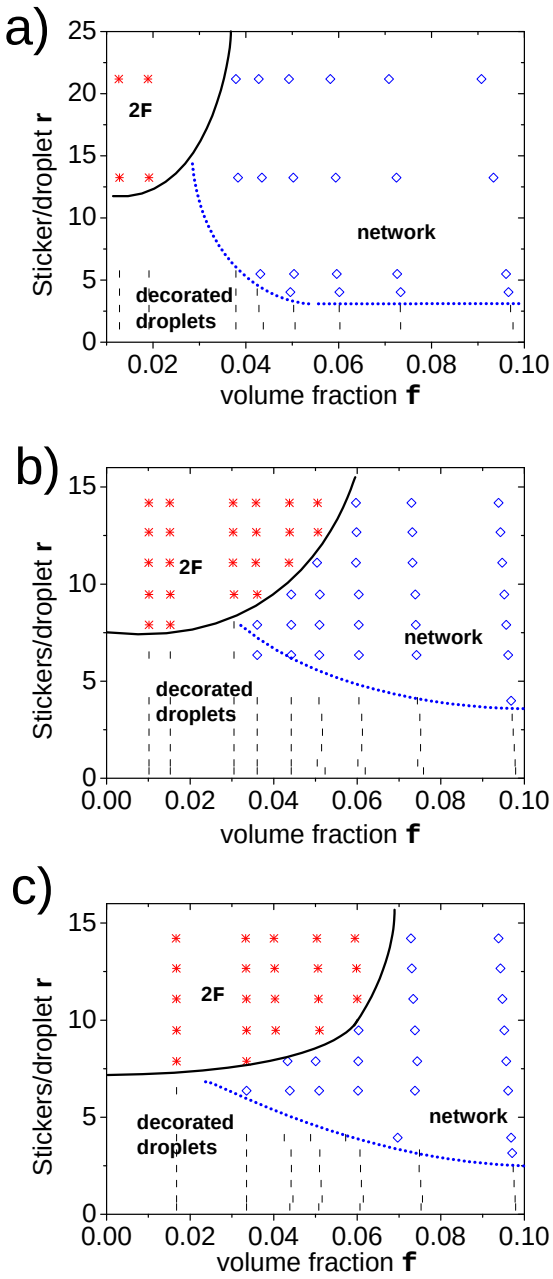

Figure 7.4: Phase behavior of the microemulsion upon addition of a)$(C_{12}PDMA)_2$ b)$(C_{12}PDMA)_3$ and c)$(C_{12}PDMA)_4$. The number of C_{12} groups are represented as a function of the hydrophobic core volume fraction. There are three regions: fluid(|), network ($\Diamond$), two phases($*$)

system to be in equilibrium, the time must be enough for the polymers to explore all different connectivity configurations. The phase separation took several days to take place and this time was longer when the samples were highly viscous.

When we compare the phase behavior of microemulsions with $(C_{12}PDMA)_2$, $(C_{12}PDMA)_3$ and $(C_{12}PDMA)_4$ added, we observe that the phase separation line when $\phi \to 0$ is at $r \sim 7.5$ regardless the architecture of the polymer. However the phase separation starts at higher

volume fraction with higher number of arms per polymer.

Moreover, we were interested in studying the dependence of the polymer molecular weight on the phase behavior. For this purpose we used a 3 arm polymer $(C_{12}PDMA)_3$ with a molecular weight 3 times larger than the previous one, and the phase diagram is depicted in Figure 7.5. The phase separation region is shifted to lower droplet volume fractions and higher r values.

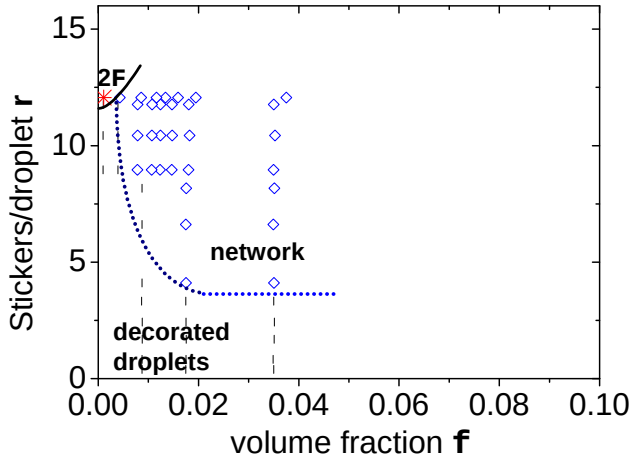

Figure 7.5: Phase behavior of the microemulsion upon addition of $(C_{12}PDMA)_3$ (M$\sim$ 90 KDa). The number of C_{12} groups are represented as a function of the hydrophobic core volume fraction.There are three regions: fluid(|), network (◊), two phases(*). Solid line: phase separation line. Dotted line: percolation line

Very similar systems with linear end-capped PEG show such a phase behavior [44,110]. Safran et al. proposed a theoretical model for the phase separation [41]. They suggest that the phase separation has a purely entropic origin and it occurs because the configurational entropy of the polymer in the dense network overcomes the loss of translational entropy of the droplets. The coexistence line in the plane (r,ϕ) is described by the equation

$$r = \frac{\phi + \frac{q_l}{q}\exp(-\epsilon)}{\phi(1-\phi)} \tag{7.2}$$

Here, ϕ is the droplet volume fraction, ϵ is the energy cost of forming a loop, q_l is the number of available positions for a sticker of size a $q_l \approx 4\pi R_0^2/(\pi a^2)$ and q the effective number of droplet pairs $q = \int dR(4\pi R^2/\pi R_0^2)\exp(-E_R/T)$. E_R is the energy of stretching a polymer to a length R having a radius of gyration R_G, $E_R \approx \frac{3}{2}R^2/R_G^2$. Above this line, the system becomes thermodynamically unstable and phase separates into a dense phase

of connected droplets and a fluid phase of decorated droplets.

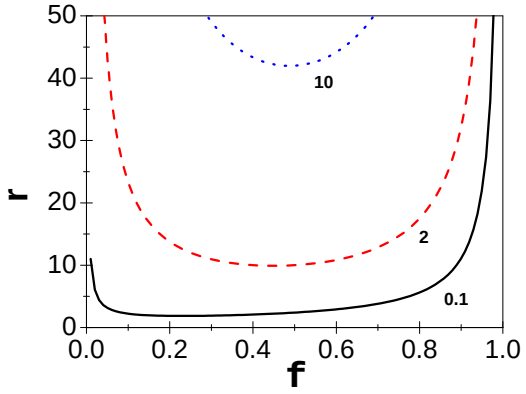

Figure 7.6: Phase diagram of microemulsion with telechelic polymer added. The lines are the spinodal lines of phase separation calculated with Eq. 7.2 for $q_l \exp(-\epsilon)/q = 0.1$, 2 and 10. Above this line, the system becomes thermodynamically unstable and phase separates into a dense phase of connected droplets and a fluid phase of decorated droplets.

The parameter ϵ is related to the loss of entropy of a polymer when both ends are in the same droplet. The number of configurations of a polymer with radius R_G that has both end constrained to a volume v, is proportional to $(v/R_G^3) \approx (R_0^2 l/R_G^3)$ where R_0 is the radius of the droplet and l the length of the sticker. Hence, the term $\exp(-\epsilon)$ can be approximated to $R_0^2 l/R_G^3$ when $R_0 < R_G$ and 1 when $R_0 > R_G$.

The controlling parameter is thus $q_l \exp(-\epsilon)/q$. As shown in Figure 7.6, the spinodal line of phase separation moves to higher values of r when $q_l \exp(-\epsilon)/q$ increases. This explained qualitatively the difference on the phase behavior due to a variation of the molecular weight.

7.2.2 Small Angle Neutron Scattering

In order to gain a further understanding of the microstructure, we performed SANS measurements for microemusion with composition TX100/B30/Decane in D_2O with increasing amounts of $(C_{12}PDMA)_2$, $(C_{12}PDMA)_3$ and $(C_{12}PDMA)_4$ added.

Figure 7.7 shows the scattering intensity as a function of the magnitude of the scattering vector q for microemusion at a constant volume fraction of 0.1 and increasing amounts of $(C_{12}PDMA)_2$, $(C_{12}PDMA)_3$ and $(C_{12}PDMA)_4$. We observe that in the three cases the unchanged position of the minimum at high q is the sign that the average size of the droplets is not influenced by the polymer. Thus, the addition of telechelic polymer to oil

in water droplets does not modify the structure or size of the droplets. This behavior is expected since all previous studies of microemulsions with end-capped polymers have shown that the droplet structure is not affected by the presence of the polymer [40, 43, 110]. The differences appear at smaller values of the scattering vector q. Upon addition of polymer, a correlation peak appears due to the interactions between the droplets as a consequence of the presence of the polymer.

We assume that the scattering is dominated by the scattering of the droplets.

The structure factor S(q) was derived by dividing the experimental scattering intensity $I(q)$ by the experimental form factor $nV^2\Delta\rho^2P(q)$ obtained in the previous section.

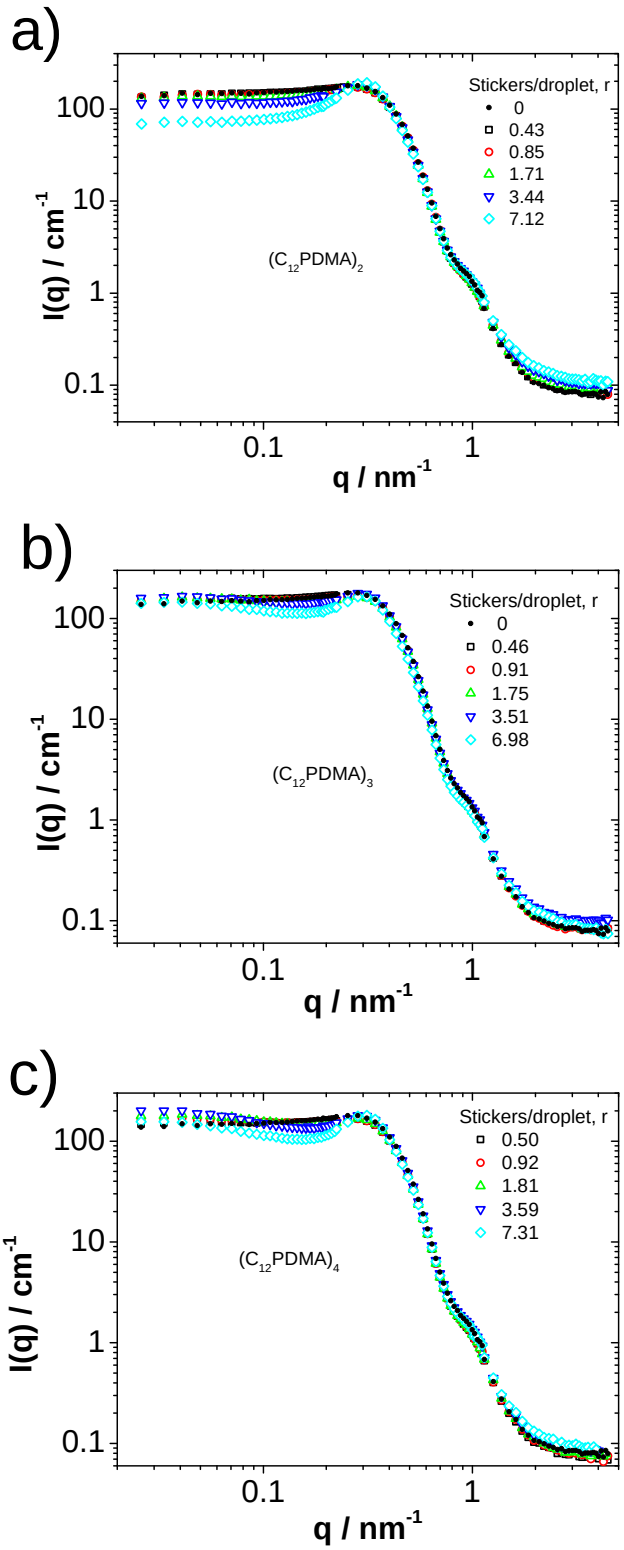

Figure 7.7: SANS patterns of the microemulsion with a core volume fraction $\phi_c = 0.67$ upon addition of a)$(C_{12}PDMA)_2$ b)$(C_{12}PDMA)_3$ and c)$(C_{12}PDMA)_4$

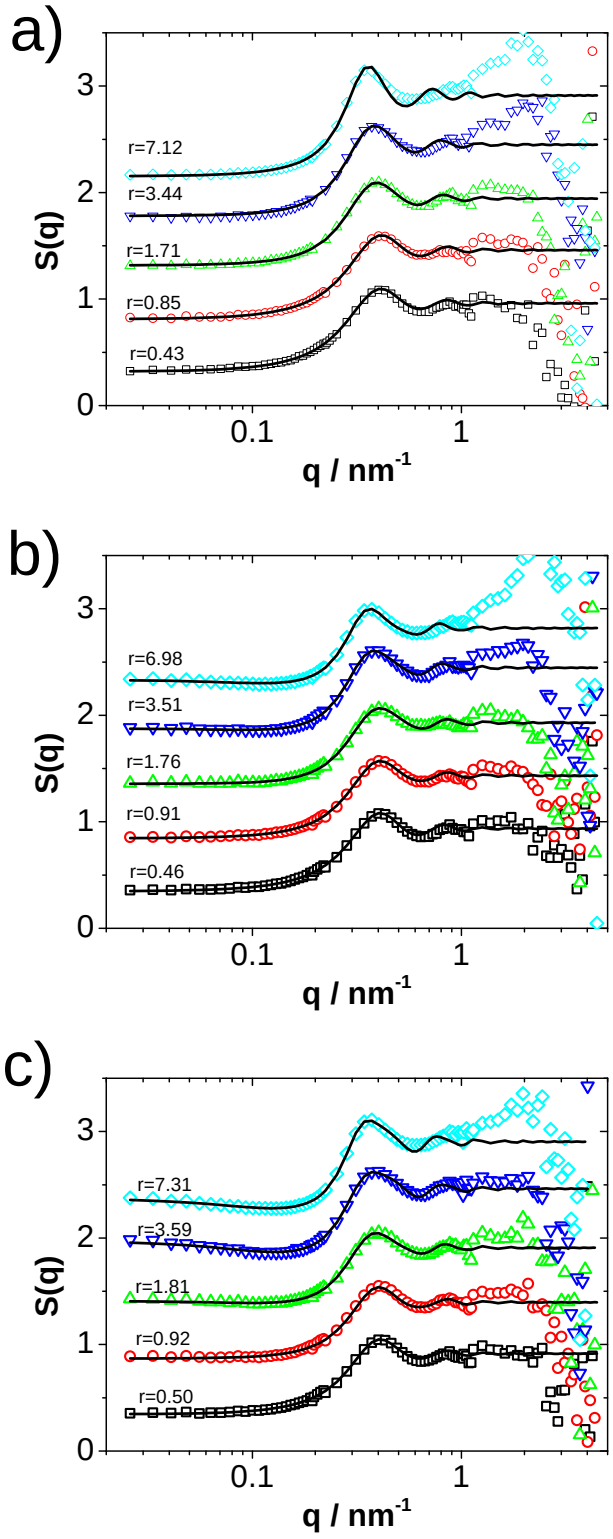

Figure 7.8: Structure factor S(q) with a core volume fraction $\phi_c = 0.67$ upon addition of a)$(C_{12}PDMA)_2$ b)$(C_{12}PDMA)_3$ and c)$(C_{12}PDMA)_4$. The number of stickers per droplet r is indicated. The curves are shifted vertically for a better view. The lines correspond to the fit with a square well potential structure factor.

The structure factor experimental data were analyzed with a a model based on the interaction potential of hard spheres with a square well attractive potential:

$$\frac{U(r)}{k_B T} = \begin{cases} \infty & \text{for} \quad 0 < r < \sigma \\ -\epsilon & \text{for} \quad \sigma < r < \lambda\sigma \\ 0 & \text{for} \quad r > \lambda\sigma \end{cases} \tag{7.3}$$

where the hard-sphere particle diameter is $\sigma = 2R_{HS}$, λ the well width, and ϵ the well depth. The Ornstein-Zernike equation in the Percus-Yevick (PY) approximation [68] for this square-well potential can be solved analytically to the first order in a series expansion for small λ, and the result for S(q) can be expressed as a function of the four parameters R_{HS},ϵ, λ, and particle volume fraction [132].

	$(C_{12}PDMA)_2$				$(C_{12}PDMA)_3$				$(C_{12}PDMA)_4$			
r	R_{HS}	ϕ_{HS}	ϵ	λ	R_{HS}	ϕ_{HS}	ϵ	λ	R_{HS}	ϕ_{HS}	ϵ	λ
0.45	7.26	0.140	0.010	1.90	7.30	0.133	0.024	1.91	7.23	0.134	0.053	1.64
0.9	7.236	0.145	0.012	1.90	7.21	0.138	0.051	1.73	7.26	0.133	0.101	1.66
1.8	7.52	0.152	0.043	1.87	7.17	0.142	0.067	1.87	7.32	0.139	0.121	1.86
3.5	7.75	0.172	0.051	1.91	7.54	0.153	0.114	1.88	7.43	0.158	0.162	1.97
7	8.63	0.232	0.035	2.00	7.82	0.166	0.179	1.81	7.90	0.189	0.204	1.91

Table 7.2: Square Well parameters from fits of S(q) of microemulsion with a core volume fraction $\phi_c = 0.67$ with increasing amounts of $(C_{12}PDMA)_2$,$(C_{12}PDMA)_3$ and $(C_{12}PDMA)_4$. Listed are the number of stickers (C_{12} groups) per droplet r, the hard sphere radius R_{HS}, the hard sphere volume fraction ϕ_{HS}, the depth of the potential ϵ and the relative width λ.

The results of fitting the experimental structure factor with the square well potential are collected in Table 7.2. One observes that the relative width of the well λ (see Eq. 7.3) is large and does not vary with r or the type of polymer. The depth of the potential ϵ increases with r and with the number of end-capped arms per polymer.

7.3 Conclusions

We presented the admixing of linear and star end-capped polymers to an oil in water microemulsion of TX100/Brij 30/decane/water with a radius of 6 nm so that the length of the polymers was near to or smaller than the interdroplet distance, depending on the droplet concentration. In general, the microemulsion polymer mixtures exhibit a phase behavior

as expected for such systems where for the case that the polymer end-to-end distance is smaller than the interdroplet distance, for high polymer concentrations the configurational entropy of the polymer overcomes the entropy gain due to phase separation. The phase separation line is shifted to lower number of stickers per droplet and higher droplet volume fractions by increasing the number of arms. In addition, SANS measurements show that the polymers with larger number of arms induce a larger attractive interaction between the droplets, where in particular a substantial enhancement takes place when changing from the 2-arm to the 3-arm polymer. This result is in good agreement with the phase behavior, where the shift of the phase boundary correlates directly with the attractive interaction observed in the SANS experiments.

Chapter 8

Conclusion and Outlook

This thesis presents a comprehensive study of hydrophobically modified linear and star polymers in aqueous solution and in microemulsion mainly by means of light scattering, small-angle neutron scattering (SANS), and rheology. The aim of this study was to elucidate the effect that the architecture of the polymers has on the aggregation behavior, especially on the structure and the dynamic properties of the polymers in water and in microemulsion and how that allows to control the rheological properties.

For this purpose I employed tailor made hydrophobically modified linear and star polymers based on hydrophilic poly(N,N-dimethylacrylamide) (PDMA) blocks with n units, that have 2, 3 or 4 end-capped arms, with an aliphatic end chain of 4, 12 or 18 carbon units.

First, I presented a SANS study of the polymers in a good, non-selective solvent with different polymer concentrations. This allowed the determination of the molecular weight, the radius of gyration and the second virial coefficient of the pure polymers. The radius of gyration increases proportional to the square root of the molecular weight, irrespective of the polymeric architecture. The knowledge of the length of the hydrophilic chains is of crucial importance in order to elucidate the structural and dynamical properties of its aqueous solutions and mixtures with microemulsions described in the following chapters.

The aggregation behavior of the polymers in aqueous solution was studied by means of SANS, DLS and rheology. The C_4 end-capped polymers behave different to the C_{12} end-capped polymers. While the first do not aggregate in aqueous solutions, the C_{12} end-capped polymers have an aggregation behavior that strongly depends on the number of hydrophobically modified arms. The C_{12} end-capped polymers aggregate into flower-like

micelles. The aggregation number of the polymers per micelle decreases with the number of end-capped arms in the polymer because the aggregation number of hydrophobes per micelle is kept constant, as predicted by the theory. However, the connectivity between the micelles increases considerably with the number of arms. This is reflected in the formation of bigger clusters and, thus, higher viscosities at low polymer concentrations and a higher elastic modulus in the formed polymer networks at higher concentrations.

In Chapter 5 I present a a comprehensive study of the structure and dynamics of a model system of a mixture of telechelic polymer and microemulsion based on a commercially available telechelic polymer (Rewopal 6000DS) with an oil-in-water (O/W) microemulsion composed of tetradecyl dimethyl amine oxide (TDMAO) and decane with droplets of a radius of 2.7 nm. We show that along the percolation line there is a transition from polymer-decorated droplets to a microemulsion network. SANS and DLS show that the droplet size is not affected by the presence of the polymer. The interaction is mainly attractive when the number of polymers per droplet is low and when the network if formed this attraction is compensated by a repulsion created by the volume occupied by bridging hydrated PDMA that resist interpenetration. Rheology measurements show that the samples exhibit a viscoelastic behavior, where the elasticity, as well as the viscosity can be very well described by a percolation behavior. The concentration fluctuations measured by DLS are characterized by two relaxation modes. The first is the collective diffusion of the droplets and the second is related to the structural relaxation process obtained from rheology.

In Chapter 6 I investigated the addition of the different 2-, 3-, and 4-arm end-capped polymers to the same O/W TDMAO/decane/water microemulsion where the end-to-end distance of the polymers was larger than the interdroplet distance $R_{ee} > d$. When added to O/W-ME, they form networks, thus markedly increasing the viscosity by several orders of magnitude and leading to systems of pronounced elastic properties. The length of the hydrophobic sticker has a strong impact on the viscosity and the dynamics of the system and controls the residence time in an aggregate .The residence time scales exponentially with the length of the hydrocarbon chain of the sticker and correspondingly the viscosity. While SANS shows that the static structure of these systems is retained upon polymer addition, in DLS in contrast, increasingly complex relaxation patterns with up to three relaxation modes are observed. Especially the appearance of a non-diffusive relaxation

mode becomes increasingly more pronounced with increasing number of arms and polymer concentration. The complex DLS behavior correlates well with the rheological behavior of the formed microemulsion networks and can be explained consistently with a network model of interconnected microemulsion droplets. We show that polymers with more end-capped chains form more effectively networks than the linear polymer.

In Chapter 7 I study the effect of admixing linear and star end-capped polymers to an oil in water microemulsion of TX100/Brij 30 and decane with a larger size (R =6 nm) so that the length of the polymers was smaller than the interdroplet distance, i.e. $R_{ee} < d$. The microemulsion polymer mixtures exhibit a phase behavior as expected for such systems. The entropically driven phase separation line is shifted to lower number of stickers per droplet and higher droplet volume fractions by increasing the number of arms. In addition, SANS measurements show that the polymers with larger number of arms induce a larger attractive interaction between the droplets, where in particular a substantial enhancement takes place when changing from the 2-arm to the 3-arm polymer. This is consistent with the phase behavior, where the shift of the phase boundary correlates directly with the attractive interaction observed in the SANS experiments.

In summary, I have studied telechelic polymers of different number of arms with respect to their ability to bridge microemulsion droplets and thereby control their rheological behavior and dynamics. This has been done for situations where the length of the bridging polymer is larger or smaller than the average distance between the O/W droplets. For all cases it is shown that the viscosity depends mostly on the sticker length of the alkyl chain that controls the residence time in the oil droplets. In contrast, the elastic modulus is clearly correlated to the number of arms. The effectiveness of the networks formed increases with the connectivity given by the number of bridging arms. This shows that the architecture of bridging polymers is a valuable means to control the dynamic and rheological properties of self-assembling systems.

Future work in that field might then be directed to generalize these findings to polymers containing still larger number of arms, i.e., to go to real star-like end-capped systems. Another direction of interest would be to go to systems where the extent of bridging, which is controlled by the number of arms and the length of the hydrophilic bridging polymer block, may be controlled by external parameters such as pH, ionic strength, light, etc.. Such functional rheological modifier then would combine very variable network forming

properties, which the possibility to switch them on or off. Such smart modifiers with well-controlled rheological controlling ability then would certainly be of high interest for a large number of potential applications.

List of Abbreviations

O/W	oil-in-water
W/O	water-in-oil
EO	ethylene oxide
PEO	poly (ethylene oxide)
AP	associative polymer
PDMA	poly (N,N-dimethylacrylamide)
HM	hydrophobically modified
TDMAO	tetradecyldimethyl amine oxide
TX100	Triton® X100
B30	Brij® 30
nd	not determined
SANS	Small Angle Neutron Scattering
DLS	Dynamic Light Scattering
FCS	Fluorescence Correlation Spectroscopy
C_n	alkyl chain with n carbon atoms

List of Symbols

F	free energy
γ	interfacial tension
p	packing parameter
v_s	surfactant chain volume
a_s	surfactant head group area
l_s	surfactant chain length
d	inter-droplet distance
d^*	surface-to-surface distance
n	number density
R	droplet radius
ϕ	volume fraction
R_{ee}	end-to-end distance of a polymer chain
N	number of monomers of a molomer chain
l	length of a monomer
c	concentration
cmc	critical micellar concentration
f	number of end-capped arms
k_B	Boltzmann constant
T	absolute temperature
q	scattering vector
$I(q)$	scattering intensity
$S(q)$	structure factor
$P(q)$	form factor
ρ	scattering length density

M_w	weight average molar mass
M_n	number average molar mass
PDI	polydispersity index
r	stickers per droplet
R_G	radius of gyration
R_{HS}	hard sphere radius
ϕ_{HS}	hard sphere volume fraction
η	dynamic viscosity
G'	elastic modulus
G''	viscous modulus
G_0	plateau modulus
D	diffusion coefficient
R_H	hydrodynamic radius

Appendix A

Appendix to Chapter 3

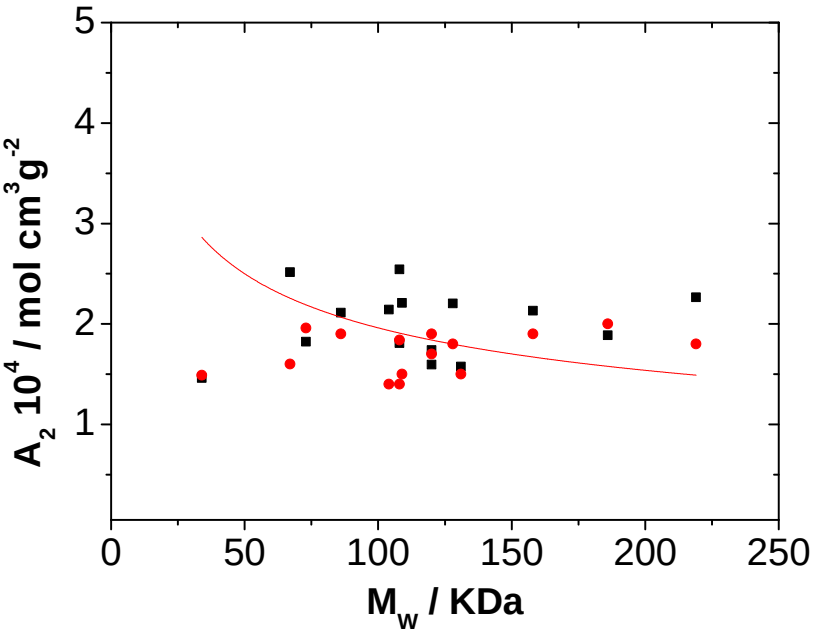

Figure A.1: Second virial coefficient as a function of the molecular weight as obtained via Zimm plot (Eq. 3.1) (squares) and from the concentration dependence of the radius of gyration (Eq. 3.3) (circles) from the SANS data of polymer solutions of concentrations between 1 and 3.5 g/ml in d_8-THF.

Appendix B

Appendix to Chapter 5

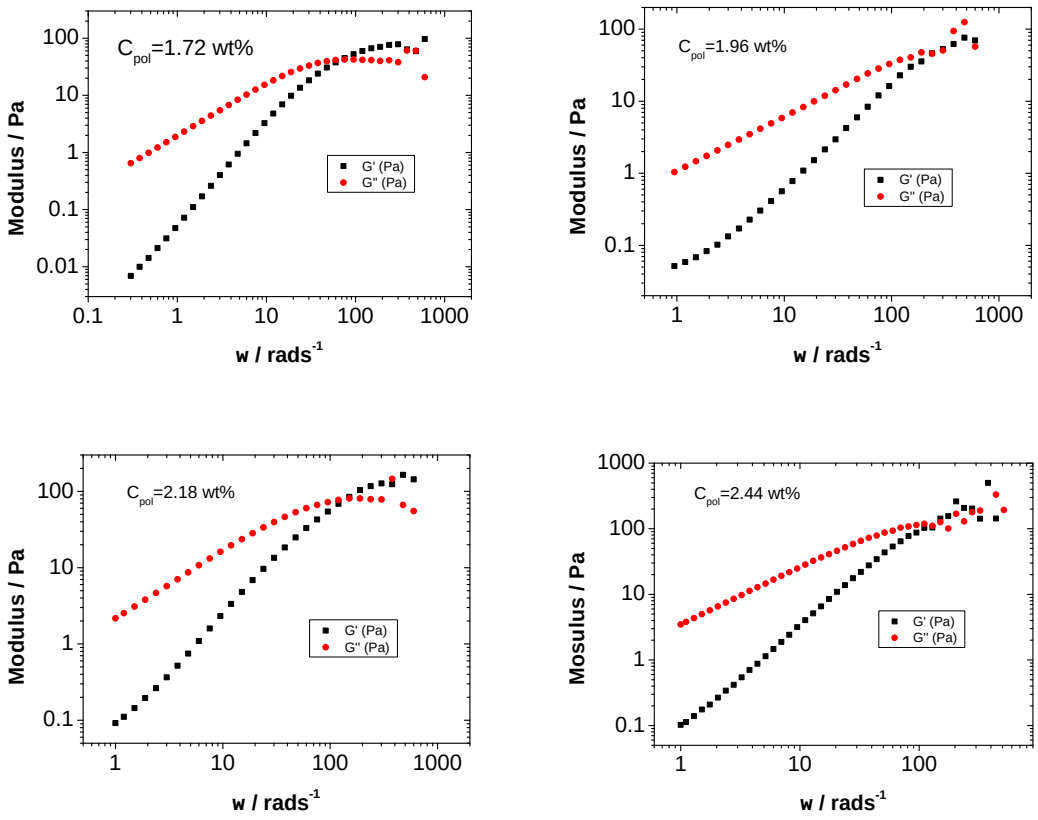

Figure B.1: Storage G' and loss G'' moduli as a function of the angular frequency for microemulsion with different concentrations of C_{18}-EO_{18}-C_{18} added c_p(the concentration is indicated in each plot) measured at a temperature of 25°C with the instrument Ares AG2

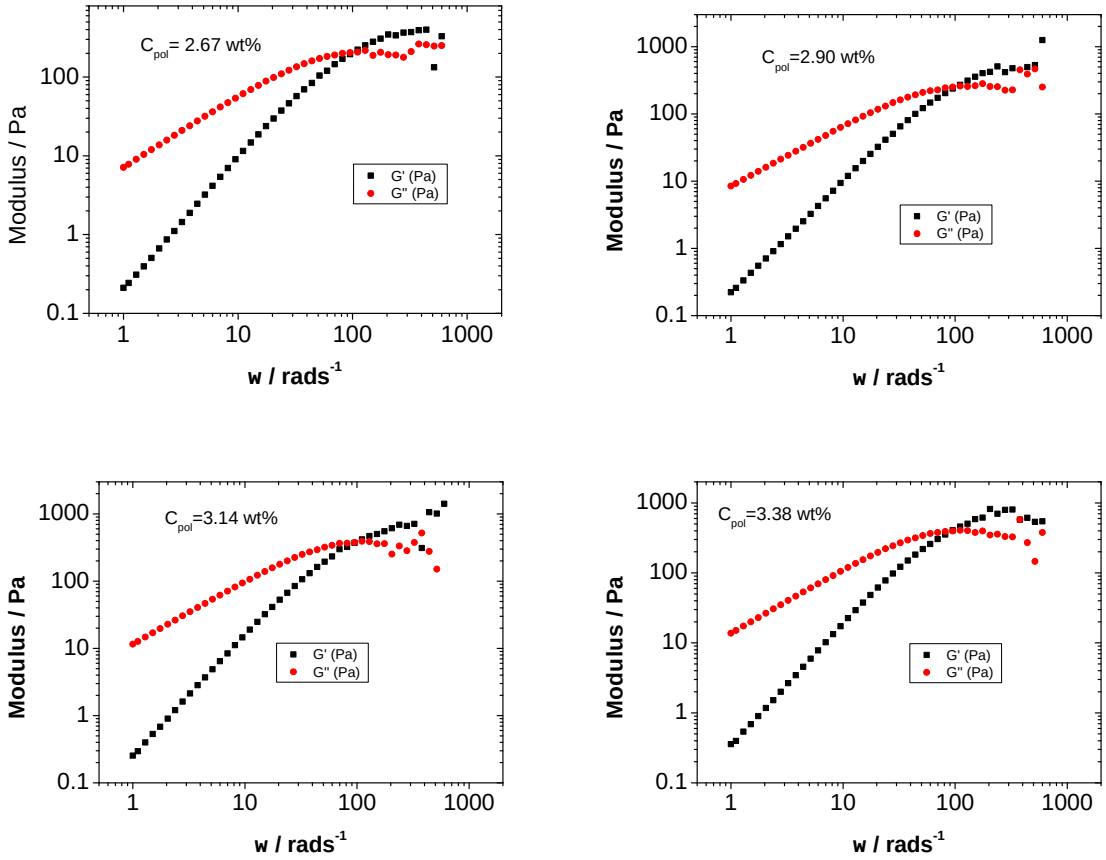

Figure B.2: Storage G' and loss G'' moduli as a function of the angular frequency for microemulsion with different concentrations of C_{18}-EO_{18}-C_{18} added c_p(the concentration is indicated in each plot) measured at a temperature of 25°C with the instrument Ares AG2

Appendix C

Appendix to Chapter 6

C.1 Small Angle Neutron Scattering (SANS)

C.1.1 Scattering length density

Table S1 contains the scattering length densities of all the components present in the mixture.

The scattering length density contrast $\Delta\rho$ of the sample can be calculated as the difference of the scattering length density of the aggregates ρ_{agg}, and the mean scattering length density of the sample $\bar{\rho}$

$$\Delta\rho = \rho_{agg} - \bar{\rho} \tag{C.1}$$

We consider the microemulsion droplets to be homogeneous spheres and, therefore, their scattering length density is the mole pondered averege of the scattering length density of decane and TDMAO (see Table C.1)

$$\rho_{agg} = n_{decane}\rho_{decane} + n_{TDMAO}\rho_{TDMAO} \tag{C.2}$$

Molecule	Structure	$M_W/gmol^{-1}$	ρ/gml^{-1}	$\rho_{SLD}/10^{10}cm^{-2}$
D_2O	D_2O	20	1.1056	6.36
Decane	$C_{10}H_{22}$	142.29	0.73	-0.488
TDMAO	$C_{16}H_{35}NO$	257.46	1	-0.23
PDMA	[a]	[a]	1.05	0.931

Table C.1: Scattering length densities of all the components present in the mixture. For the polymer [a] see Table 1

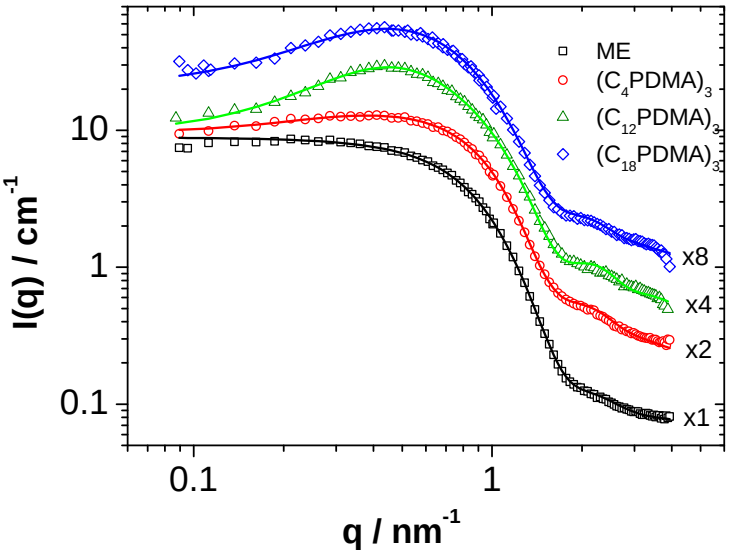

Figure C.1: SANS patterns of the aggregates of microemulsion (squares) and with $(C_4PDMA)_3$ (circles), $(C_{12}PDMA)_3$ (triangles) and $(C_{18}PDMA)_3$ (diamonds) at a concentration of 5 wt% added polymer in D_2O at room temperature. The lines correspond to the fits with Eq. 3. The curves have been vertically shiffted by the factor indicated for a better view.

where n_i is the mole average fraction of the component i in the aggregate. The average scattering length density of the sample is given by

$$\bar{\rho} = \chi_{decane}\rho_{decane} + \chi_{TDMAO}\rho_{TDMAO} + \chi_{PDMA}\rho_{PDMA} + \chi_{D_2O}\rho_{D_2O} \tag{C.3}$$

where χ_i is the mole average fraction of the component i in the sample.

C.1.2 Error estimate of the fitted parameters

The analytical model is fitted to the experimental data minimizing

$$(N_{exp} - 1)^{-1} \sum_{k=1}^{N} \left(\left[I^{th}(q_k) - I(q_k) \right] / \Delta I(q_k) \right)^2 \tag{C.4}$$

where N_{exp} is the number of points, q_k the different q-values of the points, I^{th}, I and ΔI the model intensity, experimental intensity and experimental error.

The errors on fitted parameters can be estimated from the Hessian matrix, which is calculated within the "outer product approximation" as $J^T J$ where J is the Jacobian matrix

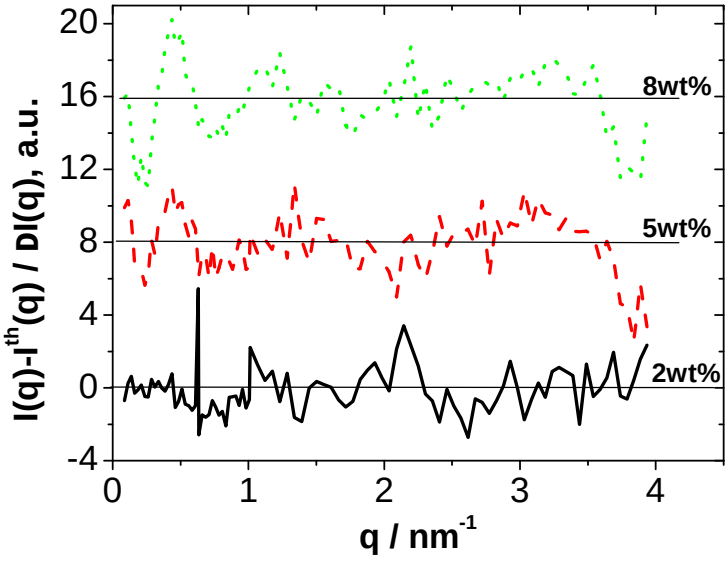

Figure C.2: Fit residuals of the SANS patterns of microemulsion with different content of added $(C_{12}PDMA)_3$.

(first derivative of the individual error).

The estimated uncertainty of the fitted parameters is indicated in Table 2.

Figure C.2 shows exemplariy the fit residuals SANS patterns of microemulsion with different content of added $(C_{12}PDMA)_3$.

C.1.3 Polymer scattering contribution

The forward scattering of the polymer contribution is proportional to the polymer content (see Fig C.3).

From the forward scattering, an effective molecular weight of the polymer segments may be calculated with the following equation:

$$M_W = \frac{d^2 N_{AV} \alpha}{\Delta\rho^2 c_{pol}} \tag{C.5}$$

c_{pol}	M_W / gmol−1
0.02	4059
0.05	3694
0.08	3323

Table C.2: Effective molecular weight of the polymer segments

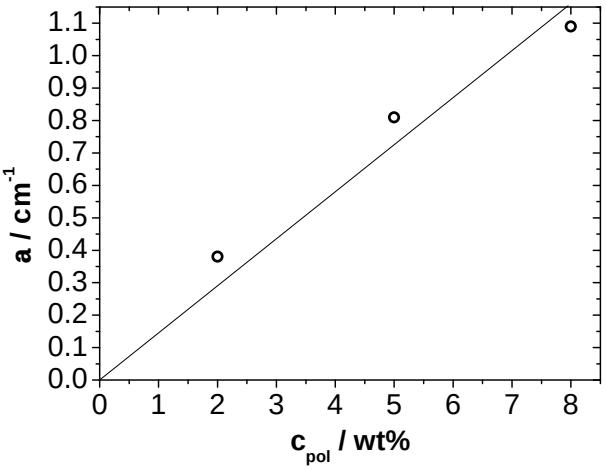

Figure C.3: Prefactor α of Eq. 6 as a function of the $(C_{12}PDMA)_3$ polymer concentration.

C.2 Dynamic Light Scattering (DLS)

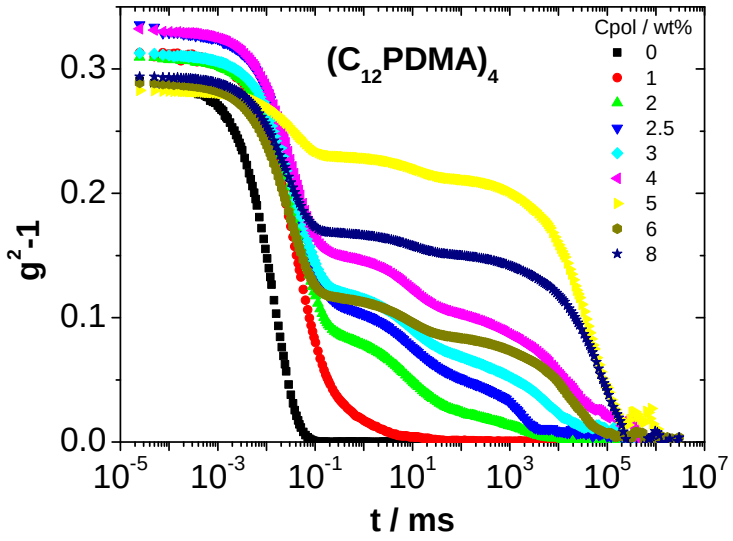

Figure C.4: Intensity autocorrelation function $g^{(2)}(t) - 1$ as a function of time for $(C_{12}PDMA)_4$ for various concentrations of polymer added to the O/W microemulsion (data taken at a scattering angle of 90° and a temperature of 25°C).

Polymer	C/ wt%	r	η_0/Pas	G_0/Pa	τ_R/ms	D_{eff}/m^2s^{-1}	$<\tau_2>/ms$	β_2
$(C_4PDMA)_3$	5	0.76	$2.95{\cdot}10^{-3}$			$5.78\cdot10^{-11}$	1.02	0.66
$(C_{12}PDMA)_3$	5	2.5	17.1	1608	11.1	$7.40\cdot10^{-11}$	64.7	0.31
$(C_{18}PDMA)_3$	5	1.6	$3.09\cdot10^3$	1129	$2.73{\cdot}10^3$	$6.60\cdot10^{-11}$	$4.36{\cdot}10^3$	0.68

Table C.3: Rheological parameters for different sticker lengths obtained from the fit with Eqs. 6.9 and 6.10: plateau modulus G_0, relaxation time τ_R and zero shear viscosity. As the sample with $(C_4PDMA)_3$ was too fluid to be measured with the Gemini rheometer, the viscosity was measured with a capillary viscometer. In addition, effective diffusion coefficient D_{eff}, mean value of the second relaxation time $<\tau_2>$, and stretching parameter β_2 as obtained from DLS.

C/ wt%	r	G_0/Pa	τ_R/ms	D_{eff}/m^2s^{-1}	$<\tau_2>/ms$	β_2 (DLS)	$<\tau_3>/s$	β_3(DlS)
0	0			$8.76\cdot10^{-11}$				
0.50	0.19			$6.52\cdot10^{-11}$				
1.00	0.38			$6.23\cdot10^{-11}$	66.9	0.62		
3.26	1.23	104	5.1	$7.38\cdot10^{-11}$	18.1	0.67	13.8	0.39
3.55	1.34	165	6.8	-				
4.50	1.70	330	8.1	-				
5.00	1.89	452	10.0	$7.11\cdot10^{-11}$	14.7	0.33	24.1	0.95
5.98	2.27	692	9.5	$7.56\cdot10^{-11}$	40.1	0.32	19.2	1.00
7.97	3.03	992	14.5	$9.01\cdot10^{-11}$	24.5	0.35	46.3	0.89

Table C.4: Dynamic parameters of $(C_{12}PDMA)_2$: Concentration C, number of stickers per droplet r and the parameters obtained from the fit with Eqs. 10 and 11: plateau modulus G_0, relaxation time τ_R; and Eq. 18 effective diffusion coefficient D_{eff}, mean value of the second relaxation time $<\tau_2>$, mean value of the stretching parameter β_2

C/ wt%	r	G_0/Pa	τ_R/ms	D_{eff}/m^2s^{-1}	$<\tau_2>/ms$	β_2(DLS)	$<\tau_3>/s$	β_3(DLS)
0	0			$8.76\cdot10^{-11}$				
0.17	0.08			$8.60{\cdot}10^{-11}$				
0.50	0.25			$7.77{\cdot}10^{-11}$				
0.75	0.37			$5.44{\cdot}10^{-11}$				
1.99	1.00	40	5.1	$5.14{\cdot}10^{-11}$	2.3	0.47	0.87	0.42
2.98	1.50	147	5.4	$6.09{\cdot}10^{-11}$	8.7	0.55	15.6	0.55
3.99	2.00	448	8.3	$6.67{\cdot}10^{-11}$	14.8	0.43	20.0	0.88
5.05	2.54	1120	11.1	$7.48{\cdot}10^{-11}$	7.9	0.85	204.8	0.44
5.95	2.99	2065		$7.45{\cdot}10^{-11}$	8.65	0.78	148.8	0.40
7.92	3.98	2703	17.5	$8.52{\cdot}10^{-11}$	9.18	0.87	182.42	0.60

Table C.5: Dynamic parameters of $(C_{12}PDMA)_3$: Concentration C, number of stickers per droplet r and the parameters obtained from the fit with Eqs. 10 and 11: plateau modulus G_0, relaxation time τ_R; and Eq. 18 effective diffusion coefficient D_{eff}, mean value of the second relaxation time $<\tau_2>$, mean value of the stretching parameter β_2

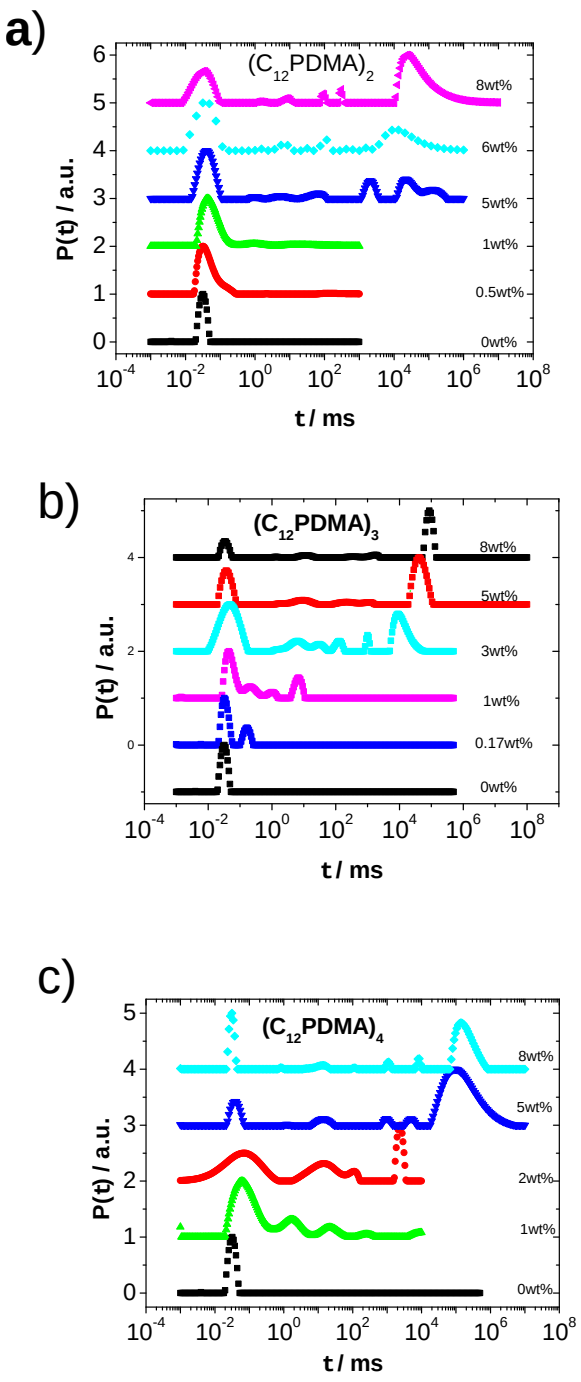

Figure C.5: Decay time distribution function for different concentrations of $(C_{12}PDMA)_3$ added to microemulsion samples containing 100 mM TMDAO / 35 mM decane

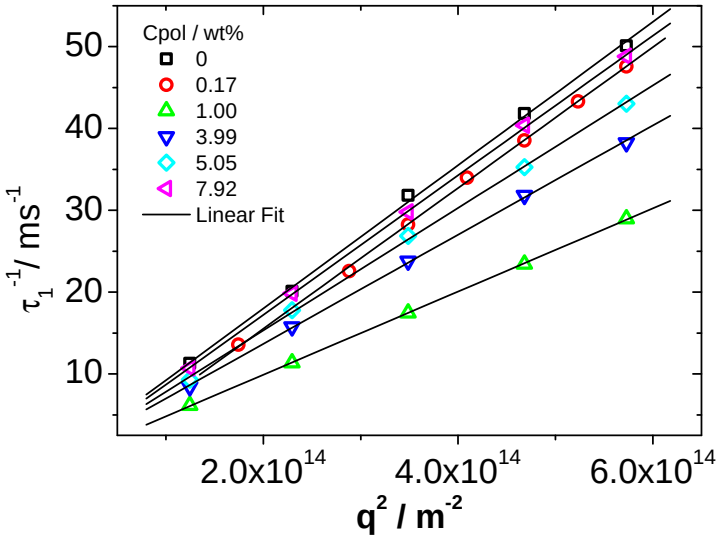

Figure C.6: Inverse of the fast relaxation time τ_1 as a function of q^2 for different concentrations of $(C_{12}PDMA)_3$ added to microemulsion samples containing 100 mM TMDAO / 35 mM decane. The lines are linear fits using Eq. 17.

C/ wt%	r	G_0/Pa	τ_R/ms	D_{eff}/m^2s^{-1}	$<\tau_2>/ms$	β_2 (DLS)	$<\tau_3>/s$	β_3(DLS)
0	0			$8.76 \cdot 10^{-11}$				
1.02	0.48	-		$4.49 \cdot 10^{-11}$	1.59	0.64		
2.00	0.95	216	2.5	$4.79 \cdot 10^{-11}$	18.2	0.49		
2.44	1.16	315	4.4	$5.22 \cdot 10^{-11}$	13.6	0.63	1.94	0.71
3.00	1.42	526	7.0	$5.81 \cdot 10^{-11}$	11.3	0.61	1.83	0.73
3.99	1.90	1320	9.0	$6.47 \cdot 10^{-11}$	10.3	0.83	20.3	0.70
5.00	2.38	1368	12.2	$7.62 \cdot 10^{-11}$	12.1	0.85	133.6	0.79
6.03	2.87	1426	7.8	$7.52 \cdot 10^{-11}$	11.6	0.73	89.2	0.64
7.89	3.76	2272	22.6	$9.45 \cdot 10^{-11}$	15.1	0.67	343.8	0.65

Table C.6: Dynamic parameters of $(C_{12}PDMA)_4$: Concentration C, number of stickers per droplet r and the parameters obtained from the fit with Eqs. 10 and 11: plateau modulus G_0, relaxation time τ_R; and Eq. 18 effective diffusion coefficient D_{eff}, mean value of the second relaxation time $<\tau_2>$, mean value of the stretching parameter β_2

Appendix D

Appendix to Chapter 7

Scattering length density contrast and hydration of the shell

The microemulsion droplet of the system TX100 / B30/ decane/D_2O consists of a hydrophobic core and a EO shell. Since the EO shell will be strongly hydrated with D_2O, the scattering length density of the core and the shell will be different, so that a model for a core-shell was used.

The scattering length density of the core results of a volume fraction pondered average of the scattering length densities of all the components, resulting in a value of -0.3 10^{10} cm^{-2}. The same way, the scattering length density of the dry shell can be calculated to be 0.965 10^{10} cm^{-2}.

In order to determine the scattering length density, we need to first determine the hydration h of the shell. This can be done with the scattering invariant, defined as

$$\tilde{Q} = 2\pi^2 \Delta\rho^2 \tag{D.1}$$

$\Delta\rho^2$ in a three phase system (core (c), shell (s), solvent (1)) is defined as

$$\Delta\rho^2 = \phi_c\phi_1(\rho_c - \rho_1)^2 + \phi_s\phi_1(\rho_s - \rho_1)^2 + \phi_c\phi_s(\rho_c - \rho_s)^2 \tag{D.2}$$

The scattering length density of the shell is

$$\rho_s = \rho_s(dry)(1 - h) + h\rho_1 \tag{D.3}$$

ϕ	I_{inc} (cm^{-1})	$\Delta\rho_{core}$ ($10^{10}cm^{-2}$)	$\Delta\rho_{shell}$ ($10^{10}cm^{-2}$)	ϕ_c	R_{core} (nm)	σ	t_{shell} (nm)	R_{HS} (nm)	ϕ_{HS}
0.005	0.021	6.68	1.97	0.0041	4.76	0.190	1.19	7.20	0.002
0.010	0.014	6.68	1.97	0.0080	4.81	0.187	1.19	7.20	0.008
0.025	0.028	6.68	1.97	0.0203	4.85	0.190	1.19	7.28	0.031
0.037	0.043	6.68	1.97	0.0315	4.89	0.195	1.19	7.25	0.049
0.050	0.053	6.68	1.97	0.0432	4.87	0.197	1.19	7.22	0.069
0.100	0.076	6.68	1.97	0.0928	4.83	0.190	1.19	7.26	0.141

Table D.1: Structural parameters. Droplet volume fraction ϕ, incoherent scattering background I_{inc}, scattering length density contrast of the core $\Delta\rho_{core}$ and the shell $\Delta\rho_{shell}$, volume fraction of the core ϕ_c, radius of the core R_{core}, standard deviation of the core size σ, thickness of the shell t_{shell}, hard sphere radius R_{HS}, hard sphere volume fraction ϕ_{HS}.

The volume fractions are:

$$\phi_c = 0.67\phi$$

$$\phi_s = 0.33\phi(1+h)$$

$$\phi_1 = 1 - h - \phi$$

Substituting Eqs. D.2 and D.3 in Eq D.1 and from the droplet concentration ϕ dependence of the experimental invariant, a hydration of the shell of 60% was obtained. The scattering length density difference of the core and the shell with the solvent are listed in Table D.1.

Bibliography

[1] T.P. Hoar and J.H. Schulman. Transparent water-in-oil dispersions: the oleophatic hydro-micelle. *Nature*, 152:102–103, 1943.

[2] M. Kahlweit and R. Strey. Phase-behavior of ternary-systems of the type h2o-oil-nonionic amphiphile (microemulsions). *Angewandte Chemie-international Edition In English*, 24(8):654–668, 1985.

[3] D. Langevin. Micelles and microemulsions. *Annual Review of Physical Chemistry*, 43:341–369, 1992.

[4] M. Gradzielski, D. Langevin, T. Sottmann, and R. Strey. Small angle neutron scattering near the wetting transition: Discrimination of microemulsions from weakly structured mixtures. *Journal of Chemical Physics*, 104(10):3782–3787, March 1996.

[5] P. G. de Gennes and C. Taupin. Microemulsions and the flexibility of oil/water interfaces. *Journal of Physical Chemistry*, 86(13):2294–2304, June 1982.

[6] M. Gradzielski, D. Langevin, and B. Farago. Experimental investigation of the structure of nonionic microemulsions and their relation to the bending elasticity of the amphiphilic film. *Physical Review E*, 53(4):3900–3919, April 1996.

[7] Mitchell D.J. Israelachvili, J.N. and B.W. Ninham. Theory of self-assembly of hydrocarbon amphiphiles into micelles and bilayers. *Journal of the Chemical Society, Faraday Transactions 2*, 72:1525, 1976.

[8] Per Gunnar Nilsson and Bjoern Lindman. Water self-diffusion in nonionic surfactant solutions. hydration and obstruction effects. *Journal of Physical Chemistry*, 87(23):4756–4761, November 1983.

[9] B.H. Robinson. Colloid chemistry: Applications of microemulsions. *Nature*, 320(6060):309–309, March 1986.

[10] B. K. Paul and S. P. Moulik. Uses and applications of microemulsions. *Current Science*, 80(8):990–1001, April 2001.

[11] Christophe Chassenieux, Taco Nicolai, and Lazhar Benyahia. Rheology of associative polymer solutions. *Current Opinion in Colloid & Interface Science*, 16(1):18–26, February 2011.

[12] C. Tsitsilianis. Responsive reversible hydrogels from associative "smart" macromolecules. *Soft Matter*, 6(11):2372–2388, 2010.

[13] Y. Serero, R. Aznar, G. Porte, J. F. Berret, D. Calvet, A. Collet, and M. Viguier. Associating polymers: From "flowers" to transient networks. *Physical Review Letters*, 81(25):5584–5587, December 1998.

[14] P. C. Shanks and E. I. Franses. Estimation of micellization parameters of aqueous sodium dodecyl sulfate from conductivity data. *Journal of Physical Chemistry*, 96(4):1794–1805, February 1992.

[15] E. Alami, M. Almgren, W. Brown, and J. Francois. Aggregation of hydrophobically end-capped poly(ethylene oxide) in aqueous solutions. fluorescence and light-scattering studies. *Macromolecules*, 29(6):2229–2243, March 1996.

[16] Q. T. Pham, W. B. Russel, J. C. Thibeault, and W. Lau. Micellar solutions of associative triblock copolymers: Entropic attraction and gas-liquid transition. *Macromolecules*, 32(9):2996–3005, April 1999.

[17] A. Yekta, J. Duhamel, H. Adiwidjaja, P. Brochard, and M. A. Winnik. Association structure of telechelic associative thickeners in water. *Langmuir*, 9(4):881–883, April 1993.

[18] Xiao-Xia Meng and William B. Russel. Structure and size of spherical micelles of telechelic polymers. *Macromolecules*, 38(2):593–600, December 2004.

[19] Fabrice Laflèche, Dominique Durand, and Taco Nicolai. Association of adhesive spheres formed by hydrophobically end-capped peo. 1. influence of the presence of single end-capped peo. *Macromolecules*, 36(4):1331–1340, January 2003.

[20] C. Chassenieux, T. Nicolai, and D. Durand. Association of hydrophobically end-capped poly(ethylene oxide). *Macromolecules*, 30(17):4952–4958, August 1997.

[21] W. D. Dozier, J. S. Huang, and L. J. Fetters. Colloidal nature of star polymer dilute and semidilute solutions. *Macromolecules*, 24(10):2810–2814, 1991.

[22] M. Daoud and J. P. Cotton. Star shaped polymers - a model for the conformation and its concentration-dependence. *Journal de Physique (Paris)*, 43(3):531–538, 1982.

[23] C. Rufier, A. Collet, M. Viguier, J. Oberdisse, and S. Mora. Influence of surfactants on hydrophobically end-capped poly(ethylene oxide) self-assembled aggregates studied by sans. *Macromolecules*, 44(18):7451–7459, September 2011.

[24] A. N. Semenov, J. F. Joanny, and A. R. Khokhlov. Associating polymers - equilibrium and linear viscoelasticity. *Macromolecules*, 28(4):1066–1075, February 1995.

[25] D. J. Lundberg, J. E. Glass, and R. R. Eley. Viscoelastic behavior among heur thickeners. *Journal of Rheology*, 35(6):1255–1274, 1991.

[26] J. F. Berret, Y. Sereo, B. Winkelman, D. Calvet, A. Collet, and M. Viguier. Nonlinear rheology of telechelic polymer networks. *Journal of Rheology*, 45(2):477–492, March 2001.

[27] T. Annable, R. Buscall, R. Ettelaie, and D. Whittlestone. The rheology of solutions of associating polymers - comparison of experimental behavior with transient network theory. *Journal of Rheology*, 37(4):695–726, July 1993.

[28] Mitchell A Winnik and Ahmad Yekta. Associative polymers in aqueous solution. *Current Opinion in Colloid & Interface Science*, 2(4):424–436, August 1997.

[29] S. O. X. Ma and S. L. Cooper. Shear thickening in aqueous solutions of hydrocarbon end-capped poly(ethylene oxide). *Macromolecules*, 34(10):3294–3301, May 2001.

[30] Enrique JimÃ©nez Regalado, Joseph Selb, and FranÃ§oise Candau. Viscoelastic behavior of semidilute solutions of multisticker polymer chains. *Macromolecules*, 32(25):8580–8588, November 1999.

[31] Sandra L. Cram, Hugh R. Brown, Geoffrey M. Spinks, Dominique Hourdet, and Costantino Creton. Hydrophobically modified dimethylacrylamide synthesis and rheological behavior. *Macromolecules*, 38(7):2981–2989, March 2005.

[32] Michael Rubinstein and Alexander N. Semenov. Dynamics of entangled solutions of associating polymers. *Macromolecules*, 34(4):1058–1068, January 2001.

[33] F. Lo Verso, A. Z. Panagiotopoulos, and C. N. Likos. Phase behavior of low-functionality, telechelic star block copolymers. *Faraday Discussions*, 144:143–157, 2010.

[34] T. Annable, R. Buscall, R. Ettelaie, P. Shepherd, and D. Whittlestone. Influence of surfactants on the rheology of associating polymers in solution. *Langmuir*, 10(4):1060–1070, April 1994.

[35] K. W. Zhang, B. Xu, M. A. Winnik, and P. M. Macdonald. Surfactant interactions with heur associating polymers. *Journal of Physical Chemistry*, 100(23):9834–9841, June 1996.

[36] S. Pispas, D. Vlassopoulos, G. Fytas, B. Loppinet, and N. Hadjichristidis. Modifying the rheological behavior of associative triblock copolymers in aqueous media through surfactant additives. *Polymer*, 47(20):7302–7311, September 2006.

[37] E. Alami, M. Almgren, and W. Brown. Interaction of hydrophobically end-capped poly(ethylene oxide) with nonionic surfactants in aqueous solution. fluorescence and light scattering studies. *Macromolecules*, 29(14):5026–5035, July 1996.

[38] S. Dai, K. C. Tam, E. Wyn-Jones, and R. D. Jenkins. Isothermal titration calorimetric and electromotive force studies on binding interactions of hydrophobic ethoxylated urethane and sodium dodecyl sulfate of different molecular masses. *Journal of Physical Chemistry B*, 108(16):4979–4988, April 2004.

[39] J. Appell, G. Porte, and M. Rawiso. Interactions between nonionic surfactant micelles introduced by a telechelic polymer. a small angle neutron scattering study. *Langmuir*, 14(16):4409–4414, August 1998.

[40] M. Filali, R. Aznar, M. Svenson, G. Porte, and J. Appell. Swollen micelles plus hydrophobically modified hydrosoluble polymers in aqueous solutions: Decoration versus bridging. a small angle neutron scattering study. *Journal of Physical Chemistry B*, 103(34):7293–7301, August 1999.

[41] A. Zilman, J. Kieffer, F. Molino, G. Porte, and S. A. Safran. Entropic phase separation in polymer-microemulsion networks. *Physical Review Letters*, 91:015901, Jul 2003.

[42] E. Michel, G. Porte, L. Cipelletti, and J. Appell. Analysis by the two-fluids model of the dynamical behavior of a viscoelastic fluid probed by dynamic light scattering. *Langmuir*, 20(3):984–990, February 2004.

[43] M. Gradzielski, A. Rauscher, and H. Hoffmann. Hydrophobically cross-linked micellar solutions - microstructure and properties of the solutions. *Journal de Physique IV*, 3(C1):65–79, May 1993.

[44] M. Filali, M. J. Ouazzani, E. Michel, R. Aznar, G. Porte, and J. Appell. Robust phase behavior of model transient networks. *Journal of Physical Chemistry B*, 105(43):10528–10535, November 2001.

[45] S. Maccarrone, H. Frielinghaus, J. Allgaier, D. Richter, and P. Lindner. Sans study of polymer-linked droplets. *Langmuir*, 23(19):9559–9562, September 2007.

[46] W. Meier, A. Falk, M. Odenwald, and F. Stieber. Microemulsion elastomers. *Colloid and Polymer Science*, 274(3):218–226, March 1996.

[47] G. Fleischer, F. Stieber, U. Hofmeier, and H.-F. Eicke. On the dynamics of equilibrium networks: Poe-b-pi-b-poe copolymers in h2o/aot/isooctane water in oil microemulsions. *Langmuir*, 10(6):1780–1785, June 1994.

[48] U. Batra, W. B. Russel, M. Pitsikalis, S. Sioula, J. W. Mays, and J. S. Huang. Phase behavior and viscoelasticity of aot microemulsions containing triblock copolymers. *Macromolecules*, 30(20):6120–6126, October 1997.

[49] T. Blochowicz, C. Gogelein, T. Spehr, M. Muller, and B. Stuhn. Polymer-induced transient networks in water-in-oil microemulsions studied by small-angle x-ray and dynamic light scattering. *Physical Review E*, 76(4):041505, October 2007.

[50] V. Testard, J. Oberdisse, and C. Ligoure. Monte carlo simulations of colloidal pair potential induced by telechelic polymers: Statistics of loops and bridges. *Macromolecules*, 41(19):7219–7226, October 2008.

[51] J. M. G. Sarraguca, A. A. C. C. Pais, and P. Linse. Structure of microemulsion - aba triblock copolymer networks. *Langmuir*, 24(19):11153–11163, October 2008.

[52] J. M. G. Sarraguca, A. A. C. C. Pais, and P. Linse. Influence of droplet properties on the formation of microemulsion-aba-triblock copolymer networks. *Soft Matter*, 5(1):140–147, 2009.

[53] Surita R. Bhatia and William B. Russel. End-capped associative polymer chains between nanospheres:attractions in ideal solutions. *Macromolecules*, 33(15):5713–5720, July 2000.

[54] M. E. Helgeson and N. J. Wagner. Colloidal interactions mediated by end-adsorbing polymer-like micelles. *Journal of Chemical Physics*, 135(8):084901, August 2011.

[55] H. Tabuteau, S. Mora, G. Porte, M. Abkarian, and C. Ligoure. Microscopic mechanisms of the brittleness of viscoelastic fluids. *Physical Review Letters*, 102(15):155501, April 2009.

[56] S. Mora. The kinetic approach to fracture in transient networks. *Soft Matter*, 7(10):4908–4917, 2011.

[57] M. Gradzielski, H. Hoffmann, and D. Langevin. Solubilization of decane into the ternary-system tdmao/1-hexanol/water. *Journal of Physical Chemistry*, 99(33):12612–12623, August 1995.

[58] J. Penfold, N. Wagner, and P. Schurtenberger. Scattering techniques, 2012. *Current Opinion In Colloid & Interface Science*, 17(1):1–2, February 2012.

[59] A. Radulescu and A. Loffe. Neutron guide system for small-angle neutron scattering instruments of the julich centre for neutron science at the frm-ii. *Nuclear Instruments*

& Methods In Physics Research Section A-accelerators Spectrometers Detectors and Associated Equipment, 586(1):55–58, February 2008.

[60] U. Keiderling. The new 'bersans-pc' software for reduction and treatment of small angle neutron scattering data. *Applied Physics A-materials Science & Processing*, 74:S1455–S1457, December 2002.

[61] J. Kohlbrecher and I. Bressler. Sasfit version 0.93.3 free avalable in the web (http://kur.web.psi.ch/sans1/sanssoft/sasfit.html).

[62] André Guinier. La diffraction des rayons x aux très faibles angles: Applications à l'etude des phénomènes ultra-microscopiques. *Annales de Physique (Paris)*, 12:161–236, 1939.

[63] O. Glatter and O. Kratky. *Small Angle X-ray Scattering*. Academic Press, London, 1982.

[64] G. Porod. Die röntgenkleinwinkelstreuung von dichtgepackten kolloiden systemen. *Colloid and Polymer Science*, 124(2):83–114, November 1951.

[65] Paul J. Flory. *Statistical Mechanics of Chain Molecules*. Interscience Publishers, 1969.

[66] LS Ornstein and F. Zernike. *Physik. Z.*, 19:134, 1918.

[67] J.P. Cotton. *Neutron, X-ray and Light Scattering*. Elsevier, New York, 1991.

[68] J. K. Percus and G. J. Yevick. Analysis of classical statistical mechanics by means of collective coordinates. *Physical Review*, 110(1):1–13, 1958.

[69] M. S. Wertheim. Exact solution of the percus-yevick integral equation for hard spheres. *Physical Review Letters*, 10(8):321–323, April 1963.

[70] Everett Thiele. Equation of state for hard spheres. *The Journal of Chemical Physics*, 39(2):474–479, 1963.

[71] R.J. Baxter. Percus-yevick equation for hard spheres with surface adhesion. *Journal of Chemical Physics*, 49(6):2770–2774, 1968.

[72] C. N. Likos, H. Lowen, M. Watzlawek, B. Abbas, O. Jucknischke, J. Allgaier, and D. Richter. Star polymers viewed as ultrasoft colloidal particles. *Physical Review Letters*, 80(20):4450–4453, May 1998.

[73] D. Qiu, T. Cosgrove, and A. M. Howe. Steric interactions between physically adsorbed polymer-coated colloidal particles: Soft or hard? *Langmuir*, 23(2):475–481, January 2007.

[74] J.P. Hansen and J.B. Hayter. A rescaled msa structure factor for dilute charged colloidal dispersions. *Molecular Physics*, 46:651–656, 1982.

[75] R. J. Glauber. Coherent and incoherent states of radiation field. *Physical Review*, 131(6):2766–&, 1963.

[76] P. G. de Gennes. Relaxation anomalies in linear polymer melts. *Macromolecules*, 35(9):3785–3786, April 2002.

[77] S. W. Provencher. A constrained regularization method for inverting data represented by linear algebraic or integral-equations. *Computer Physics Communications*, 27(3):213–227, 1982.

[78] J. T. Bendler and M. F. Shlesinger. Derivation of the kohlrausch-williams watts decay law from activation-energy dispersion. *Macromolecules*, 18(3):591–592, 1985.

[79] B. Nystrom, H. Walderhaug, and F. K. Hansen. Dynamic crossover effects observed in solutions of a hydrophobically associating water-soluble polymer. *Journal of Physical Chemistry*, 97(29):7743–7752, July 1993.

[80] C. Esquenet, P. Terech, F. Boue, and E. Buhler. Structural and rheological properties of hydrophobically modified polysaccharide associative networks rid c-6062-2008. *Langmuir*, 20(9):3583–3592, April 2004.

[81] M. Adam and M. Delsanti. Dynamical behavior of semidilute polymer-solutions in a theta-solvent - quasi-elastic light-scattering experiments. *Macromolecules*, 18(9):1760–1770, 1985.

[82] B. Ewen, D. Richter, B. Farago, and B. Stühn. Neutron spin-echo investigations on the segmental dynamics in semidilute polymer-solutions under theta-solvent and

good solvent conditions. *Journal of Non-Crystalline Solids*, 172:1023–1027, September 1994.

[83] D. S. Banks and C. Fradin. Anomalous diffusion of proteins due to molecular crowding rid d-9302-2011. *Biophysical Journal*, 89(5):2960–2971, November 2005.

[84] Jerker Widengren, Uelo Mets, and Rudolf Rigler. Fluorescence correlation spectroscopy of triplet states in solution: a theoretical and experimental study. *Journal of Physical Chemistry*, 99(36):13368–13379, September 1995.

[85] M. Weiss, H. Hashimoto, and T. Nilsson. Anomalous protein diffusion in living cells as seen by fluorescence correlation spectroscopy. *Biophysical Journal*, 84(6):4043–4052, June 2003.

[86] P. O. Gendron, F. Avaltroni, and K. J. Wilkinson. Diffusion coefficients of several rhodamine derivatives as determined by pulsed field gradient-nuclear magnetic resonance and fluorescence correlation spectroscopy. *Journal of Fluorescence*, 18(6):1093–1101, November 2008.

[87] A. Aggeli, M. Bell, N. Boden, J. N. Keen, P. F. Knowles, T. C. B. McLeish, M. Pitkeathly, and S. E. Radford. Responsive gels formed by the spontaneous self-assembly of peptides into polymeric beta-sheet tapes. *Nature*, 386(6622):259–262, March 1997.

[88] R. G. Larson. Going with the flow. *Science*, 318(5847):57–58, October 2007.

[89] S. Panmai, R. K. Prud'homme, and D. G. Peiffer. Rheology of hydrophobically modified polymers with spherical and rod-like surfactant micelles. *Colloids and Surfaces A-physicochemical and Engineering Aspects*, 147(1-2):3–15, January 1999.

[90] L. Kirschenmann and W. Pechhold. Piezoelectric rotary vibrator (prv) - a new oscillating rheometer for linear viscoelasticity. *Rheologica Acta*, 41(4):362–368, June 2002.

[91] Christoph Herfurth, Paula Malo de Molina, Christoph Wieland, Sarah Rogers, Michael Gradzielski, and Andre Laschewsky. One-step raft synthesis of well-defined amphiphilic star polymers and their self-assembly in aqueous solution. *Polymer Chemistry*, 3(6):1606–1617, 2012.

[92] Immergut E. H. Grulke E.A. Abe A. Brandrup, J. and D.R. Bloch. *Polymer Handbook*. John Wiley & Sons, Hoboken, New Jersey, 1999.

[93] Bruno H. Zimm. The scattering of light and the radial distribution function of high polymer solutions. *The Journal of Chemical Physics*, 16(12):1093–1099, 1948.

[94] H. Benoit and M. Benmouna. Scattering from a polymer solution at an arbitrary concentration. *Polymer*, 25(8):1059–1067, August 1984.

[95] Walther Burchard. Structure formation by polysaccharides in concentrated solution. *Biomacromolecules*, 2(2):342–353, April 2001.

[96] P.-G. De Gennes. *Scaling Concepts in Polymer Physics*. Cornell University Press: Ithaca, NY, 1979.

[97] J. des Cloizeaux. The lagrangian theory of polymer solutions at intermediate concentrations. *Journal de Physique (Paris)*, 36(4):281–291, 1975.

[98] D. J. Lundberg, R. G. Brown, J. E. Glass, and R. R. Eley. Synthesis, characterization, and solution rheology of model hydrophobically-modified, water-soluble ethoxylated urethanes. *Langmuir*, 10(9):3027–3034, September 1994.

[99] Q. T. Pham, W. B. Russel, J. C. Thibeault, and W. Lau. Micellar solutions of associative triblock copolymers:the relationship between structure and rheology. *Macromolecules*, 32(15):5139–5146, June 1999.

[100] E. Beaudoin, O. Borisov, A. Lapp, L. Billon, R. C. Hiorns, and J. Francois. Neutron scattering of hydrophobically modified poly(ethylene oxide) in aqueous solutions. *Macromolecules*, 35(19):7436–7447, September 2002.

[101] T. M. Birshtein and E. B. Zhulina. Scaling theory of supermolecular structures in block copolymer solvent systems .1. model of micellar structures. *Polymer*, 30(1):170–177, January 1989.

[102] P. Malo de Molina, C. Herfurth, A. Laschewsky, and M. Gradzielski. Multi-bridging polymers. synthesis and behaviour in aqueous solution. *Prog. Colloid Polym. Sci.*, 138:67–72, 2011.

[103] M. Schwab and B. Stuhn. Relaxation phenomena and development of structure in a physically crosslinked nonionic microemulsion studied by photon correlation spectroscopy and small angle x-ray scattering. *Journal of Chemical Physics*, 112(14):6461–6471, April 2000.

[104] E. Michel, L. Cipelletti, E. d'Humieres, Y. Gambin, W. Urbach, G. Porte, and J. Appell. Self-diffusion and collective diffusion in a model viscoelastic system. *Physical Review E*, 66(3):031402, September 2002.

[105] Michael Gradzielski and Heinz Hoffmann. Influence of charges on structure and dynamics of an o/w microemulsion. effect of admixing ionic surfactants. *Journal of Physical Chemistry*, 98(10):2613–2623, March 1994.

[106] I. Hoffmann, P. Heunemann, S. Prevost, R. Schweins, N. J. Wagner, and M. Gradzielski. Self-aggregation of mixtures of oppositely charged polyelectrolytes and surfactants studied by rheology, dynamic light scattering and small-angle neutron scattering. *Langmuir*, 27(8):4386–4396, April 2011.

[107] M. S. Green and A. V. Tobolsky. A new approach to the theory of relaxing polymeric media. *The Journal of Chemical Physics*, 14(2):80–92, 1946.

[108] E. Michel, M. Filali, R. Aznar, G. Porte, and J. Appell. Percolation in a model transient network: Rheology and dynamic light scattering. *Langmuir*, 16(23):8702–8711, August 2000.

[109] K. Thuresson, F. E. Antunes, M. G. Miguel, and B. Lindman. The association between a non-ionic microemulsion and hydrophobically modified peg. a rheological investigation. *Trends In Colloid And Interface Science XVI*, 123:40–43, 2004.

[110] H. Bagger-Jörgensen, L. Coppola, K. Thuresson, U. Olsson, and K. Mortensen. Phase behavior, microstructure, and dynamics in a nonionic microemulsion on addition of hydrophobically end-capped poly(ethylene oxide). *Langmuir*, 13(16):4204–4218, August 1997.

[111] S. H. Chen. Small-angle neutron-scattering studies of the structure and interaction in micellar and microemulsion systems. *Annual Review of Physical Chemistry*, 37:351–399, 1986.

[112] S. H. Chen, J. Rouch, F. Sciortino, and P. Tartaglia. Static and dynamic properties of water-in-oil microemulsions near the critical and percolation points rid b-4768-2012 rid f-2194-2011. *Journal of Physics-condensed Matter*, 6(50):10855–10883, December 1994.

[113] J. Appell, C. Ligoure, and G. Porte. Bending elasticity of a curved amphiphilic film decorated with anchored copolymers: a small angle neutron scattering study. *Journal of Statistical Mechanics-Theory and Experiment*, page P08002, August 2004.

[114] Massimo G. Noro and Daan Frenkel. Extended corresponding-states behavior for particles with variable range attractions. *The Journal of Chemical Physics*, 113(8):2941–2944, 2000.

[115] Eric Michel, Jacqueline Appell, Francois Molino, Jean Kieffer, and Gregoire Porte. Unstable flow and nonmonotonic flow curves of transient networks. *Journal of Rheology*, 45(6):1465–1477, November 2001.

[116] A. Stauffer, D.and Coniglio and M. Adam. Gelation and critical phenomena. *Advances in Polymer Science*, 44:103–158, 1982.

[117] M. Fuchs and K. S. Schweizer. Structure of colloid-polymer suspensions. *Journal of Physics-condensed Matter*, 14(12):R239–R269, April 2002.

[118] Eduardo Waisman. The radial distribution function for a fluid of hard spheres at high densities. *Molecular Physics*, 25(1):45–48, January 1973.

[119] Bo Svensson and Bo Jönsson. On the mean spherical approximation (msa) for colloidal systems. *Mol. Phys.*, 50(3):489–495, October 1983.

[120] Eric W. Kaler, Karl E. Bennett, H. Ted Davis, and L. E. Scriven. Toward understanding microemulsion microstructure: A small-angle x-ray scattering study. *Journal of Chemical Physics*, 79(11):5673–5684, December 1983.

[121] U. Olsson and P. Schurtenberger. Structure, interactions, and diffusion in a ternary nonionic microemulsion near emulsification failure. *Langmuir*, 9(12):3389–3394, December 1993.

[122] J. Brunner-Popela, R. Mittelbach, R. Strey, K.-V. Schubert, E. W. Kaler, and O. Glatter. Small-angle scattering of interacting particles. iii. d[sub 2]o-c[sub 12]e[sub 5] mixtures and microemulsions with n-octane. *Journal of Chemical Physics*, 110(21):10623–10632, June 1999.

[123] N. Puech, S. Mora, V. Testard, G. Porte, C. Ligoure, I. Grillo, T. Phou, and J. Oberdisse. Structure and rheological properties of model microemulsion networks filled with nanoparticles. *European Physical Journal E*, 26(1-2):13–24, May 2008.

[124] D. B. Siano and J. Bock. A polymer-microemulsion interaction - the coacervation model. *Journal of Colloid and Interface Science*, 90(2):359–372, 1982.

[125] M. Gradzielski and H. Hoffmann. Structural investigations of charged o/w microemulsion droplets. *Advances in Colloid and Interface Science*, 42:149–173, October 1992.

[126] S. W. Provencher. Contin - a general-purpose constrained regularization program for inverting noisy linear algebraic and integral-equations. *Computer Physics Communications*, 27(3):229–242, 1982.

[127] G. Hed and S. A. Safran. The immunity of polymer-microemulsion networks. *European Physical Journal E*, 19(1):69–76, January 2006.

[128] D. E. Koppel. Analysis of macromolecular polydispersity in intensity correlation spectroscopy - method of cumulants. *Journal of Chemical Physics*, 57(11):4814–&, 1972.

[129] Barbara J. Frisken. Revisiting the method of cumulants for the analysis of dynamic light-scattering data. *Applied Optics*, 40(24):4087–4091, August 2001.

[130] B. J. Berne and R. Pecora. *Dynamic Light Scattering: With Applications to Chemistry, Biology and Physics*. John Wiley, 1976.

[131] G. K. Batchelor. Brownian diffusion of particles with hydrodynamic interaction. *Journal of Fluid Mechanics*, 74(01):1–29, 1976.

[132] R. V. Sharma and K. C. Sharma. The structure factor and the transport properties of dense fluids having molecules with square well potential, a possible generalization. *Physica A: Statistical and Theoretical Physics*, 89(1):213 – 218, 1977.